The Dynamics of Strings, Monopoles, and Texture
in Nematic Liquid Crystals

by

Isaac L. Chuang

S.B. (Physics, MIT '90)

Submitted to the Department of Electrical Engineering and Computer Science
in partial fulfillment of the requirements for the degrees of

Bachelor of Science

and

Master of Science

at the

MASSACHUSETTS INSTITUTE OF TECHNOLOGY

June 1991

© Isaac L. Chuang 1991

The author hereby grants to MIT permission to reproduce and
to distribute copies of this thesis document in whole or in part.

Signature of Author _____
Department of Electrical Engineering and Computer Science
Feburary 1, 1991

Certified by ___
Bernard Yurke
Member of Technical Staff, AT&T Bell Laboratories
Company Supervisor (Cooperating company)

Certified by _____
Peter Hagelstein
Professor of Electrical Engineering, Department of Electrical Engineering and Computer Science
Thesis Supervisor (Academic)

Accepted by _____
Arthur C. Smith
Chairman, Department Committee on Graduate Students

Acknowledgements

The Dynamics of Strings, Monopoles, and Texture in Nematic Liquid Crystals

by

Isaac L. Chuang

Abstract

The dynamical behavior of topological defects created in symmetry breaking phase transitions is a universal phenomenon which is important in describing properties of systems in cosmology and in particle physics. However, to date, most of the research in this area has been theoretical in nature. This thesis represents an effort to pioneer the *experimental* investigation of defect dynamics, through a study of behavior associated with the broken symmetry phase of a simple condensed matter system – the liquid crystal.

The bulk of my thesis deals with experimental observations of strings and monopoles in a volume of nematic liquid crystal (NLC). These defects are created in a rapid, pressure–jump induced isotropic to nematic phase transition, and observed with a high speed video camera. I have also observed the decay of texture through a dynamical instability mechanism in a thin film preparation. My most important experimental results are (1) an experimental confirmation of the "one-scale" model originally developed for describing cosmic string evolution; (2) the categorization of defect interactions into sixteen distinct events identified by five "quantum numbers;" and (3) the accumulation of statistics describing the time evolutionary behavior of monopole, loop, and vertex densities, and various event branching ratios. I also document observations of string intercommutation and loop collapse.

The remainder of my results follow from my numerical investigations of defect dynamics in the 2D smectic, 2D nematic, and 3D nematic liquid crystals. I present a new formulation of the equations of motion for the NLC which utilize a SO(3) tensor field to reflect the underlying symmetries of the physical system. I also discuss data showing the scaling behavior of the structure function and monopole density in the 2D smectic simulation.

For the benefit of the reader, I review (1) the fundamental theories describing the behavior of the liquid crystal, (2) the underlying concepts of homotopy classification of topological defects, and (3) the mathematical description of defect structures. I also include numerous drawings and pictures showing the various defects and how they interact. My conclusion from this study is that certain theories can indeed be tested successfully through laboratory observations of the dynamics of symmetry breaking phase transitions in liquid crystals. I believe that liquid crystal research, in the context of cosmology and particle physics theories, promises to provide experimental insights which have never been within reach before.

Company Supervisor (Cooperating company): Bernard Yurke
Title: Member of Technical Staff, AT&T Bell Laboratories

Thesis Supervisor (Academic): Peter Hagelstein
Title: Professor of Electrical Engineering, Department of Electrical Engineering and Computer Science

Contents

List of Figures

x

List of Tables

Chapter 1

Introduction

This thesis presents the results of a study of the dynamics of topological defects created in a symmetry breaking phase transition of a liquid crystal. Through numerical simulations and direct experimental observations, I have systematically attempted to quantify the evolutionary behavior of strings, monopoles, and texture defects as they interact following their creation in a rapid isotropic to nematic phase transition.

In the introduction, I discuss the motivation for this work, provide some background on liquid crystals, describe the research goals, and cite some pertinent literature. I conclude by summarizing the organization of the remainder of the thesis.

1.1 Motivation

This study of defect dynamics is motivated by a perception of the growing importance of the role played by defects produced in symmetry breaking phase transitions in explaining the fundamental properties of physical systems, from particle and condensed matter physics to cosmology. For example, the standard model of particle physics is built on the notion of spontaneously broken internal symmetries. Recent work indicates that processes involving gauged texture defects in the dynamics of the electroweak phase transition play a major role in determining the final matter-antimatter asymmetry in the universe[KRS85, Sha37, Sha88, TZ90]. In hot big bang cosmology, defects are produced as the universe cools through symmetry breaking phase transitions[Kib76]; many cosmologists are attracted by the idea that such defects later seeded the large scale structure observed in the

1

universe today. Finally, in condensed matter physics, we are now beginning to develop an understanding of non-equilibrium scaling behavior, particularly near phase transitions, through study of defect dynamics[GMS83, Fur85, Kaw85, TH87, Bra89].

The universality of symmetry breaking phenomena suggests that theories dealing with time and space scales beyond the grasp of human manipulation may nevertheless be explored by observing similar systems in which all the relevant lengths have been uniformly scaled down to within reach of the experimentalist, while preserving the essential physics. In this spirit, Zurek proposed[Zur85] in 1985 a test of one of the key elements of the cosmological scenario, the Kibble mechanism, through observations of a quench-induced phase transition from normal ^{4}He to the superfluid. His idea was that in a rapid quench, topological string defects (vortex lines) would be created in the same way that some cosmological theories predict. Studying the resulting distribution of strings in the broken symmetry phase might thus give valuable clues about how analogous one-dimensional defects in cosmology, cosmic strings, should behave. Unfortunately, the experiment was never successfully performed, in part due to the difficulties of working with liquid helium.

The superfluid transition in liquid helium is described in terms of the transition from a paraboloid to a "mexican hat" free energy density. The analogy between this and similar "Higgs potentials" in particle physics theories motivated Zurek's proposal. Such potentials are ubiquitous in particle physics theories, providing the mechanism through which elementary particles get their masses. They are also ubiquitous in the description of phase transitions in condensed matter, so that it might well be hoped that a more experimentally tractable physical system could be found, in which Zurek's proposal would be realised. Liquid crystals provide such a system.

1.2 Background

Liquid crystals[KL88, VdJ88, dG74, DR78] are organic compounds which have phases intermediate to the liquid and solid phases. These mesophases, of which more than eight distinct types have been identified so far, are characterized by certain symmetries in the orientations of the rod-like molecules of the liquid crystalline substances. Typically, phase transitions occur between 10 and 200°C, and result in structures with length scales on the order of tens of microns to centimeters which may coarsen with a time scale on the order of seconds. Their preparation has been extensively studied[dG74, DR78], and in contrast to superfluid ^{4}He, they are relatively easy to work with in the laboratory, and require

Substance	Ordering Properties
Liquids	Isotropic – (high temp. phase) molecules randomly oriented, randomly located
Nematics	Aligned molecules – preferred orientation, random position
Smectics	Stacked planes – positional order in one dimension, random orientation
Crystals	Lattice – (low temp. phase) Positional and orientational regularity

Table 1.1: Liquid crystals in perspective.

only an optical microscope for observation. However, the main focus of the majority of work with liquid crystals has been on the *static* properties of defects – I shall be more interested in their *dynamics*, on which there has apparently been little work.

Table 1.1 provides some framework in which to judge the role of liquid crystals. The smectic liquid crystal (SLC) and nematic liquid crystal (NLC) are two mesophasic systems. The molecules in a SLC and NLC, in the broken symmetry phase, have more orientational and positional order than in a liquid, but less than in a crystal. Temperature changes are the primary mechanism for causing a system to move from one phase to another, but pressure jumps also work. The intermediate states of NLC or SLC systems, as they undergo a phase transition from a high-temperature isotropic phase to the cooler nematic or smectic phase, are characterized by the presence of topological defects. These defects interact with the viscous medium, dissipating energy; in an infinite system, the density of defects drops according to some power law, eventually reaching zero. This behavior is the subject of my study.

Why do topological defects form? Defects are unavoidably created in symmetry breaking phase transitions because of the finite speed of communication between different parts of a system. Imagine that there is a characteristic velocity v_{info} at which information propagates between molecules, and consider the process of suddenly cooling a volume of NLC which was previously equilibrated in its high-temperature, isotropic phase. Suppose that the isotropic→nematic phase transition takes place in some small time t_{quench}. Upon undergoing the phase transition, all $\xi^3 = (v_{info} t_{quench})^3$ sub-volumes of the NLC will select a random, preferred orientation. However, because v_{info} is typically much slower than the scale of the system divided by t_{quench}, there are a huge number of these sub-volumes which have independently oriented themselves. Furthermore, because the tendency in the nematic phase of all molecules to align in one direction as uniformly as possible, the individual ξ^3 volumes will subsequently communicate and attempt to come to a consensus. In this process, the characteristic

3

length scale ξ for which molecule orientations are correlated will grow larger. Soon, patches of one orientation bump into patches of another orientation, resulting in conflicts which can only be resolved by the destruction of one of the contenders. Such conflicts are topological defects. I will discuss their formation and behavior in greater detail in Chapter 2.

Finally, I note a few points about the nomenclature used in this thesis. I have chosen to call one-dimensional defects "strings", in keeping with the convention used in high-energy physics and cosmology. In condensed matter physics, especially in the study of liquid crystals, strings are often referred to as "disclination lines." The two topological charges of monopoles and strings, ± 1 and $\pm\frac{1}{2}$, are usually delineated as being "type-1" and "type-$\frac{1}{2}$;" however, I will simply describe them by their charges. Also, I denote the $\pi_3(\mathcal{M}_0)$ defect in the NLC as "texture," following the convention of Turok et. al.[Tur89]; texture defects are sometimes referred to as topological solitons. The term "texture" is also sometimes used in the literature to refer to the pattern of the director field in liquid crystals; this can be confusing, and I do not use that convention here.

1.3 The Research Goals

The goals of this research were to study the dynamics of topological defects in a nematic liquid crystal, and to try to understand observations in the context of various models drawn from theories of ordering dynamics in condensed matter physics and cosmology. I approached these goals with two tools: numerical simulations and experimental observations. In my experiments, I studied string intercommutation and loop-collapse, and I searched for texture defects. I also quantified monopole creation and annihilation mechanisms, and sought to characterize defect interactions through the formulation of a systematic categorization strategy. In my numerical work, my goal was to implement a full simulation of the 3D NLC.

Several models have been important in this study. In particular, one of my goals was to experimentally investigate the workings of the "Kibble mechanism" of defect production[Kib80] (the scenario described in the previous section), and test the "one-scale"[AT89] model for string network evolution. I also studied the behavior of the structure function, or two-point correlation function, in a simulation of a two dimensional SLC system.

Finally, because of the pioneering nature of this work, I also saw an opportunity to develop novel numerical and experimental techniques for studying defect dynamics in liquid crystals. Numerical

simulation of NLC systems is complicated by the need to preserve the underlying physical symmetries. Together with B. Yurke, I attempted, and succeeded, in devising and applying a new formulation of the NLC equations of motion. We also sought to develop new experimental techniques for observing defect dynamics in vivo, by designing and constructing a pressure cell to allow study of rapid, pressure jump induced isotropic→nematic phase transitions, and a thin film apparatus to allow mechanical manipulation of line defects in thin films of material.

1.4 A Brief Review of the Literature

Literature pertinent to the research described in this thesis can be divided into three general categories, including those describing (1) liquid crystal chemistry and properties, (2) dynamics of topological defects, and (3) numerical simulations of broken symmetry systems.

1.4.1 Liquid Crystal Properties

Liquid crystal research has mostly been driven by its commercial use in display technology. The majority of the fundamental experimental work was published in the early 1970's, by French researchers. Several beautiful review articles, [Bou81, Bou74, Bou73, KL88], present an overview of static properties and structures of defects observed in various liquid crystals. The fundamental text in this area is by de Gennes[dG74]. I have also found [VdJ88] and [DR78] useful references.

Certain works I have referred to are of particular note. A derivation of the Frank free energy, including the saddle-splay curvature term is presented in [NS71]. Previous high pressure studies of liquid crystal properties are reviewed in [CS79].

1.4.2 Topological Defects

My discussion of topological defects and homotopy theory, using simple physical arguments, is most approachable from the presentations by Mermin[Mer79] and Michel[Mic80]. The specific application of homotopy theory to a discussion of defects in liquid crystals is discussed by Kurik and Lavrentovich[KL88]. Texture, and its role in seeding large-scale structure in the universe is described in [GST90, CPT90] and [TS90, Tur89], and cosmic string seeded galaxies are discussed in [Vil81]. The properties of cosmic strings are reviewed in [Vil85], and string scaling, intercommutation, and kinks are discussed by [AC90].

5

The static structure of defects in liquid crystals has been widely studied. A good overview is provided by Kléman[Kle83]. Notable work in this area includes a discussion of monopole structure[Ost81] and an experimental study of ±1 string structure[WPC72a].

Literature on the the dynamics of defects in liquid crystals is sparse. The dynamics of string defects are discussed by [CvSFK87, Rey90, GSG75, GGS73, MYT+77]. Lavrentovich and Rozhkov have also considered ±1 strings terminated by boojums[LR88]. Finally, a Japanese research group has reported an interesting study of the coarsening dynamics and scaling properties of defects in twisted nematics[NOI87, OI86].

1.4.3 Numerical Simulations

The ordering dynamics of a physical system that has undergone a deep quench from a phase of higher symmetry to a phase of lower symmetry is a topic of considerable interest[Fur85, HH77, Voo85, GMS83]. The behavior of such systems is expected to depend on the dimensionality and internal symmetry of the system, and the presence of conservation laws. The bulk of the experimental[CW90, GSM87] and theoretical[RED88, Bra89, Kaw85, Kle90, TCG88, Hus86, ASM88, MV87] work that has been reported is on the phase separation dynamics (spinodal decomposition) of binary mixtures.

More recently, attention has also focused on systems whose Hamiltonian has a continuous rather than discrete symmetry[MG90, TH87, Toy90, NN89, dPT86, MZ85]. Generally, theoretical work has concentrated on models characterized by the time-dependent Landau-Ginzburg equation[NN89]. For such models, with nonconserved order parameter, it is generally predicted[TH87, MZ85] that the defect line density should scale as t^{-1}. However, a scaling behavior of $t^{-0.75 \pm 0.05}$ from numerical simulations has been reported in three dimensions[NN89], and $t^{-1.00 \pm 0.04}$ in two dimensions[MG90].

The specific simulation of nematic liquids has been investigated in [CF90], and the simulation of string networks is discussed in [BB90], [AT85], [MMR90], and other works.

1.5 Organization of the Manuscript

The outline of this thesis is as follows: in Chapter 2, I introduce a mathematical discussion of topological defects, through a brief introduction to homotopy theory. I also introduce the field equations specific to the nematic and smectic liquid crystal simulations which will be discussed later. Chapter 3 summarizes my understanding of monopole, string, and texture defect structures, relying

primarily on developing visual representations of molecule arrangements and the homotopy theory of the previous chapter. A study of these defects through numerical simulation is the subject of Chapter 4. I performed three simulations, and discuss them in order of complexity: the 2D-SLC, the 2D-NLC, and the 3D-NLC. My results for the scaling of the structure function and monopole density measured for the 2D-SLC are inconclusive, and data generated by my 3D-NLC simulation show nothing unexpected. However, my work successfully implemented and tested a new method of using a SO(3) tensor field for simulating the NLC.

Next, I present my experimental results, in Chapter 5. I find that though the "one-scale" model for string network evolution properly characterizes our[1] results remarkably well, the monopole statistics we have gathered do not agree with our expectations. Other observations I record include a string intercommutation sequence, loop collapses, and monopole creation and annihilation events. These defect interactions can be understood in terms of a microscopic model characterized by a certain events which occur with some probability. Chapter 5 concludes with a discussion of an event categorization strategy which I and B. Yurke propose for describing defect dynamics in the NLC. Finally, in the conclusion, I briefly summarize my results and present ideas for future work.

---

[1]The research described in this thesis is principally the result of my own design, unless otherwise noted. However, all the experimental work was performed in close cooperation with B. Yurke. Thus, I will take liberty in using the first person plural.

Chapter 2

Theory

The existence of topological defects resulting from symmetry breaking phase transitions is most simply understood from a group theoretic standpoint. Their particular structure, however, is determined by the specific equations governing the system under study – for the liquid crystal, these are given by the Frank free energy[dG74]. I shall begin the discussion with a presentation of the equations of motion governing liquid crystal molecules, then conclude with an introduction to topological defects and homotopy theory.

2.1 Liquid Crystal Formalisms

The nematic liquid crystal can be viewed as a fluid of rod-like molecules. These rods can be approximated to have complete cylindrical and inversion symmetry. In the nematic phase, all the rods align in one preferred direction, known as the "nematic axis," while in the isotropic phase, the rods become completely orientationally disordered (Figure 2-1). The state of the system can be quantified by the "order parameter," which varies from some finite nonzero value in the nematic phase to 0 in the isotropic phase. A rod-molecule fluid can also be characterized microscopically, by the so-called "director field" $\vec{n}(\vec{r})$, a vector (or tensor) field which simply gives the orientations of all the molecules. The free energy density is determined by the relative local orientations of molecules; thus, it can be written as a function of $\vec{n}(\vec{r})$. In the following discussion, I will construct the order parameter for a rod-molecule fluid and discuss how the free energy comes about. I will conclude this section by deriving the equations of motion from the free energy functional.

9
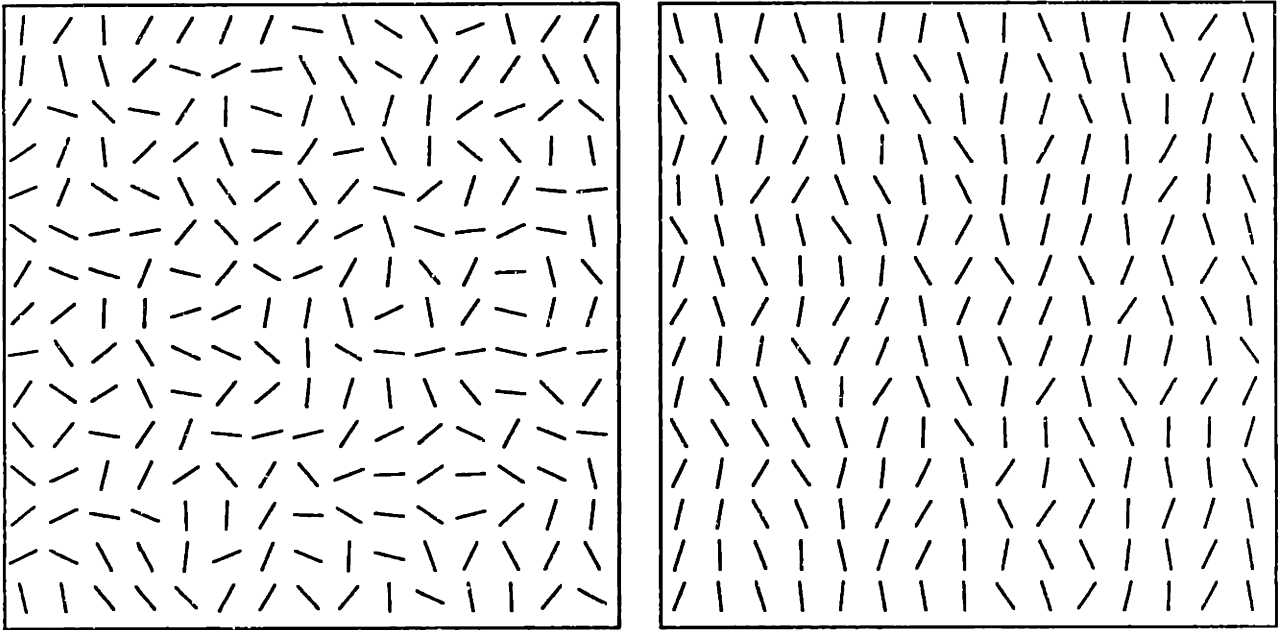
Figure 2-1: The nematic and isotropic phases of an assembly of rod-like molecules. The isotropic phase, shown on the left, is characterized by orientational disorder. In the nematic phase, on the right, the molecules align in one preferred direction, known as the "nematic axis." Note that the rods are shown on a lattice (with positional order) only for clarity; in the actual case, the rods would be randomly positioned.

2.1.1 The Order Parameter

The orientations of rod-molecules in a fluid can be described collectively by the probability $p(\theta, \phi)$ of finding a rod oriented in the θ, ϕ direction, where θ is the polar angle and ϕ is the azimuthal angle, as usual, and $\hat{z}$ is taken to be the nematic axis. In both the nematic and isotropic phases, $p(\theta, \phi)$ is independent of ϕ, and $p(\theta) = p(\theta + \pi)$. However, in the nematic phase, $p(\theta)$ is peaked around $\theta = 0$ and $\theta = \pi$, and minimal for $\theta = \pi/2$, following from our definition of the nematic axis. In the isotropic phase, $p(\theta)$ is a constant. Thus, the simplest single parameter which describes the phase of the fluid is

$$S = \frac{1}{2}(3\langle\cos^2\theta\rangle - 1), \tag{2.1}$$

where the brackets refer to averaging over the solid angle $d\Omega$, and θ are the orientations of the individual rods. In the nematic phase, $\cos^2\theta = 1$, so that $S = 1$, and in the isotropic phase, $\langle\cos^2\theta\rangle = \frac{1}{3}$, so that $S = 0$.

Generalization of Eq. (2.1) gives a tensor order parameter

$$Q_{ab} = S\left[n_a n_b - \frac{1}{3}\delta_{ab}\right], \tag{2.2}$$

with n_a a three-vector giving the x, y, and z components of the orientation of a rod molecule. S is a normalization factor. Here, and in the following discussion, I use implicit summation rules, where repeated Roman indices are to be summed over $\{x,y,z\}$, referred to as $\{1,2,3\}$. The free energy density F of a nematic fluid may be expanded in terms of powers of Q_{ab}. Following de Gennes[dG74]:

$$F = F_0 + \frac{1}{2}A(T)Q_{ab}Q_{ba} + \frac{1}{3}B(T)Q_{ab}Q_{bc}Q_{ca} + \mathcal{O}(Q^4), \tag{2.3}$$

where T is the temperature. The existence of a non-vanishing term of order Q^3 is important, and indicates that the isotropic→nematic phase transition is of first order, in agreement with experiment[VdJ88]. Inclusion of a Q^3 term is mandated because a state of Q_{ab} does not necessarily have the same free energy as one of $-Q_{ab}$; there is no symmetry relation. The behavior of the free energy as a function of the order parameter can thus be depicted as in Figure 2-2 near the isotropic→nematic phase transition.

The existence of a phase transition in the NLC can also be understood as occurring through competition between positional entropy, which favors the rods being randomly located, and orientational

11
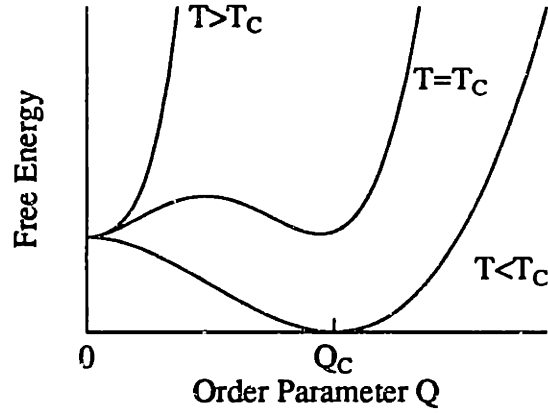
Figure 2-2: The behavior of the free energy density F near the isotropic→nematic phase transition, as a function of the order parameter Q, for various temperatures T. T_c is the critical temperature.

entropy, which favors them being randomly oriented.[1] At high pressure, or low temperatures, maximizing positional entropy is most important, and the favored phase is the "nematic" phase, where the rods are all nearly aligned along the nematic axis. Conversely, at low pressure, or high temperature, the "isotropic" phase is instead favored.

I shall not find the order parameter useful in the remainder of the discussion in this thesis, but its presentation here serves to connect the NLC system to others studied in statistical mechanics.

2.1.2 The Frank Free Energy

The molecules of the NLC obey symmetries invariant under rigid rotations (about the molecular axes) and inversions ($\vec{n} \rightarrow -\vec{n}$). These symmetries naturally lead to a free energy which, in the most general case, consists of four terms:

$$\mathcal{E}_{lc} = \frac{1}{2} \left[k_1 (\vec{\nabla} \cdot \vec{n})^2 + k_2 (\vec{n} \cdot \vec{\nabla} \times \vec{n})^2 \right. \tag{2.4}$$
$$\left. + k_3 \left| \vec{n} \times (\vec{\nabla} \times \vec{n}) \right|^2 + k_4 \vec{\nabla} \cdot \left((\vec{n} \cdot \vec{\nabla})\vec{n} - \vec{n}(\vec{\nabla} \cdot \vec{n}) \right) \right].$$

The four terms in Eq. (2.5) are known as the "splay," "twist," "bend," and "saddle–splay curvature" terms, respectively[Bou81]. Usually, the k_i are not equal; in the particular substance I have studied (see

---

[1]This argument was first given by Onsager (see [dG74]).

section 5.1), $k_1 \approx k_3 \approx 2k_2$. Nevertheless, a popular approximation is to take the k_i equal. In such a case, $\mathcal{E}_{lc}$ becomes related to the free energy for that of an analogous field theory with spontaneously broken global symmetry (where global SO(3) internal symmetry is spontaneously broken to O(2) by a traceless symmetric tensor[2]), as follows:

$$\mathcal{E}_{lc} = \mathcal{E}_{ft} + \frac{k - k_4}{2}\left[(\partial_a n_a)^2 - (\partial_b n_a)(\partial_a n_b)\right] . \tag{2.5}$$

Furthermore, the k_4 term is usually neglected, because it does not appear in the equations of motion, being a surface term. For $k = k_1 = k_2 = k_3$, and $k_4 - k = 0$, Eq. (2.5) becomes what is known as the "equal-constant" approximation:

$$\mathcal{E}_{\text{equal constant}} = \mathcal{E}_{ft} = \frac{k}{2}(\partial_a n_b)^2 , \tag{2.6}$$

where n_i are the cartesian components of the director field.

The Frank free energy is Eq. (2.5) without the k_4 surface term. This is written as follows:

$$\mathcal{E}_{\text{Frank}}[n_i, \partial_m n_i] = \frac{k_1}{2}(\partial_a n_a)^2 + \frac{k_2}{2}(n_c \epsilon_{abc}\partial_a n_b)^2 + \frac{k_3}{2}(\epsilon_{dce} n_d \epsilon_{abc}\partial_a n_b)^2 . \tag{2.7}$$

Note that $\mathcal{E}_{\text{Frank}}$ is positive definite. Generally, the Frank free energy is taken to be the most "correct" energy density to use in describing the properties of a liquid crystal (after all, it has the greatest number of degrees of freedom). However, a simpler expression, which results from setting the k_i equal in the Frank free energy, is much easier to work with. It differs from the equal constant expression only by a surface term, which is usually neglected. Because the fundamental physics I am interested in can be studied in the equal constant approximation, I will often use Eq. (2.6) in favor of Eq. (2.7).

2.1.3 The Equations of Motion

The equations governing the motion of the molecules in the nematic liquid crystal are most easily approached by considering first a two-dimensional system without an inversion symmetry. This is the smectic liquid crystal (SLC). After I discuss the 2D SLC, I will extend my calculations to the 2D and 3D NLC cases.

The SLC is described by a director field in which the the $\vec{n}(\vec{r})$ in each x-y plane $\mathcal{R}_i^2$ are tilted by

---
[2]for a further discussion of this point, see [CDTY90].

some constant angle θ_i with respect to the z-axis. The azimuthal angle $\phi(x, y)$ is left undetermined, and the θ_i is usually the same from plane to plane. Once again, note that the symmetry of the NLC is more complicated. Its director field has a local inversion symmetry, whereby the replacement $\vec{n}(\vec{r}) \rightarrow -\vec{n}(\vec{r})$ does not change any of the NLC's physical observables.

The dynamics of the director field in the NLC and the 2D SLC are governed by the Frank free energy functional. Normally, the magnitude of $\vec{n}(\vec{r})$ is constant and chosen to be unity, for both the SLC and the NLC. However, because the free energy diverges at a singularity (a terrible thing to have to cope with in numerical simulations), I add an additional term which cuts off infinite divergences by allowing the length of the $\vec{n}(\vec{r})$ to change in the locality of defects. Such a cutoff is introduced naturally by the finite size of the molecules in the actual physical system. Thus, the total energy functional I use in deriving the equations of motion is a sum of the field energy and a lambda potential energy term:

$$\mathcal{E}_{\text{lc}}\left[n_i, \partial_m n_i\right] = \frac{k_1}{2}(\partial_a n_a)^2 + \frac{k_2}{2}(n_c \epsilon_{abc} \partial_a n_b)^2 + \frac{k_3}{2}(\epsilon_{dce} n_d \epsilon_{abc} \partial_a n_b)^2 + \frac{\lambda}{4}(n_a n_a - 1)^2 . \quad (2.8)$$

The equations of motion for the 2D SLC can be derived directly from this energy functional by using the variational principle. Similar equations for the NLC are more complicated to derive, because this expression does not include the local inversion symmetry required by the nematic. To analyze the NLC therefore, I will first rewrite the free energy in tensor form, using SO(2) and SO(3) matrices[3] for the 2D and the 3D cases, respectively. As in the smectic, the equations of motion will then follow from variationally minimizing the energy.

2.1.4   2D SLC Equations of Motion

Because the SLC has a planar symmetry, it is appropriate to model only a single, 2D layer of SLC. Also, I choose to study only planar configurations of SLC because they can be related to experimental results from free standing thin films. In two dimensions, Eq. (2.8) reduces to:

$$\mathcal{E}_{\text{2D}} = \frac{k_1}{2}(\partial_a n_a)^2 + \frac{k_3}{2}(\epsilon_{ab} \partial_a n_b)^2 + \frac{\lambda}{4}(n_a n_a - 1)^2 , \quad (2.9)$$

where the indices vary over 1, 2, and $\epsilon_{11} = \epsilon_{22} = 0, \epsilon_{12} = 1$, and $\epsilon_{21} = -1$. The equations of motion

---

[3] SO(n) are the groups formed from the set of proper rotations in n-dimensional Euclidean space. They can be represented as symmetric $n \times n$ matrices.

follow from the Euler-Lagrange equation, modified appropriately to reflect the dissipative nature of this system:

$$\left[\partial_m \frac{\partial}{\partial(\partial_m n_k)} - \frac{\partial}{\partial n_k}\right] \mathcal{E}_{2D} = \gamma \partial_t n_k. \tag{2.10}$$

The equations of motion for the 2D SLC are thus:

$$\gamma \partial_t n_k = k_1 \partial_k \partial_a n_a + k_3 \epsilon_{ck} \epsilon_{ab} \partial_c \partial_a n_b - \lambda(n_a n_a - 1)n_k. \tag{2.11}$$

2.1.5   2D NLC Equations of Motion

The symmetry of the NLC under local inversion of the director field corresponds to a group symmetry of SO(2) and SO(3) matrices for a two or three dimensional system. The major problem with writing a SO(2) or SO(3) tensor formulation of Eq. (2.7), however, is that the energy must be positive definite, in order to allow variational minimization. One way to assure this is to construct equivalent tensor expressions for the terms in the parentheses in Eq. (2.7). This approach begins by writing down all possible low-order combinations of derivatives and tensors using $N_{ab} = n_a n_b$, and combining them creatively until the desired expressions are found. By construction, identities which can be exploited include:

$$N_{aa} = 1 \tag{2.12}$$

$$N_{ab} = N_{ba} \tag{2.13}$$

$$\partial_a N_{bb} = 0. \tag{2.14}$$

In two dimensions, these identities become

$$n_1 \partial_1 n_1 + n_2 \partial_1 n_2 = 0 \tag{2.15}$$

$$n_1 \partial_2 n_1 + n_2 \partial_2 n_2 = 0 \tag{2.16}$$

$$n_1^2 + n_2^2 = 1. \tag{2.17}$$

15

For the 2D, SO(2) tensor case, the following free energy expression is equivalent to the $\mathcal{E}_{2D}$ of Eq. (2.9):

$$\mathcal{E}_{2D-NLC} = \frac{k_1}{2}\left[\partial_a N_{ab} - N_{ca}\partial_a N_{cb}\right]\left[\partial_d N_{db} - N_{ed}\partial_d N_{eb}\right] \qquad (2.18)$$

$$+\frac{k_3}{2}\left[N_{de}\epsilon_{ab}\partial_a N_{bd}\right]\left[N_{he}\epsilon_{fg}\partial_g N_{gh}\right]$$

$$+\frac{\lambda_A}{2}[N_{aa} - 1]^2 + \frac{\lambda_B}{4}[N_{ab}N_{ab} - 1]^2 .$$

Again, a lambda potential term has been added to cutoff infinite divergences at the cores of singularities. Unlike for the vector free energy though, there are two terms. In the case where $\lambda_A \to \infty$ and $\lambda_B \to \infty$, the SO(2) tensor has a unique mapping to a $\mathcal{R}^2$ vector (except for the desired inversion degeneracy):

$$n_1 = \sqrt{N_{11}} = N_{12}/\sqrt{N_{22}} \qquad (2.19)$$

$$n_2 = \sqrt{N_{22}} = N_{12}/\sqrt{N_{11}} . \qquad (2.20)$$

When λ_A and λ_B are finite, as they are in my computer simulations, there is no unique mapping; however, significant deviation will only occur at the cores of singularities, where knowledge of the exact orientation of the director field is not crucial.

Finally, using the variational principle leads to the complete equations of motion for the 2D NLC, as given in Figure 2-3.

A simplified version of the free energy, given by setting $k = k_1 = k_3$, is considerably easier to deal with:

$$\mathcal{E}_{simp2D} = \frac{k}{4}(\partial_a N_{bc})(\partial_a N_{bc}) + \frac{\lambda_A}{2}[N_{aa} - 1]^2 + \frac{\lambda_B}{4}[N_{ab}N_{ab} - 1]^2 . \qquad (2.24)$$

The corresponding equations of motion are:

$$\gamma\partial_t N_{ik} = \frac{k}{2}\partial_a\partial_a N_{ik} - \lambda_A\delta_{ik}(N_{aa} - 1) - \lambda_B N_{ik}(N_{ab}N_{ab} - 1) . \qquad (2.25)$$

2.1.6 3D NLC Equations of Motion

The 3D NLC equations of motion are similar to those of the 2D NLC case. Instead of SO(2) tensors, SO(3) tensors form the underlying field. Also, the rank of the levi-civita tensors must be raised from

16

$$\frac{\partial \mathcal{E}_{\text{2D-NLC}}}{\partial N_{ik}} = \frac{k_1}{2}(N_{ca}\partial_a N_{cb} - \partial_a N_{ab})(\partial_k N_{ib} + \partial_i N_{kb}) \tag{2.21}$$

$$+\frac{k_3}{2}\epsilon_{ab}\epsilon_{fg}(\partial_a N_{bd})(N_{dk}\partial_f N_{gi} + N_{gi}\partial_f N_{gk})$$

$$+\lambda_A \delta_{ik}(N_{aa} - 1) + \lambda_B N_{ik}(N_{ab}N_{ab} - 1)$$

$$\partial_m \frac{\partial \mathcal{E}_{\text{2D-NLC}}}{\partial(\partial_m N_{ik})} = \frac{k_1}{2}[\delta_{mi}\delta_{kb} - N_{im}\delta_{kb} + \delta_{mk}\delta_{ib} - N_{km}\delta_{ib}] \tag{2.22}$$

$$\times [\partial_m \partial_a N_{ab} - N_{ca}\partial_m \partial_a N_{cb} - (\partial_m N_{ca})(\partial_a N_{cb})]$$

$$+\frac{k_1}{2}[\delta_{kb}\partial_m N_{im} + \delta_{ib}\partial_m N_{km}][\partial_a N_{ab} - N_{ca}\partial_a N_{cb}]$$

$$+\frac{k_3}{2}\epsilon_{ab}\epsilon_{mg}[\delta_{ig}\delta_{kn} + \delta_{ik}\delta_{kg}]$$

$$\times [N_{de}N_{ne}\partial_m \partial_a N_{bd} + N_{de}(\partial_m N_{ne})(\partial_a N_{bd})N_{ne}(\partial_m N_{de})(\partial_a N_{bd})]$$

$$\gamma \partial_t N_{ik} = \partial_m \frac{\partial \mathcal{E}_{\text{2D-NLC}}}{\partial(\partial_m N_{ik})} - \frac{\partial \mathcal{E}_{\text{2D-NLC}}}{\partial N_{ik}} \tag{2.23}$$

Figure 2-3: Equations of motion for the 2D NLC

two to three, and subsequently the k_3 term changes. Finally, a k_2 term must be included, and the λ_B term must be expanded (because there are more degrees of freedom in the 3×3 matrices which must be fixed). The free energy becomes:

$$
\begin{aligned}
\mathcal{E}_{\text{3D-NLC}} = \;& \frac{k_1}{2} \left[\partial_a N_{ab} - N_{ca} \partial_a N_{cb} \right] \left[\partial_d N_{db} - N_{ed} \partial_d N_{eb} \right] \\
&+ \frac{k_2}{2} \left[\epsilon_{abc} N_{ad} \partial_b N_{cd} \right]^2 \\
&+ \frac{k_3}{2} \left[N_{ab} \partial_b N_{ca} \right] \left[N_{de} \partial_e N_{cd} \right] \\
&+ \frac{\lambda_A}{2} \left[N_{aa} - 1 \right]^2 + \frac{\lambda_B}{4} \left[N_{ab} N_{cd} - N_{ac} N_{bd} \right] \left[N_{ab} N_{cd} - N_{ac} N_{bd} \right] .
\end{aligned}
\tag{2.26}
$$

The corresponding equations of motion are straightforward but lengthy to calculate; I leave them as an exercise for the reader.

Simplified equations of motion

The 3D NLC equivalent of Eq. (2.25) is given by using the free energy expression:

$$
\mathcal{E}_{\text{simp3D}} = \frac{k}{4} (\partial_a N_{bc})(\partial_a N_{bc}) + \frac{\lambda_A}{2} \left[N_{aa} - 1 \right]^2 + \frac{\lambda_B}{4} \left[N_{ab} N_{cd} - N_{ac} N_{bd} \right] \left[N_{ab} N_{cd} - N_{ac} N_{bd} \right] ,
\tag{2.27}
$$

where $k = k_1 = k_2 = k_3$. The corresponding equations of motion are:

$$
\gamma \partial_t N_{ik} = \frac{k}{2} \partial_a \partial_a N_{ik} - \lambda_A \delta_{ik} (N_{aa} - 1) \lambda_B \left[2 N_{ab}^2 N_{ik} - N_{ai} N_{bk} N_{ab} - N_{ak} N_{bi} N_{ab} \right] .
\tag{2.28}
$$

The equivalence of Eq. (2.27) to Eq. (2.6) is established by substituting $N_{ab} = n_a n_b$ into Eq. (2.27), and expanding (the λ terms can be disregarded):

$$
\begin{aligned}
\mathcal{E}_{\text{simp3D}} &= \frac{k}{4} (\partial_a N_{bc})(\partial_a N_{bc}) \tag{2.29} \\
&= \frac{k}{4} (\partial_a (n_b n_c)) (\partial_a (n_b n_c)) \\
&= \frac{k}{4} (n_c \partial_a n_b + n_b \partial_a n_c)(n_c \partial_a n_b + n_b \partial_a n_c) \\
&= \frac{k}{2} [(n_c \partial_a n_b)(n_c \partial_a n_b) + (n_c \partial_a n_b)(n_b \partial_a n_c)] \\
&= \frac{k}{2} (\partial_a n_b)^2
\end{aligned}
$$

18

$$= \mathcal{E}_{\text{equal constant}} \cdot$$

The identity $2n_b \partial_a n_b = \partial_a N_{bb} = 0$, derived from Eq. (2.14), is used in the fifth line. These steps are typical of the process used to progressively derive tensor expressions equivalent to the usual vector ones.

Mapping from SO(3) to $\vec{n}$

The mapping of a SO(3) matrix to a three-vector can be accomplished in three ways. The symmetric matrix N_{ik} is defined as

$$N_{ik} = \begin{bmatrix} n_x^2 & n_x n_y & n_x n_z \\ & n_y^2 & n_y n_z \\ & & n_z^2 \end{bmatrix} . \tag{2.30}$$

The λ_A and λ_B terms impose the following restrictions:

$$N_{11} + N_{22} + N_{33} = 1 \tag{2.31}$$

$$N_{12}^2 = N_{11} N_{22} \tag{2.32}$$

$$N_{13}^2 = N_{11} N_{33} \tag{2.33}$$

$$N_{12} N_{23} = N_{22} N_{13} \tag{2.34}$$

When $\lambda_A = \lambda_B \to \infty$, these restrictions are obeyed perfectly. However, for finite λ's, there will be some degeneracy between the possible mappings from N_{ik} to $\vec{n}$. I use the following criteria: the first of the diagonal elements N_{ii} (starting with $i = 1$) which is substantially greater than zero is chosen as a starting point, and $n_i = \sqrt{N_{ii}}$ is calculated. From the off diagonal elements N_{12}, N_{13}, and N_{23} are derived the two remaining components. I have found this method to work well enough to allow proper visualization of the field as it is evolved.

2.1.7 Summary

The results of this section are summarized in Table 2.1. I have devised a potential contribution modification to the free energy to allow cutoff of singularities, and derived equations of motion for the two-dimensional smectic, nematic, and three-dimensional nematic systems. The NLC equations

19

System	Eq. Motion	Free Energy
2D smectic	Eq. (2.11)	$\mathcal{E}_{2D} = \frac{k_1}{2}(\partial_a n_a)^2 + \frac{k_2}{2}(\epsilon_{ab}\partial_a n_b)^2 + \frac{\lambda}{4}(n_a n_a - 1)^2$
2D nematic	Eq. (2.25)	$\mathcal{E}_{simp2D} = \frac{k}{4}(\partial_a N_{bc})(\partial_a N_{bc}) + \frac{\lambda_a}{2}[n_{aa} - 1]^2 + \frac{\lambda_b}{4}[n_{ab}n_{ab} - 1]^2$
3D nematic	Eq. (2.28)	$\mathcal{E}_{simp3D} = \frac{k}{4}(\partial_a N_{bc})(\partial_a N_{bc}) + \frac{\lambda_A}{2}[N_{aa} - 1]^2$ $+ \frac{\lambda_B}{4}[N_{ab}N_{cd} - N_{ac}N_{bd}][N_{ab}N_{cd} - N_{ac}N_{bd}]$

Table 2.1: Free energies and equations of motion for the 2D smectic, nematic, and 3D nematic systems.

are based on SO(2) and SO(3) tensor fields, while the SLC is a simple vector field model. I next turn to the macroscopic (as opposed to microscopic) properties of the director field, and begin a discussion of topological defects.

2.2 Topological defects

Topological defects can be created when a system undergoes a symmetry breaking phase transition. Crudely put, a topological defect is an aberration which is usually very localized, and often easily identified as a singularity in energy density. Whether or not one is created, and what form it may take, is most concisely determined by using results from group theory[Mer79, Mic80], as will be sketched below. The principle concerns are to develop abstractions which describe the degeneracies in minimal energy states of the system under consideration, and to use these abstractions to describe a mapping from physical space to the degeneracy space. Such concerns are fundamentally about the symmetries of a system and how they change.

Symmetry breaking refers to the loss of symmetry in the configuration of a system which occurs when the system is brought from one energy state to a lower one. For example, when a liquid is frozen, the molecules in the resulting solid no longer have isotropic symmetry; instead, they may have a discrete rotational symmetry, or some more complicated symmetry. Many physical systems undergo such symmetry breaking to reach a lower energy state. The classical example is that of a knitting needle, which buckles in one particular direction when compressed by a force applied at both ends along its axis. The result is that the needle is no longer symmetric with respect to rotations about its axis.

2.2.1 Domain Walls

Topological defects arise when large ensembles of objects collectively undergo symmetry breaking. As a simple example, consider a two dimensional ensemble of spins which are free to point either up or down, initially in equilibrium with a heat bath at some high temperature. We can imagine that nearest neighbor molecules are coupled in such a way that they all prefer to be oriented in the same direction. However, because of the hot heat bath, they are jiggling so hard that kT is larger than the coupling energy J. Suppose we now lower the temperature of our heat bath suddenly. As kT becomes smaller than J, the spins begin aligning themselves to each other, forming local patches of up and down-spins. Where these patches meet a wall of high energy forms. There is no way for this "domain wall" to disappear except by growing out to infinity, collapsing by shrinking in, or by annihilating on an opposite polarity counterpart. Domain walls are a class of topological defects.

The formation of domain walls can be predicted by studying the symmetry groups of the high temperature versus the low temperature phases. In the high temperature phase, each spin can be in one of two states, but in the low temperature phase, after the system has settled and is very cold, all the spins are in the same state, either up or down. Mathematically, we say that the spin system has undergone a $\mathcal{Z}_2 \rightarrow \mathcal{Z}_1$ symmetry breaking transition[4]. In this case, the set of possible final states which are equal in energy, otherwise known as the vacuum manifold $\mathcal{M}_0$, is described as $\mathcal{Z}_2$. $\mathcal{Z}_2$ can be represented as two disconnected points. The existence of domain walls can therefore be predicted, on the basis that there is no continuous transformation from one point to another in $\mathcal{M}_0$. The utility of this approach becomes more apparent as more complicated symmetries arise.

2.2.2 Monopoles and Strings, and Homotopy Theory

Consider next a two dimensional lattice of continuous spins, orientable in any direction from 0 to 2π. The symmetry of the high temperature phase of this system is O(2), and the symmetry of the low temperature phase is $\mathcal{Z}_1$, and $\mathcal{M}_0 = \mathcal{S}_1$ (the one-sphere[5]), because the set of possible final states include all 2π directions. Now, we introduce the basic elements of homotopy theory. A uniform field, one with all the spins oriented in the same direction, is shown in Figure 2-4. On top of this

---

[4]The group $\mathcal{Z}_n$ is isomorphic to the additive group of integers, modulo n. In this text, I will use $\mathcal{Z}_1$ to denote the identity, because it arises infrequently in the discussion; in the literature, the identity is usually denoted as 1.

[5]$\mathcal{S}_n$ are groups formed from the set of points on the surface of spheres in $(n + 1)$-dimensional Euclidean space. Such sets can be described by n free parameters. For example, the circle, a sphere in two-dimensional space, is parametrized by θ, and is known as a "one-sphere."

field is shown a closed, oriented contour γ; at all points on this contour, the spins are oriented in the same direction $\phi = \pi/2$ (choose ϕ to be measured from the horizontal, and the origin in the center of the figure). Thus, we say that γ maps to a single point Γ in the phase space of possible orientations, $\mathcal{M}_0$. This is schematically depicted in Figure 2-5.
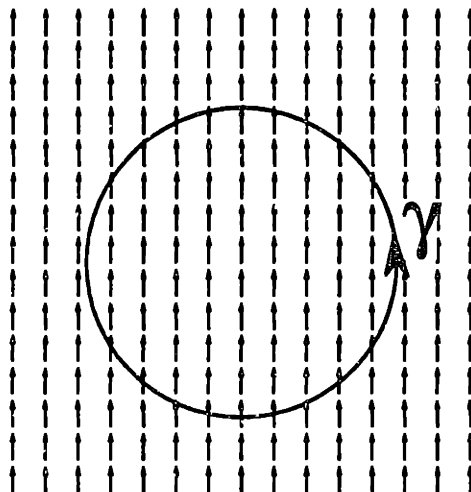
Figure 2-4: A uniform field. The spins on the one-sphere γ are all oriented in the same direction; thus, γ maps to a single point Γ in orientation space.
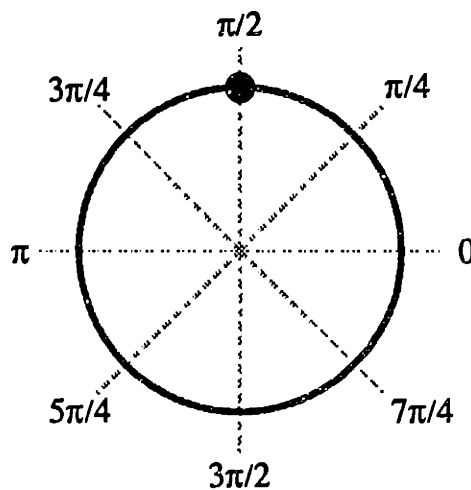
Figure 2-5: Orientation space configuration map. The single point plotted corresponds to a uniform field.

Figure 2-6 shows a sequence in which a warped field configuration is deformed continuously.

22

The rules for deformation are that each spin may be turned by a small angle $d\theta$, but that neighboring spins must be oriented in nearly the same direction (the director field desires to remain as continuous as possible). The analogous deformation sequence in orientation space is shown in Figure 2-7. The circle, or "one-sphere", shown in the figure is a representation of $\mathcal{M}_0$: each point on the circle corresponds to a spin orientation from 0 to 2π. The contours, Γ, correspond to the orientations of the spins in physical space along the contour γ. The fact that the left hand configuration can be deformed continuously into a uniform field is equivalent to the fact that Γ can be shrunk continuously to a point on the one-sphere.
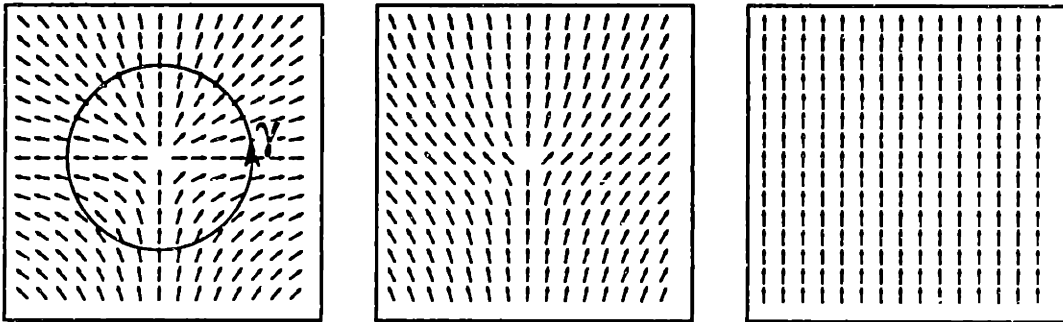
Figure 2-6: The continuous deformation of a warped field to a uniform field. The original field, on the left, is thus nonsingular.
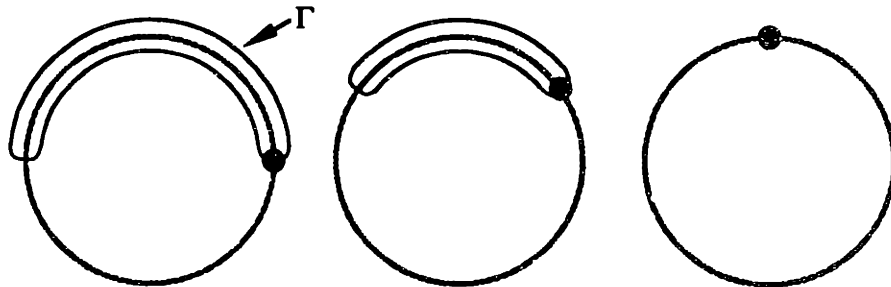
Figure 2-7: Deformation of a warped field shown in orientation space.

The power of homotopy theory is the reversibility of this last statement. Spin orientation configurations for which there exists a mapping from a closed contour γ to a closed contour Γ in orientation space, which cannot be shrunk to a point, belong to a class of configurations which cannot be made to disappear without overcoming a significant energy barrier. Such mappings are known as "non-trivial." Trivial maps are those which lead to Γ which can be shrunk to a point on $\mathcal{M}_0$. Note that

continuous deformations of the field in physical space correspond to allowing the contour Γ to be perturbed continuously on $\mathcal{M}_0$. Also, note that Γ cannot be broken – it must remain a closed contour.

An example of a configuration with a non-trivial $\gamma \rightarrow \Gamma$ map in our model system is shown in Figure 2-8. The contour Γ which corresponds to γ follows a closed path around the one-sphere. No continuous perturbation of Γ allow us to shrink it to a point. Thus, the configuration of Figure 2-8 is one of a class of configurations which are "topologically stable." Other configurations which are topologically related to this one correspond to *rotations* of Γ around $\mathcal{M}_0$, such as those shown in Figure 2-9. This class of topological defects are known as monopoles.
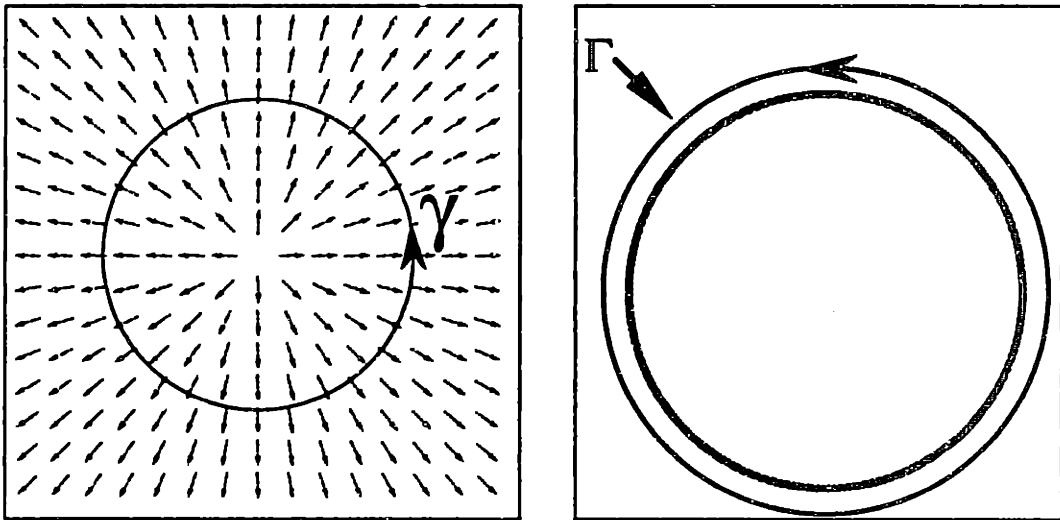
Figure 2-8: Splay energy defect. The picture on the left shows the spin configuration, and the one on the right shows the mapping from the contour γ in physical space to the contour Γ in orientation space. Because Γ cannot be continuously deformed into a point, this spin configuration is topologically stable.

As we have just shown, monopoles are known to exist because there exists a mapping from a closed contour γ in physical space to an unshrinkable contour Γ on $\mathcal{M}_0$. In our particular case, the physical system is two-dimensional, and γ is isomorphic to a one-sphere ($\mathcal{S}_1$). Thus, monopoles correspond to nontrivial maps from $\mathcal{S}_1$ to $\mathcal{M}_0$. Such maps, from $\mathcal{S}_n$ to $\mathcal{M}_0$, are generally written as $\pi_n(\mathcal{M}_0)$. Defects of dimensionality t in a d-dimensional system are classified according to the map $\pi_{d-t-1}(\mathcal{M}_0)$. These categories are summarized in Table 2.2.
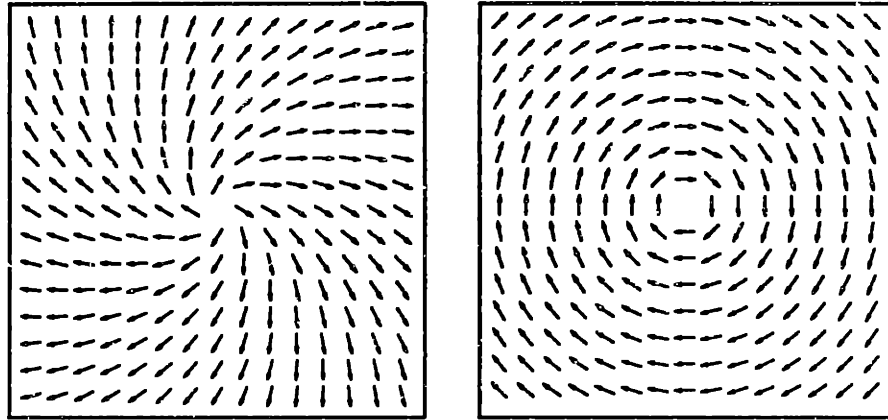
Figure 2-9: Two degenerate energy "bent" splay defects.

Defect	Dimensionality	2D System Homotopy	3D System Homotopy
Domain Walls	2		$\pi_0(\mathcal{M}_0)$
Strings	1		$\pi_1(\mathcal{M}_0)$
Monopoles	0	$\pi_1(\mathcal{M}_0)$	$\pi_2(\mathcal{M}_0)$
Texture	"-1"	$\pi_2(\mathcal{M}_0)$	$\pi_3(\mathcal{M}_0)$

Table 2.2: Homotopy classification of topological defects in 2D and 3D systems.

25

2.2.3 Summary

My discussion of topological defects from a group theoretical standpoint relies primarily on drawing pictures which present the important physics and on developing a general intuition. Unfortunately, the lack of mathematical specifics precludes a discussion of more advanced subjects, such as relative vs. absolute homotopy, and more powerful tools, such as exact homotopy sequences. However, I quote an important result here. As will be discussed in the next chapter, the vacuum manifold of the NLC[KMT77] is S_2/Z_2. Mathematicians would say about the NLC that "using an exact homotopy sequence, it can be shown that the homotopy of $\mathcal{M}_0$ is as follows: $\pi_1(\mathcal{M}_0) = Z_2$, $\pi_2(\mathcal{M}_0) = Z$, $\pi_3(\mathcal{M}_0) = Z$." The meaning of this statement is that we should expect to find one type of string, integrally charged monopoles, and integrally charged texture, in the NLC. For more details, the reader is kindly referred to group theory texts, or Mermin's excellent review of the subject[Mer79].

2.3 Summary

The two sections in this chapter have discussed the microscopic and the macroscopic properties of systems made of rod-like molecules with certain continuous symmetries. In Section 2.1, we learned that the order parameter Q_{ab} of the NLC is given by a function of its director field $\vec{n}$. The free energy, when expanded in powers of Q, shows the existence of a first-order symmetry breaking phase transition. The symmetries of the low temperature, nematic phase, give rise to the Frank free energy, from which can be derived equations of motion governing the dynamics of $\vec{n}$.

As we will see in Chapter 4, these equations of motion will naturally lead to the creation of topological defects when applied to an initial configuration with random, isotropically distributed rod orientations. Section 2.2 presented a group theory based understanding of why particular topological defects exist, and how to predict their existence based on the fundamental symmetries of the system under study. The NLC, for which $\mathcal{M}_0$ is S^2/Z_2, the two-sphere with antipodal points identified, allows the existence of monopoles, strings, and texture.

The next chapter will begin to unify the theory presented in this chapter. And in Chapters 4 and 5, I will begin applying this knowledge of topological defects and field equations to numerical simulations and experimental observations of liquid crystal systems.

26

Chapter 3

Defect Structure

In this chapter, I summarize our understanding of NLC defect structures. First, I consider defects in two-dimensional systems. Defects in three-dimensional systems have similar fundamental structure, but are significantly complicated by extra degrees of freedom. Also, in $\mathcal{R}^3$, monopoles and texture defects arise, while the ± 1 defects of the $\mathcal{R}^2$ become non-singular. Throughout the discussion, I concentrate on visualizing the defects by imagining a volume filled with stiff rods. In Section 3.5, I show that a comparison between the energy density in a volume ξ containing different defects can be used to estimate the evolution of the relative defect abundances as ξ grows. The model I use in my analysis is known as the "equal constant" approximation; in the non-equal constant case, defect structure solutions do change slightly, but little enough to leave the main conclusions and pictoral intuition intact.

3.1 Defects in $\mathcal{R}^2$

The isotropic→nematic phase transition in a thin, essentially two-dimensional layer of NLC can properly be described as an $O(2)/\mathcal{Z}_2 \rightarrow \mathcal{Z}_2$ symmetry breaking transition[1]. Initially, in the high temperature isotropic phase, the molecules of the liquid crystal are free to point in whatever direction they please, but after the transition, the molecules gradually relax to a state in which they all point in one particular direction. The final state is $\mathcal{Z}_2$ symmetric because of the inversion symmetry of the rod-like molecules of the nematic. Because the final orientation of the molecules is undetermined,

---

[1] Note that the group $O(n)$ refers to the set of rigid body rotations in n-dimensional Euclidean space. Thus, $O(n)$ can be characterized by $n - 1$ free parameters.

Charge	Director field
+1	$\vec{n} = \cos\phi\hat{x} + \sin\phi\hat{y}$
-1	$\vec{n} = -\cos\phi\hat{x} + \sin\phi\hat{y}$
$+\frac{1}{2}$	$\vec{n} = \cos\frac{\phi}{2}\hat{x} + \sin\frac{\phi}{2}\hat{y}$
$-\frac{1}{2}$	$\vec{n} = -\cos\frac{\phi}{2}\hat{x} + \sin\frac{\phi}{2}\hat{y}$

Table 3.1: Director field structure of ± 1 and $\pm\frac{1}{2}$ defects in $\mathcal{R}^2$.

the set of possible minimal energy configurations, otherwise known as the vacuum manifold $\mathcal{M}_0$, is a one-sphere with opposite points identified $\mathcal{S}_1/\mathcal{Z}_2$.

The isotropic→smectic-C transition is similar to the isotropic→nematic transition, but is not complicated by the presence of an inversion symmetry. It is described simply as a $O(2)\to\mathcal{Z}_1$ symmetry breaking transition, with $\mathcal{M}_0 = \mathcal{S}_1$. Thus, as discussed in the last chapter, monopoles, which correspond to nontrivial $\pi_1(\mathcal{M}_0)$, will exist in the smectic. These monopoles are known as charge ± 1 monopoles; the topological charge m of a defect is calculated as an integral over the director field on a closed loop γ which encloses the defect in question:

$$m = \frac{1}{2\pi}\oint_\gamma \vec{\nabla}\theta \, d\vec{l}, \qquad (3.1)$$

where $\theta = \tan^{-1}(n_y/n_x)$ gives the orientation of the director field elements. Rod pictures of $+1$ and -1 monopoles are shown in Figures 4-1 and 4-2.

Topological charge $\pm\frac{1}{2}$ monopoles will also exist in the nematic, because of the additional $\mathcal{Z}_2$ symmetry. Closed contours in physical space along which θ varies from 0 to $\pi/2$ will correspond to nontrivial $\pi_1(\mathcal{M}_0)$, because of the identification of antipodal points of $\mathcal{S}_2/\mathcal{Z}_2$. Table 3.1 gives the director field $\vec{n}$ for ± 1 and $\pm\frac{1}{2}$ monopoles in R_2, and Figure 3-1 shows a rod picture of a $+\frac{1}{2}$ monopole. Other configurations, which correspond to global rotations of $\vec{n}$, are equivalent (in the equal constant approximation).

These defects can be observed under a microscope by placing a thin preparation of liquid crystal material between crossed polarizers, to produce what is known as a "Schlieren" image. Regions in which the molecules are oriented at $\pi/4$ with respect to the polarizers are brightest, while regions oriented close to the directions of either polarizer are the darkest. ± 1 monopoles produce four alternating light-dark bands (sometimes described as a Maltise cross pattern), and $\pm\frac{1}{2}$ monopoles,

28
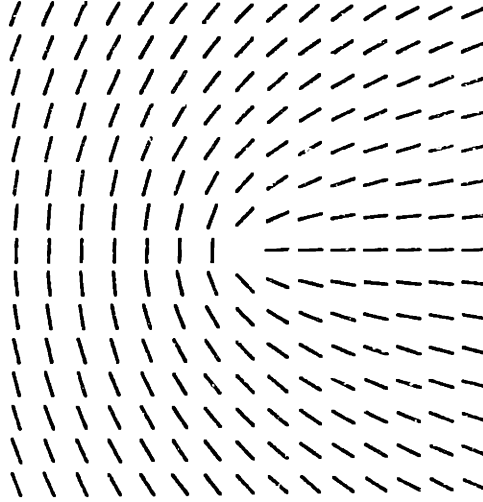
Figure 3-1: Director field of a $+\frac{1}{2}$ monopole.

two bands.

Note that two oppositely charged monopoles will attract each other and eventually annihilate. The director field configuration for a pair of monopoles is given by $\theta = (\theta_1 - \theta_2)/s$, where $s = 1$ or 2 for ± 1 and $\pm \frac{1}{2}$ monopoles, respectively.

Finally, I mention a few details concerning the actual structure of the core of a monopole. As given in Table 3.1, monopole cores are singularities in energy. In reality, this cannot be the case. Some believe that in the NLC, the core is actually composed of a higher energy phase, i.e., of isotropic fluid[KL88]. In the NLC, the core size is believed to be somewhere in the range of $r_c \approx 10$ to 100 Å in size. This length scale is much smaller than the length scales ξ normally observed experimentally.

3.2 Strings

Topological defects in the three dimensional NLC can be complicated, because not only are strings, monopoles, and texture possible, but also because there may be many different kinds of each.

First, consider strings. In the most naive approach, strings may be constructed by taking $\mathcal{R}^2$ defects and sweeping out world lines with their cores. However, this neglects the possibility for the molecules to twist out of the plane (along the direction of the string), thus allowing ± 1 strings to become nonsingular. Director field configurations for singular core strings are given in cylindrical

29

coordinates by

$$\vec{n} = \mathbf{O}\left[\hat{x}\cos(s\phi) \pm \hat{y}\sin(s\phi)\right], \tag{3.2}$$

where $s = 1$ or $1/2$ for ± 1 and $\pm\frac{1}{2}$ strings, respectively, and $\mathbf{O}$ is a global rotation matrix, as before.

± 1 strings can have very low energy density, by becoming very broad, diffuse objects. This property, known as their ability to "escape,"[2] can be justified from group theory arguments. The isotropic→nematic transition is a $SO(3)$→$O(2)$ symmetry breaking transition; before the transition the molecules find themselves free to orient in any direction, and afterwards, they all line up in one particular direction. The vacuum manifold is the quotient group $SO(3)/O(2)$ and is found to be $\mathcal{S}_2/\mathcal{Z}_2$, the two-sphere with antipodal points identified[3]. A closed contour in physical space enclosing the center of a $\pm\frac{1}{2}$ string would correspond to a closed contour $\Gamma_{\frac{1}{2}}$ in symmetry space, on the two-sphere, from the north pole to the south pole; the north and south poles are actually the same point (Figure 3-2). There is no way to continuously deform $\Gamma_{\frac{1}{2}}$ into a single point on the two-sphere, because of the "anchoring" properties of the antipodal points denoted "N" and "S" in the Figure; shrinking $\Gamma_{\frac{1}{2}}$ to the left, away from the north pole, would necessitate warping the bottom part of the curve towards the right, away from the south pole. On the other hand, a closed contour in physical space enclosing the center of a ± 1 string would correspond to a closed contour Γ_1 in symmetry space forming a great circle (Figure 3-3). Clearly, Γ_1 can be deformed continuously to simply roll it off the top of the sphere into a point. Mathematically, it is said that ± 1 strings have trivial $\pi_2(\mathcal{M}_0)$ homotopy.

A physical picture which justifies the non-singular nature of "escaped" ± 1 strings can be constructed by considering the ± 1 and $\pm\frac{1}{2}$ defects in $\mathcal{R}^2$, with an additional degree of freedom in which the rods of the director field are allowed to swivel out of the plane. First, consider the string given by

$$\vec{n} = \hat{x}\cos\chi\cos\phi + \hat{y}\cos\chi\sin\phi + \hat{z}\sin\chi, \tag{3.3}$$

with $\chi = 0$ far away from the origin. Now, imagine that towards the origin, χ gradually increases to $\pi/2$, whereupon the rods all tilt upwards out of the plane. Recalling the equal-constant expression

---

[2]This is also refered to in the literature as "escape in the third dimension" (see [CK72, WPC72b]).

[3]The symmetry group may equally well be taken to be $O(3)$ broken to D_∞, but since the corresponding orbits are the same, $O(3)\vec{n} = SO(3)\vec{n}$, it is sufficient to consider $SO(3)$ broken to $O(2)$.
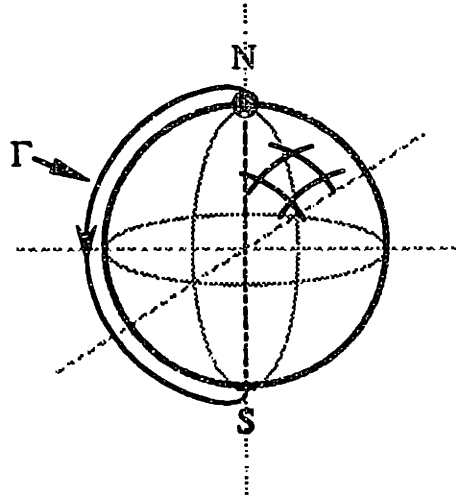
Figure 3-2: Diagram showing a nontrivial $\pi_1(\mathcal{M}_0)$ map corresponding to a $+\frac{1}{2}$ string in the NLC. $\mathcal{M}_0 = \mathcal{S}_2/\mathcal{Z}_2$, the two-sphere with antipodal points identified. The contour Γ cannot be deformed continuously into a point because the two points marked "N" and "S" are constrained to remain opposite each other at all times.
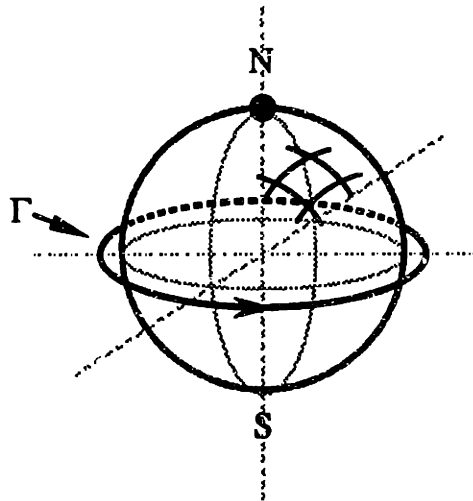
Figure 3-3: Diagram showing a trivial $\pi_1(\mathcal{M}_0)$ map corresponding to a $+1$ string in the NLC. $\mathcal{M}_0 = \mathcal{S}_2/\mathcal{Z}_2$, the two-sphere with antipodal points identified. The contour Γ can be deformed continuously into a point by simply rolling it up to the top of the sphere.

for the energy density

$$\mathcal{E} = (\partial_a n_b)^2 = \sum_i (\nabla n_i)^2 \,, \tag{3.4}$$

we see that because the rods are no longer pointing towards each other, and in fact become parallel to each other at the origin, the energy density is minimal.

$\pm \frac{1}{2}$ strings can be written as $\vec{n} = \mathbf{O}\left[\hat{x}\cos(\phi/2) + \hat{y}\sin(\phi/2)\right]$, where $\mathbf{O}$ is a constant rotation matrix. Compare this picture with that of a $\pm\frac{1}{2}$ defect which tries to escape; the director field is shown in Figure 3-1. Imagine the rods trying to lift themselves out of the plane as they approach the origin, remembering that $\vec{n}$ wants to remain as continuous as possible (the higher ∂n, the higher the energy cost). We see that because of the extra bend in the $\pm\frac{1}{2}$ defects, the director does not want to tilt upwards out of the plane.

Other forms of ± 1 defects exist; in particular, there exists the $+1$ $\mathcal{R}^2$ monopole whose rods are arranged along concentric circles. This and all the other ± 1 defects may escape to become nonsingular; one possibility would be for the rods in the circles to gradually twist themselves as they near the center, until they are arranged as in Eq. (3.3), which we have already seen can escape. Finaly, a matter of nomenclature: because ± 1 strings can become nonsingular, I shall somtimes refer to them as flux tubes rather than as strings. When ± 1 strings escape to become nonsingular, they are seen as fuzzing out and becoming very broad.

3.3 Monopole Structure

Monopoles exist in three as well as in two dimensions, although they have many more degrees of freedom in $\mathcal{R}^3$. Their structure can be visualized by thinking of a curled up hedgehog (or a porcupine), which has all its quills pointing out from its center. In spherical coordinates, the orientation of the director field of a monopole would be given by its θ, ϕ position, such that the field always points inward towards the origin. All other monopole configurations may be produced by globally rotating the $\vec{n}$ of the hedgehog. In cartesian coordinates, this configuration is written as

$$\vec{n} = \mathbf{O}\left[\cos\phi\sin\theta\hat{x} + \sin\phi\sin\theta\hat{y} + \cos\theta\hat{z}\right]\,. \tag{3.5}$$

Typically, the flux coming out of a monopole bunchs up into two tubes going in opposite directions out from (or in to) the monopole. Thus, monopoles are observed as blips of highly concentrated energy

(black dots) sitting on ±1 flux tubes. Again, because ±1 strings can escape to become nonsingular objects, the flux tubes coming out of a monopole may quickly disappear into nothingness, but at the monopole itself, the flux is necessarily pinched into a point. Furthermore, in order for a monopole to be formed, the two ±1 strings on either side of the monopole must be escaped in opposite directions, and their charges must be the same.

The topological charge of an isolated monopole is arbitrary, but the relative charge of two monopoles is well-defined. It is determined by the charge of the ±1 strings connecting them. Because $\pi_2(\mathcal{M}_0) = Z$, we know that topological charge $0, \pm 1, \pm 2, \dots$ exist. However, it would be impossible to determine if a monopole formed by the intercommutation of two ±1 strings were of charge 0 or ±2.

3.4 Texture Structure

Texture is a completely nonsingular topological defect, except when it forms a singularity for an instant as it collapses. Mathematically, texture corresponds to homotopically nontrivial maps from $\mathcal{S}_3$ to $\mathcal{S}_2$ (i.e., nontrivial $\pi_3(\mathcal{M}_0)$); they are a special case of the Hopf fibration[Ste51]. They are constructed as follows: using the fact that $SU(2)$ is isomorphic to $\mathcal{S}_3$, a map from a uniform field onto $SU(2)$ can be written as $g(\vec{x}) = \exp(i\chi(r)\vec{x} \cdot \vec{\sigma}/r)$, with the Pauli matrices $\vec{\sigma}$ and $\chi(r)$ a function running from 0 at the origin to π at infinity. Subsequently, $g(\vec{x})$ is mapped onto $\mathcal{S}_2$ using $\vec{n}(\vec{x}) \cdot \vec{\sigma} = g(\vec{x})\sigma_3 g(\vec{x})^{-1}$. The resulting director field is:

$$\vec{n} = (\frac{xz}{r^2}(1 - \cos 2\chi) - \frac{y}{r}\sin 2\chi, \frac{yz}{r^2}(1 - \cos 2\chi) + \frac{x}{r}\sin 2\chi, \frac{z^2}{r^2}(1 - \cos 2\chi) + \cos 2\chi). \quad (3.6)$$

This configuration may be viewed as two concentric, escaped ±1 strings of opposite charge. There are no singularities anywhere, but by Derrick's theorem[Der64], the configuration must collapse and unwind itself, or be stabilised by higher derivative terms (this possibility was considered in [WZ89]). To see that the configuration is topologically nontrivial, and must produce a singularity in the unwinding process, consider lines of constant $\vec{n}$ in space. These lines form two rings about the z axis which link once (this is known as a Hopf link). If the configuration is to relax to a configuration of constant $\vec{n}$, these linked lines must cross. It being impossible for $\vec{n}$ to take two values at once, there must be a singularity produced at the crossing point. Bouligand has actually observed such linked

rings in a cholesteric liquid crystals[Bou81, Bou74].

Although texture contains no singularities, i.e., the director field of a texture cannot be deformed continuously into a homogeneous state, texture is properly classified as a topological soliton [Sha77].

Unfortunately, a precise balance in centering the two ±1 strings seems to be critical in determining whether or not a texture defect will decay through the expected mechanism, by collapsing and unwinding itself (it is expected that the inner loop collapses first, forming a monopole which is later annihilated when the outer loop collapses around the same point). If the two strings are not perfectly concentric, it is possible for the two loops to intersect at a single point, while they are shrinking. At this intersection, an intercommutation will occur, leaving behind two monopoles sitting on the ends of the two broken rings[4]. The monopoles quickly recede from each other and eventually annihilate. I discuss this scenario further in Section 5.4.

3.5 Defect Energetics

A possible measure for the relative abundances of defects is given by a comparison between their energy densities and how that behaves versus the length scale of the system. In this section, I first consider how such energies are calculated, and then proceed with the calculation for the monopole, $\pm\frac{1}{2}$ string, and escaped ±1 string.

3.5.1 Calculating E_{defect} in a Volume ξ^3

Consider a volume of space with length scale ξ containing a monopole or a section of a string. Neglecting the core energies of the defects, what is the total energy E contained in this space? We can calculate the energy density $\mathcal{E}$ using the equal-constant expression:

$$\mathcal{E}_{\text{equal constant}} = \frac{k}{2}(\partial_a n_b)^2 . \tag{3.7}$$

---

[4]Does this mean that the two strings must be escaped in the same θ direction? The equations show that the strings are escaped in *opposite* directions!

The total field energy (recalling that $\mathcal{E}_{\text{equal constant}} = \mathcal{E}_{lc}$ with our definitions) is given by the integral of $\mathcal{E}$ over the space, possibly with some cutoff limit at the core:

$$E = \int_{\tau_c}^{\xi} \mathcal{E} r^2 \sin\theta \, dr \, d\theta \, d\phi \tag{3.8}$$

However, Eq. (3.7) neglects a surface term which appears in the Frank free energy, Eq. (2.7). We can calculate this contribution separately, as follows:

$$\mathcal{E}_{lc} = \mathcal{E}_{\text{equal constant}} + \mathcal{E}_{\text{surface}} \tag{3.9}$$

$$\mathcal{E}_{\text{surface}} = \frac{k-k_4}{2}\left[(\partial_a n_a)^2 - (\partial_b n_a)(\partial_a n_b)\right] = \frac{k-k_4}{2}\vec{\nabla}\cdot\vec{G}, \tag{3.10}$$

where I have defined $\vec{G}$ as the surface component (or otherwise known as the "saddle-splay-curvature" term) of the energy density to be:

$$\vec{G} = \vec{n}(\vec{\nabla}\cdot\vec{n}) - (\vec{n}\cdot\vec{\nabla})\vec{n}. \tag{3.11}$$

Setting $k_4 = 0$, the surface term contribution to the energy is thus given by:

$$E_{\text{surface}} = \int \mathcal{E}_{\text{surface}} \, d\vec{x} = \frac{k}{2}\oint \vec{G}\cdot\hat{r}\, dS. \tag{3.12}$$

Though the surface term does not contribute to the equations of motion which describe the dynamical behavior of a particular defect, it does contribute to the energy of a defect.

Whether or not the surface term should be included is a judgement which can be based on the nature of the problem under study. If it is desired that all solutions should be related by global rotations, then the equal constant expression, Eq. (3.7), should be used, because it is invariant under global rotations of $\vec{n}$. On the other hand, when a surface term is included, this symmetry is broken. Also, the individual terms in the Frank free energy are clearly not invariant under global rotations. In the following discussion, I will separately present both the field and surface term energies.

35

3.5.2 Monopole Energy Density

Using Eq. (3.5), and the definition of the gradient $\vec{\nabla} = \hat{r}\partial_r + \hat{\theta}\frac{1}{r}\partial_\theta + \hat{\phi}\frac{1}{r\sin\theta}\partial_\phi$ in spherical coordinates, we calculate the derivatives of n_i to be

$$
\begin{aligned}
\vec{\nabla} n_x &= \hat{\theta}\frac{1}{r}\cos\theta\cos\phi - \hat{\phi}\frac{1}{r}\sin\phi \\
\vec{\nabla} n_y &= \hat{\theta}\frac{1}{r}\cos\theta\sin\phi + \hat{\phi}\frac{1}{r}\cos\phi \\
\vec{\nabla} n_z &= -\hat{\theta}\frac{\sin\theta}{r} .
\end{aligned}
\tag{3.13}
$$

The energy density is found to be $\mathcal{E} = \frac{k}{2}\left[(\vec{\nabla} n_x)^2 + (\vec{\nabla} n_y)^2 + (\vec{\nabla} n_z)^2\right] = \frac{k}{r^2}$, and the total energy in a sphere of radius ξ is given by an integral over space to be

$$
E_{\text{monopole}} = 4\pi k\xi .
\tag{3.14}
$$

The energy contributed by the surface term of $\mathcal{E}_{lc}$ is given by calculating $\vec{G}$ from Eq. (3.11). We use the fact that in spherical coordinates, our monopole is given by $\vec{n} = \hat{r}$, to get $\vec{G} = 2\hat{r}/r$. The integral of Eq. (3.12) is trivial:

$$
E_{\text{surface}} = \frac{k}{2}\oint\left(\frac{2\hat{r}}{r}\right)\cdot\hat{r}r^2\,d\Omega = 4\pi k\xi
\tag{3.15}
$$

where we have evaluated the integral on a sphere of radius $r = \xi$.

3.5.3 Singular String Energy Density

The energy density of a localized ± 1 or $\pm\frac{1}{2}$ string is calculated by using as the director field:

$$
\vec{n} = \hat{x}\sin(s\phi) + \hat{y}\cos(s\phi) ,
\tag{3.16}
$$

with $s = \pm\frac{1}{2}$ for $\pm\frac{1}{2}$ strings and $s = \pm 1$ for ± 1 strings. The derivatives are calculated in cylindrical coordinates to get:

$$
\begin{aligned}
\vec{\nabla} n_x &= \hat{\phi}\frac{s}{r}\cos(s\phi) \\
\vec{\nabla} n_y &= -\hat{\phi}\frac{s}{r}\sin(s\phi)
\end{aligned}
\tag{3.17}
$$

$$\vec{\nabla} n_z = 0,$$

and the energy density follows immediately, giving $\mathcal{E} = \frac{ks^2}{2r^2}$. The total field energy per unit length of string is given by an integral in cylindrical coordinates:

$$\frac{dE_{\text{singular string}}}{dl} = \int_{r_c}^{\xi} \mathcal{E} r\, dr\, d\phi = \pi s^2 k \ln\left(\frac{\xi}{r_c}\right). \tag{3.18}$$

The energy of a $\pm\frac{1}{2}$ string in a volume of scale ξ^3 is therefore given by setting $s = \frac{1}{2}$ and multiplying by the string length ξ:

$$E_{\text{singular string}} = \frac{\pi}{4} k \xi \ln\left(\frac{\xi}{r_c}\right). \tag{3.19}$$

We can calculate the surface term contribution by re-expressing the director field in cylindrical coordinates as:

$$\vec{n} = \hat{r} \sin(s'\phi) + \hat{\phi} \cos(s'\phi), \tag{3.20}$$

where $s' \equiv s + 1$. The $\hat{r}$ component of $\vec{G}$ is thus:

$$G_r = n_r(\vec{\nabla} \cdot \vec{n}) - (\vec{n} \cdot \vec{\nabla})n_r = \frac{s'-1}{r}\sin^2(s'\phi) - \frac{s'-1}{r}\cos^2(s'\phi) = \frac{1-s'}{r}\cos(2s'\phi). \tag{3.21}$$

It follows that because the surface integral

$$(1 - s')\oint_0^{2\pi} \cos(2s'\phi)\, d\phi = 0, \tag{3.22}$$

for s' of the form $m/2$, where m is an integer, there is no surface energy contribution.

$$E_{\text{surface}} = 0. \tag{3.23}$$

3.5.4 Escaped String Energy Density

Another case is that of an escaped ± 1 string, with a director field configuration as given by Eq. (3.3). Here the derivatives (again, in cylindrical coordinates) are:

$$\vec{\nabla} n_x = \hat{r} \cos\chi \cos\phi \partial_r \chi - \hat{\phi}\frac{1}{r}\sin\chi\sin\phi \tag{3.24}$$

$$\vec{\nabla} n_y = \hat{r} \cos\chi \sin\phi \partial_r \chi + \hat{\phi}\frac{1}{r}\sin\chi\cos\phi$$

37

$$\vec{\nabla} n_z = -\hat{r} \sin\phi \partial_r \chi \, .$$

χ is a function only of radius r which parametrizes the escape of the string. We will calculate this function by variationally minimizing the energy. The energy density is given by the sum of the squares of the above derivatives

$$\mathcal{E} = \frac{k}{2} \left[(\partial_r \chi)^2 + \frac{1}{r^2} \sin^2 \chi \right] \, , \tag{3.25}$$

and the total energy per unit length is calculated from the integral

$$\frac{dE}{dl} = \int_0^\xi \mathcal{E} r \, dr \, d\phi = k\pi \int_0^R \left[r(\partial_r \chi)^2 + \frac{\sin^2 \chi}{r} \right] dr \, . \tag{3.26}$$

Minimizing E by varying χ gives the equation of motion:

$$\partial_r \left[r \partial_r \chi \right] - \frac{\sin\chi \cos\chi}{r} = 0 \, . \tag{3.27}$$

which, with the boundary conditions that $\chi(r = 0) = 0$ and $\chi(r \to \infty) = \pi/2$, gives us the first order differential equation

$$(r \partial_r \chi)^2 = A^2 - \cos^2 \chi \, , \tag{3.28}$$

and $A = \pm 1$. Integrating this equation gives us our final expression for χ, the function parameterizing the string escape:

$$\chi = 2 \tan^{-1} \left(\frac{r}{\xi} \right) \, . \tag{3.29}$$

This expression can be substituted into Eq. (3.26) to give the final total energy per unit length for an escaped ± 1 string:

$$\frac{dE_{\text{escaped string}}}{dl} = 2\pi k \, . \tag{3.30}$$

The total field energy of an escaped ± 1 string in a volume of scale ξ^3 is thus:

$$E_{\text{escaped string}} = 2\pi k \xi \, . \tag{3.31}$$

The surface term contribution is straightforward to calculate. Eq. (3.24) is rewritten in cylindrical

38

Defect	Field energy	Surface energy	Total energy
Monopole	$4\pi k\xi$	$4\pi k\xi$	$8\pi k\xi$
Localized $\pm\frac{1}{2}$ string	$\frac{\pi}{4}k\xi\ln\left(\frac{\xi}{r_c}\right)$	0	$\frac{\pi}{4}k\xi\ln\left(\frac{\xi}{r_c}\right)$
Escaped ±1 string	$2\pi k\xi$	$\pi k\xi$	$3\pi k\xi$

Table 3.2: Comparison of defect energies. The field and surface energies of a monopole, a singular string defect, and a nonsingular string defect in a volume of characteristic length scale ξ^3 are tabulated.

coordinates as:

$$\vec{n} = \hat{r}\sin\chi + \hat{z}\cos\chi, \tag{3.32}$$

and the radial component of $\vec{G}$ is found to be:

$$G_r = n_r(\vec{\nabla}\cdot\vec{n}) - (\vec{n}\cdot\vec{\nabla})n_r = \frac{1}{r}\sin^2\chi. \tag{3.33}$$

G_z is zero, so there is no contribution from the top and bottom surfaces of the integration cylinder. The surface integral makes use of Eq. (3.29), and the radius is evaluated at $r = \xi$ to arrive at the final expression for the surface energy contribution:

$$E_{\text{surface}} = \frac{k\xi}{2}\oint G_r r\,d\phi = \pi k\xi. \tag{3.34}$$

I note that our results are in agreement with those found in the literatue[CK72, WCK73], but the derivation I have presented is simpler.

3.5.5 Comparison of Defect Volumetric Energies

The various defect energetics are summarized in Table 3.2. Knowing that $\xi \propto t^{1/2}$ (a scaling relationship which will be discussed in section 5.2.3) the $\pm\frac{1}{2}$, and ±1 string and monopole energies can be rewritten as functions of time, thus giving some very general criteria for judging when one defect population should be larger than another. A qualitative plot of the three energies Figure 3-4, shows the existence of three "epochs," the first of which could be dominated by $\pm\frac{1}{2}$ strings, followed by ±1 strings and monopoles. Though such a comparison is crude at best, at least it does provide a prediction for the evolutionary growth of the three defect populations.
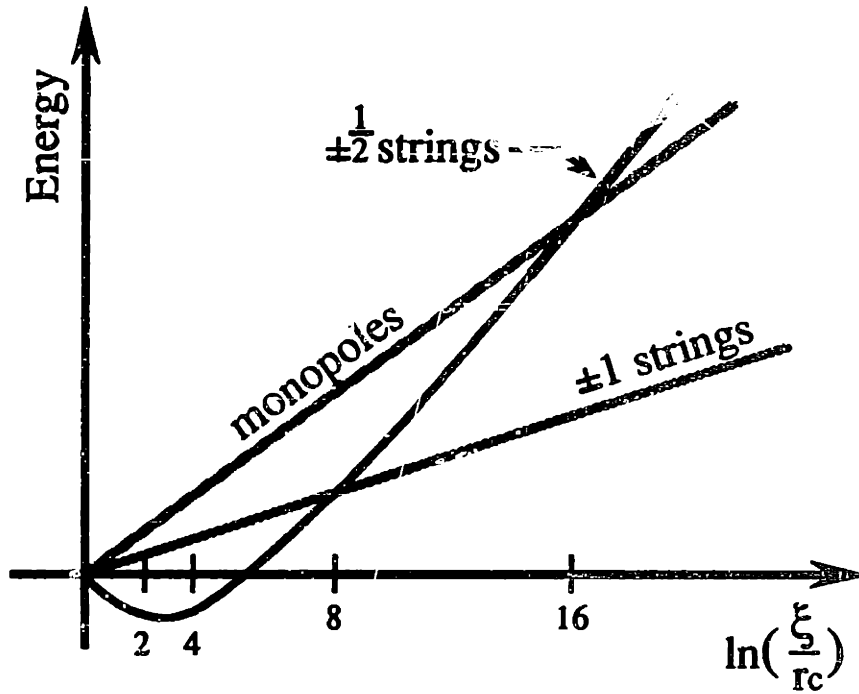
Figure 3-4: Qualitative plot showing the scaling of defect energies in a volume ξ^3, where ξ is the characteristic length scale. Field energies of monopoles, $\pm\frac{1}{2}$ strings, and escaped ± 1 strings are plotted (see Table 3.2 for surface term contributions). Until $\xi \approx r_c e^8$, $\pm\frac{1}{2}$ strings are energetically favored to dominate the system. In the next "epoch," from $\xi \approx r_c e^8$ to $r_c e^{16}$, ± 1 strings become dominant. In the final stage, monopoles become favored over $\pm\frac{1}{2}$ strings.

3.6 The Non-equal Constant Case

The equations of motion derived from the equal-constant approximation to the energy density Eq. (2.6) posses full internal and spatial rotational symmetries. In this model, we expect that all defects related by internal rotations would occur with equal abundances in the bulk. However, these symmetries are broken in the real system, in which the k_i are unequal. I briefly note here the differences which appear, and how they can be quantified.

The structure of the minimal energy monopole in the unequal k_i case can be calculated by minimizing $\delta\mathcal{E}/\delta O$, where O is the global rotation matrix as discussed previously, and the energy density $\mathcal{E}$ is taken as a functional of k_i. Turok has shown that when $\delta k_1 = \delta k_2 > 0$, $\delta k_2 = 0$, the minimal energy monopole for free boundary conditions is given (up to rigid rotations) by $\vec{n} = \hat{x}\sin\theta\cos(\phi - 2\pi/3) + \hat{y}\sin\theta\sin(\phi - 2\pi/3) + \hat{z}\cos\theta$. As long as the δk_i are different, the minimal energy solution is cylindrically, rather than spherically symmetric.

Goldhaber has shown that monopoles in the one-constant approximation have an additional degeneracy in energy, given by a class of deformations which, at no cost in energy, concentrate all the flux-lines from a monopole into a single arbitrarily thin tube[Gol89]. However, the unequal k_i monopole solution given above can be shown to be stable under Goldhaber's deformation. Thus, monopoles survive in cylindrically symmetric, stable configurations.

The family of $\pm\frac{1}{2}$ string solutions which are degenerate under $\delta k_i = 0$ can be envisioned as strings which are high in twist, bend, or splay energy, or combinations of two of the three. For $\delta k_1 = \delta k_2 > 0$, and $\delta k_3 = 0$, the minimal energy solutions are given by rigid rotations of $\vec{n} = \hat{x}\cos(\phi/2)\pm\hat{z}\sin(\phi/2)$, a solution in which the director twists out of the plane perpendicular to the string as it is encircled in space.

3.7 Summary

The defects in two and three dimensional systems are summarized in Table 3.3, and pictures of the director field of $\mathcal{R}^2$ defects are shown in Table 3.7. By studying the s·aling behavior of the energy densities of monopoles, escaped ±1 strings, and $\pm\frac{1}{2}$ strings in the $\mathcal{R}^3$ NLC, we have found that there are distinct "epochs" in which one of the three defects has a distinctly lower volumetric energy density, suggesting that the defect population of an evolving system which has reached a scaling state

System	$\mathcal{M}_0$	Homotopy	Defect	Director
2D SLC	$\mathcal{S}_1$	$\pi_1(\mathcal{M}_0)$	± 1 monopoles	$\vec{n} = \hat{x}\cos\phi \pm \hat{y}\sin\phi$
2D NLC	$\mathcal{S}_1/\mathcal{Z}_2$	$\pi_1(\mathcal{M}_0)$	± 1 monopoles	$\vec{n} = \hat{x}\cos\phi \pm \hat{y}\sin\phi$
		$\pi_1(\mathcal{M}_0)$	$\pm\frac{1}{2}$ monopoles	$\vec{n} = \hat{x}\cos\phi/2 \pm \hat{y}\sin\phi/2$
3D NLC	$\mathcal{S}_2/\mathcal{Z}_2$	$\pi_1(\mathcal{M}_0)$	± 1 strings (nonsingular)	$\vec{n} = \hat{x}\sin\chi\cos\phi \pm \hat{y}\sin\phi + \hat{z}\cos\chi$
		$\pi_1(\mathcal{M}_0)$	$\pm\frac{1}{2}$ strings (singular)	$\vec{n} = \hat{x}\cos\phi/2 \pm \hat{y}\sin\phi/2$
		$\pi_2(\mathcal{M}_0)$	monopoles	$\vec{n} = \frac{x}{r}\hat{x} + \frac{y}{r}\hat{y} + \frac{z}{r}\hat{z}$
		$\pi_3(\mathcal{M}_0)$	texture	Eq. (3.6)

Table 3.3: Summary of defect structures.

will be dominated by $\pm\frac{1}{2}$ strings at first, followed by escaped ± 1 strings, then by monopoles.
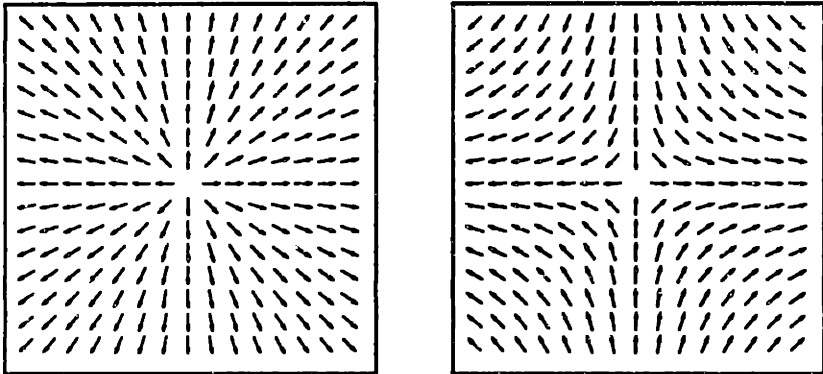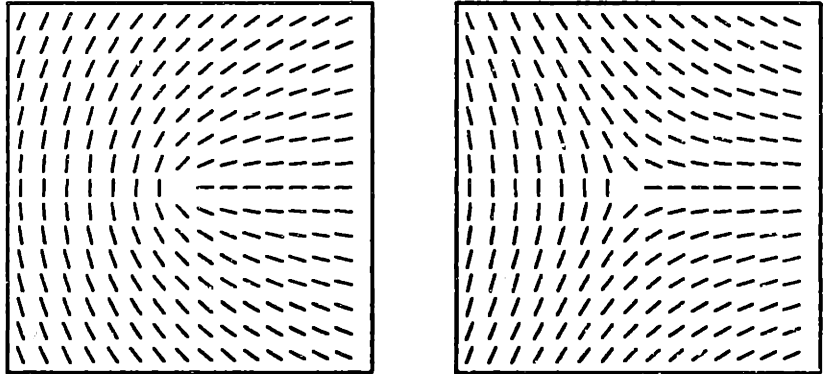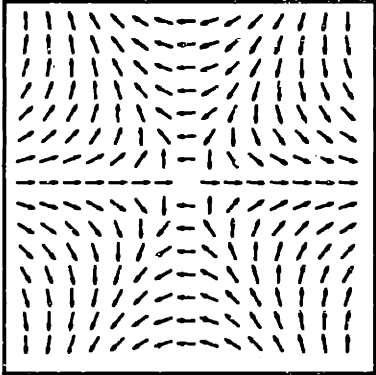
Defect Structure		Description
		$+1, -1$ monopoles
		$+\frac{1}{2}, -\frac{1}{2}$ monopoles
		-2 monopole

Table 3.4: Structures of topological defects in the 2D NLC.

Chapter 4

Numerical Simulations

Numerical integration of the SLC and NLC equations of motion for a system composed of a lattice of vector and tensor spins provides a valuable tool for investigating the dynamical behavior of the defects discussed in the last chapter. Observables which can be measured include the structure function and the monopole density. Also, the evolution of a system can be monitored through generation of crossed polarizer, energy density, and director field pictures. I will discuss my simulation results in order of increasing complexity, beginning with the 2D SLC, then the 2D NLC, and finally the 3D NLC.

4.1 The 2D Smectic

The 2D SLC is the simplest system to study numerically. As discussed in Chapter 3, the 2D SLC is populated by only ± 1 monopoles. These monopoles are formed with linear combinations of k_1 and k_3 energy; I shall denote purely k_1 and purely k_3 energy monopoles as "splay" and "bend" singularities in this discussion. Numerical simulation is accomplished by straightforward integration of the equations of motion given in Section 2.1.4, and periodic calculation of observables useful in describing the behavior of the system.

4.1.1 The Equations of Motion

Eq. (2.11) is the basis for my numerical simulation of the 2D SLC. The summations can be expanded to give the following two coupled differential equations for n_x and n_y:

$$\gamma\frac{\partial n_x}{\partial t} = k_1\frac{\partial^2 n_x}{\partial x^2} + k_3\frac{\partial^2 n_x}{\partial y^2} + (k_1 - k_3)\frac{\partial^2 n_y}{\partial x \partial y} - \lambda(n_x^2 + n_y^2 - 1)n_x \qquad (4.1)$$

$$\gamma\frac{\partial n_y}{\partial t} = k_3\frac{\partial^2 n_y}{\partial x^2} + k_1\frac{\partial^2 n_y}{\partial y^2} + (k_1 - k_3)\frac{\partial^2 n_x}{\partial x \partial y} - \lambda(n_x^2 + n_y^2 - 1)n_y , \qquad (4.2)$$

which are discretized in the usual way, by replacing n_x and n_y with discrete values $x_{i,j}$ and $y_{i,j}$ on a 2D grid, gridspacing a, and by approximating the derivatives by finite differences:

$$x'_{i,j} = x_{i,j} + \frac{\Delta t}{4\gamma a^2}[4k_1(x_{i+1,j} - 2x_{i,j} + x_{i-1,j}) + 4k_3(x_{i,j+1} - 2x_{i,j} + x_{i,j-1}) \qquad (4.3)$$

$$+(k_1 - k_3)(y_{i+1,j+1} - y_{i+1,j-1} - y_{i-1,j+1} + y_{i-1,j-1}) - 4\lambda\left(x_{i,j}^2 + y_{i,j}^2 - 1\right)x_{i,j}]$$

$$y'_{i,j} = y_{i,j} + \frac{\Delta t}{4\gamma a^2}[4k_1(x_{i+1,j} - 2y_{i,j} + y_{i-1,j}) + 4k_3(y_{i,j+1} - 2y_{i,j} + y_{i,j-1}) \qquad (4.4)$$

$$+(k_1 - k_3)(x_{i+1,j+1} - x_{i+1,j-1} - x_{i-1,j+1} + x_{i-1,j-1}) - 4\lambda\left(x_{i,j}^2 + y_{i,j}^2 - 1\right)y_{i,j}] .$$

The terms on the l.h.s. are used to fill a new lattice, which replaces the old one after the entire set of new $x_{i,j}$ and $y_{i,j}$ are calculated. The diffusion constant γ, timestep Δt, lattice constant a, elasticity constants k_1, k_3, and λ are the free parameters at this stage. Following a single evolutionary step, Langevin noise is applied to the spins in the lattice, by calculating the angle of each spin $\theta = \tan^{-1}(n_y/n_x)$ and adding to it a random value $\delta\theta = 2\pi\Gamma_{LA}\eta$. η is a gaussian random number, with $\langle\eta\rangle = 0$ and $\langle\eta^2\rangle = 1.0$. The combination of a single evolutionary step and a Langevin step is known as an iteration. After n_{iter} iterations, measurements are made on the system and recorded.

4.1.2 Operational Parameters

I typically operated the simulation with $\gamma = 1$, $k_1 = k_3 = 0.1$, a timestep of $\Delta t = 0.005$, a Langevin noise amplitude of $\Gamma_{LA} = 0.01$, a gridspacing $a = 0.1$, and a potential depth of $\lambda = 4$. Naturally, only the ratio $\Delta t/\gamma a^2$ is relevant, but I hold to the nomenclature for sentimental reasons. By varying Δt over a wide range, with the lattice grid size a and the diffusion constant γ set to unity, I found that the 2D SLC evolution algorithm presented in Eqs. 4.3-4.4 was stable over the range $\Delta t \leq 0.25$ (I recognized instability as a condition where the system did not equilibrate after protracted evolution).

I also studied the behavior of the simulation for larger Γ_{LA}; with $\Gamma_{LA} > 0.5$ or so, the system became too noisy to observe any coarsening dynamics.

For the evolution, I selected periodic boundary conditions. Periodic boundary conditions (PBC's) effectively create an infinite system, in which the single system under study is replicated and repeated on all sides, forming a large mosaic-like tile. In other words, the left side of the system is equivalent to the right, and the top to the bottom. Such a warped system can also be envisioned as being the surface of a doughnut shaped torus. PBC's are popular because they allow finite size effects to be minimized, but they create problems related to unanticipated interactions with the infinite images extending on all sides.

4.1.3 Initial Conditions

My initial condition configurations include totally random spins, random with various amounts of averaging, and splay, bend, and dipole singularity configurations.

The random configurations are generated as follows: the totally random (TR) configuration generates spins with a uniform probability distribution $p_\theta(\theta) = 1/2\pi$ for $\theta \in [0, 2\pi]$. The singly averaged random configuration (AR) is generated by convolving the n_x and n_y components of a TR configuration with the averaging matrix:

$$\mathcal{M}_{AR} = \frac{1}{16} \begin{bmatrix} 1 & 2 & 1 \\ 2 & 4 & 2 \\ 1 & 2 & 1 \end{bmatrix} . \tag{4.5}$$

Note that convolving θ with $\mathcal{M}_{AR}$ will not work, because such an averaging destroys the uniform distribution in $\theta \in [0, 2\pi]$. I have also used three other averaging matrices,

$$\mathcal{M}_{AR1} = \frac{1}{24} \begin{bmatrix} 1 & 3 & 1 \\ 3 & 8 & 3 \\ 1 & 3 & 1 \end{bmatrix} \tag{4.6}$$

$$\mathcal{M}_{AR2} = \frac{1}{32} \begin{bmatrix} 1 & 4 & 1 \\ 4 & 12 & 4 \\ 1 & 4 & 1 \end{bmatrix} \tag{4.7}$$

47

$$\mathcal{M}_{\text{AR3}} = \frac{1}{44} \begin{bmatrix} 1 & 5 & 1 \\ 5 & 20 & 5 \\ 1 & 5 & 1 \end{bmatrix}, \tag{4.8}$$

which generate configurations I will denote as AR1, AR2, and AR3, respectively. Averaging is done to produce a more realistic physical system, for which the director field is usually a locally smooth function. My experience has shown that using the TR configuration may lead to a spurious start-up transient in some observables, which may hide important features of the dynamics under study.

The splay singularity is that of a $+1$ monopole (Table 3.1), for which $\theta = \pi + \tan^{-1}(y/x)$. The bend singularity is that of a $+1$ monopole whose rods are arranged along concentric circles, for which $\theta = 3\pi/2 + \tan^{-1}(y/x)$. The dipole singularity is that of a pair of oppositely charged monopoles separated by distance d, for which $\theta_{i,j} = \tan^{-1}[y/(x+d)] - \tan^{-1}[y/(x-d)]$. Note that the core structure is ignored in all of these configurations.

4.1.4 Observations

The primary tool used to observe the 2D SLC as it evolves is the generation of "Schlieren" images, pictures of what the system would look like between crossed polarizers. Schlieren images may be generated by producing a grey-scale image with the intensity at a point in the system fixed to be $I = \sin^2(2\theta)$, where θ is defined to be the local angle of the molecule $\theta \equiv \tan^{-1}(n_y/n_x)$. As discussed in Section 3.1, such images produce high contrast, four pronged "Maltise" crosses centered at the location of the ± 1 monopoles in the system.

Another useful tool for visualization is a simple direct plot of the field, using an assembly of rods whose lengths and orientations are given by n_x and n_y. Other observables which can be calculated include the monopole density, and the two-point correlation function. Data from these calculations will be discussed later in this chapter, in Section 4.4.

Eigenstates

Bend and splay singularities ($+1$ monopoles) are solutions to the equations of motion of the 2D SLC. Thus, in my simulation, with periodic boundary conditions, it should be possible to reach a steady-state solution in which oppositely charged bend or splay singularities form a lattice to balance against each other. For example, if a $+1$ monopole is placed in the middle of the system, another

48

+1 monopole should form in the four corners (one quarter of a monopole in each corner, from the perspective shown), and two −1 monopoles formed between the left and right sides, and the top and bottom. Eventually the system should equilibrate to a state with total monopole charge of zero. These states are pictured in Figures 4-2 and 4-1.
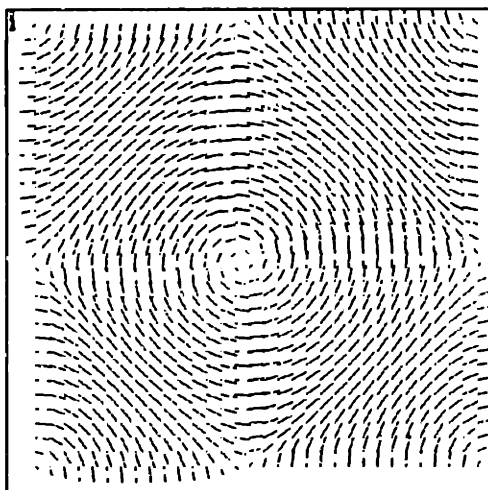
Figure 4-1: Lattice of "bend" singularities generated by evolving a single bend energy monopole in a system with periodic boundary conditions.
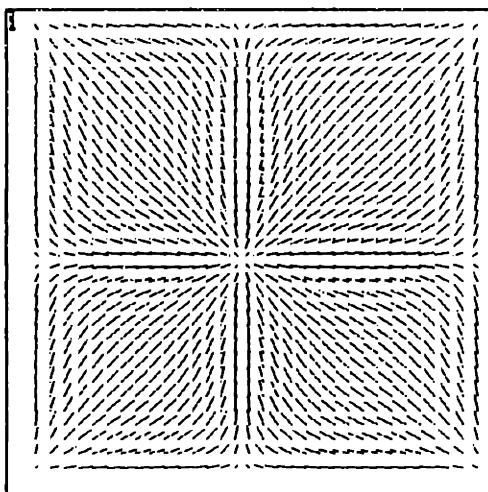
Figure 4-2: Lattice of "splay" singularities.

Two monopoles of opposite charge attracting each other are expected to approach at a rate given by $\dot{r} \propto \frac{1}{r}$. Figure A-1 shows a typical crossed-polarizer image of a monopole pair. I have measured the distance r between two monopoles as a function of time (in units of number of evolution steps), in 128×128 and 256×256 sized systems. The data from my 256×256 simulations, shown in Figure 4-3, agree well with the expected results. The simulation was run on a Cray X-MP for 24 hours, with the operating parameters as given in Table 4.1. The monopole separation was obtained by measuring the separation of the cores on a large printed Schlieren image. Figure 4-4 shows the same data plotted differently, with r^2 vs. time.
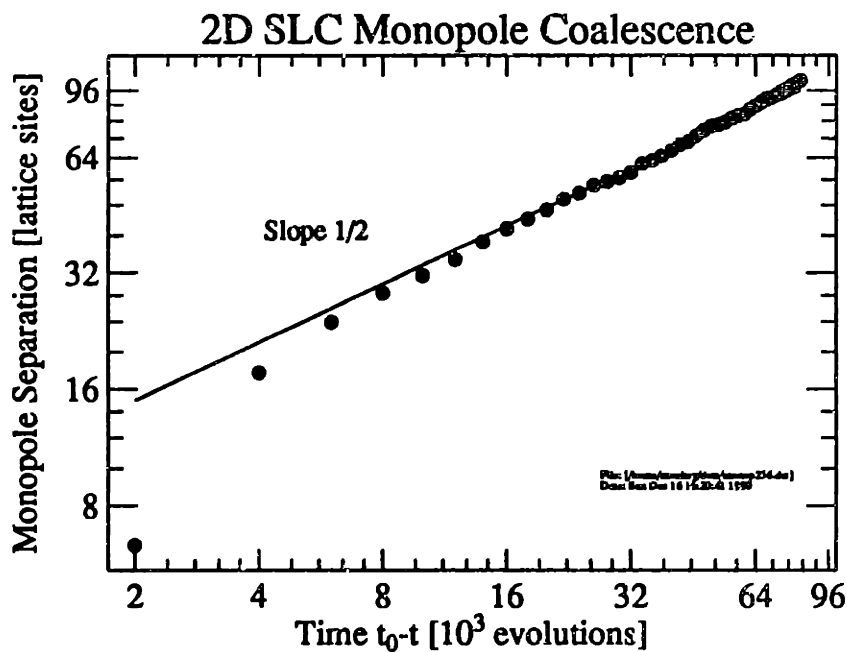
Figure 4-3: Data from a 256×256 sized numerical simulation showing the rate of monopole coalescence in the 2D SLC. Monopole separation is measured in units of lattice spacings, and time is measured in thousands of evolutionary steps. The results are in agreement with theoretical expectations predicting that $\dot{r} = 1/r$. t_0 is the time at which the two monopoles have annihilated with each other.

2D SLC Monopole Coalescence

$r^2 = 1.00 - 0.0127t$
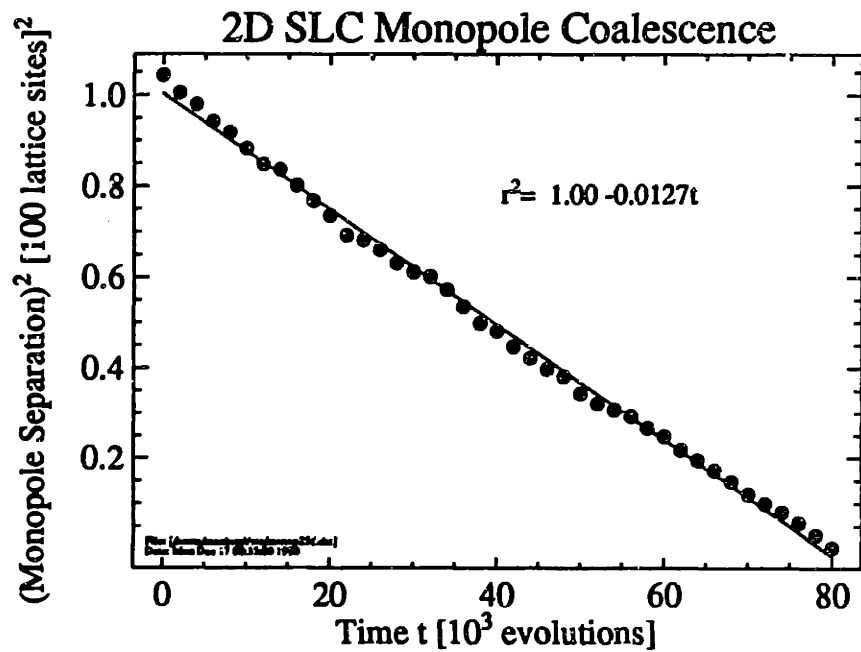
Figure 4-4: Same data as in Figure 4-3 plotted differently, with r^2 vs $t_0 - t$. This plot shows that the expected $r^2 \propto (t_0 - t)$ behavior is seen even for small $t_0 - t$.

Thermal quench

Evolution from an initial configuration of randomly oriented spins can be considered to be equivalent to the evolution of a system immediately after it has undergone a transition from a state of lower to higher symmetry. It is in fact, the evolution of the 2D SLC as it undergoes a symmetry breaking phase transition from O(2) to $\mathcal{Z}_1$. Initially, the system reacts strongly to the disorder in the rod orientations, and spontaneously forms a plethora of monopoles. During the next stage, the monopoles coalesce, reducing the density of defects in the system. The final state leaves the director field uniformly oriented in one random direction. Such a sequence of events is shown in Figure A-2.

4.2 The 2D Nematic

Analysis of the 2D NLC is the next natural step towards the ultimate goal of simulating the behavior of the 3D NLC. The 2D NLC differs from the 2D SLC only in the addition of a rod inversion symmetry: $-\vec{n} \leftrightarrow \vec{n}$. Unfortunately, however, such an identification is difficult to implement in a straightforward fashion when a vector field is used as the director field. Possible approaches include (1) exploiting the computer's ability to mechanically calculate all possible $\pm \vec{n}$ combinations, and (2) the use of an analytic solution, in which $\vec{n}$ is replaced with SO(3) tensors N_{ik} which contain the desired inversion degeneracy. I discuss these two approaches and my results below.

4.2.1 The Vector Model 2D NLC Equations of Motion

The identification between $\vec{n}$ and $-\vec{n}$ which gives the added symmetry distinguishing the 2D NLC from the 2D SLC can be implemented by evolving a system whose field components are n_x and n_y, as in the 2D SLC case, but additionally inserting a procedure in the evolution step by which all possible combinations of the local $x_{i\pm n_i, j\pm n_j}$ and $y_{i\pm n_i, j\pm n_j}$ are enumerated and the least energy set are chosen to calculate the new $x_{i,j}$ and $y_{i,j}$. The two possible orientations of a certain spin at i, j are given by $(x_{i,j}, y_{i,j})$ and $(-x_{i,j}, -y_{i,j})$. Unfortunately however, the energy density $\mathcal{E}_{2D}$, Eq. (2.8), contains only first derivatives of n_x and n_y, and thus cannot be discretized symmetrically.

My goal in this procedure would be to calculate the optimal sign for n_x and n_y at the five sites, $i \pm 1, j, i, j \pm 1$, and i, j used in integrating Eqs. 4.3 and 4.4. I do this by calculating the local energy density centered at each of the sites, in such a way that the total energy density $\mathcal{E} = \mathcal{E}_1 + \mathcal{E}_2$ is

minimal, where $\mathcal{E}_1 = \sum(\partial_1 n_2 + \partial_2 n_2)^2$ and $\mathcal{E}_2 = \sum(\partial_1 n_2 - \partial_2 n_1)^2$ are the splay and bend energies, respectively. With reference to the cell locations defined in Figure 4-5, $\mathcal{E}_{k1}$ and $\mathcal{E}_{k3}$ are calculated as follows:

$$\frac{\mathcal{E}_{k1}}{k_1} = (x_8 - x_6 + y_{11} - y_3)^2 + (x_7 - x_5 + y_{10} - y_2)^2 \qquad (4.9)$$

$$+ (x_4 - x_2 + y_7 - y_1)^2 + (x_9 - x_7 + y_{12} - y_4)^2 + (x_{12} - x_{10} + y_{13} - y_7)^2$$

$$\frac{\mathcal{E}_{k3}}{k_3} = (x_3 - x_{11} + y_8 - y_6)^2 + (x_2 - x_{10} + y_7 - y_5)^2 \qquad (4.10)$$

$$+ (x_1 - x_7 + y_4 - y_2)^2 + (x_4 - x_{12} + y_9 - y_7)^2 + (x_7 - x_{13} + y_{12} - y_{10})^2 .$$
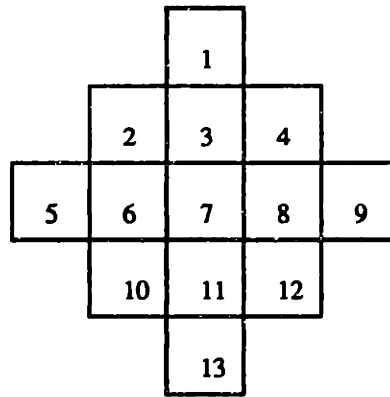
Figure 4-5: Sites used in energy density calculation.

Though only the five sites shown in Figure 4-6 are needed, the eight surrounding sites are also required to determine what the minimal energy signs are. The total of 2^{13} possible combinations are prohibitive, if I presume to calculate $\mathcal{E}$ for all of possibilities. A possible simplification of this scheme is to select N of the possibilities, and to choose the minimal energy configuration from that set. Mechanically, that is done by rolling a $\log_2 N$ sided dice, and using the individual bits of the random number to determine which subset of the 13 cells gets their signs flipped. However, I found that even with a large N, this method was sub-optimal. At worst, one evolution step would take N times longer than a 2D SLC evolution step, and N needed to be on the order of 10^3 or 10^4 before the procedure started being effective in imposing the desired inversion symmetry. This was discouraging.

```
        ┌──────┐
        │      │
        │ i,j+1│
        │      │
 ┌──────┼──────┼──────┐
 │      │      │      │
 │ i-1,j│  i,j │ i+1,j│
 │      │      │      │
 └──────┼──────┼──────┘
        │      │
        │ i,j-1│
        │      │
        └──────┘
```
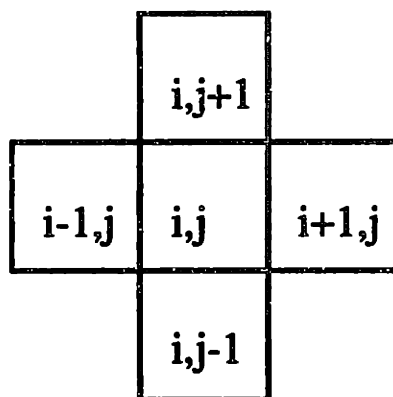
Figure 4-6: Sites used in integrating equations of motion.

4.2.2 The Tensor Model 2D NLC Equations of Motion

Because of the number problems I encountered implementing vector field equations of motion for the 2D NLC, I turned instead to applying the SO(2) tensor model for the director field evolution which was introduced in Section 2.1.5. Though this method increased the number of field components from two to three, and introduced a degeneracy in the mapping into physical space, all of the troubles described in the previous subsection were avoided.

The equations of motion (allowing for unequal k_i) governing the evolution of the $N_{ab}(i,j)$ at the sites i,j are given in Figure 2-3. I mechanically enumerated all the summation indices and discretized the derivatives as before, then ran the resulting mess through Macsyma[1] to reach a final set of simplified explicit equations of motion for each of the N_{ab}. This procedure worked, but evolution was disappointingly slow, primarily because of the sheer complexity of the equations.

My next try was to simplify the equations of motion to the equal constant case, Eq. (2.25). At last, the simulation worked reasonably rapidly (at about one-quarter the speed of the 2D SLC), and allowed me to successfully produce Schlieren images showing chains of $\pm\frac{1}{2}$ monopoles.

4.2.3 Observations

The set of initial configurations I used were the same as for the 2D SLC. Shown in Figure 4-7 is the director field of a single $+\frac{1}{2}$ monopole sitting in the center of the system. PBC's have forced the system to create a $-\frac{1}{2}$ monopole sitting at the middle of the right hand side wall. Figure A-3

---

[1] A symbolic math package originally developed at MIT through Project MAC at the Laboratory for Computer Science.

shows three pairs of $\pm\frac{1}{2}$ monopoles coalescing in the late stages of evolution of a 2D NLC, and Figures A-4 and A-5 show the director field configuration and corresponding Schlieren image of a system evolved from an initial random configuration.
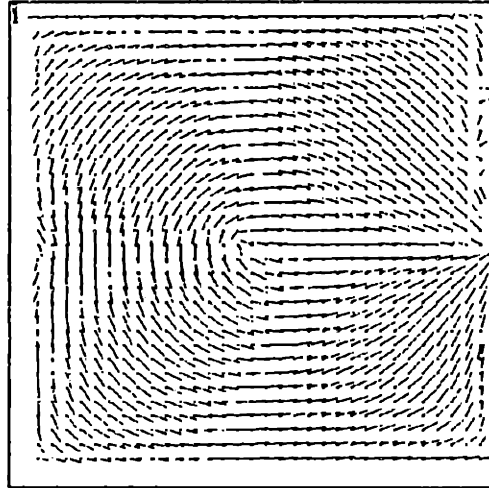
Figure 4-7: Director field of a $+\frac{1}{2}$ monopole in the 2D NLC.

The first, and most striking observation was that ±1 monopoles, though they could be created in the system, slowly decomposed into pairs of $\pm\frac{1}{2}$ monopoles which would annihilate with their counterparts separating from the image ±1 monopole formed by the periodic boundary conditions. I interpret this observation as an indication that the energy of a ±1 monopole is greater than that of two $\pm\frac{1}{2}$ monopoles in the 2D NLC, at least in the equal constant approximation.

4.3 The 3D Nematic

The 3D NLC is the most complicated of all the numerical simulations I devised. Not only is the evolution of the system more difficult and time-consuming to calculate, but also, defects in the system are much harder to visualize. I studied $x \times y \times z$ systems, with $x, y, z = 8, 16, 32$ and 64. I also used a variety of initial conditions which allowed a rich set of interaction possibilities to be explored, including string and loop formation, texture collapse, and ±1 string escape.

4.3.1 The 3D NLC Equations of Motion

Following my experience with the 2D NLC, I first tried integration of the full equations of motion for the 3D NLC, but then gave that up in favor of using the equal-constant approximation, Eq. (2.28). I mechanically enforced the symmetry of the 3×3 N_{ij} matrices (my representation of SO(3) tensors), and as before, enumerated the summation indices and simplified the expressions using Macsyma. Furthermore, I implemented fixed boundary conditions, as well as periodic boundary conditions (PBC's). In my fixed boundary conditions, the director on the boundary can be fixed to be parallel or perpendicular to the boundary.

Note that in contrast to the 2D SLC calculation, but similar to the 2D NLC, no Langevin noise was applied.

4.3.2 Initial Conditions

I observed the evolution of eight different initial configurations. These are listed below:

- **Random** – Unit length spins which are distributed evenly in orientation space (over 4π steradians).

- **Texture** – $\pi_3(\mathcal{M}_0)$ defect, with the director field as given in Eq. (3.6), and $\chi = 2\pi r/s$, with s being the scale, or the size, of the texture.

- **Deformed texture** – $\pi_3(\mathcal{M}_0)$ defect, with $\chi = \pi(1 + \tanh(\frac{r-s(1+d*\cos\phi)/2}{w}))$, where ϕ is the normal azimuthal angle, s is the scale, d is the deformation parameter, and w is the width of the texture.

- **+1 string** – An escaped +1 string, axis along the $\hat{z}$ axis, with the director field given by $\vec{n} = \hat{x}\cos\phi + \hat{y}\sin\phi + 10(\tanh(-r/3) + 1)\hat{z}$, $r = \sqrt{x^2 + y^2}$.

- **+$\frac{1}{2}$ splay string loop** – Infinite +$\frac{1}{2}$ string used as a cross section of revolution to produce a loop (with a monopole in the middle). $\vec{n} = \hat{x}\cos(\phi/2) - \hat{y}\sin\phi\sin(\phi/2) + \hat{z}\cos\phi\sin(\phi/2)$.

- **Pair of $\pm\frac{1}{2}$ splay strings** – Two infinite (by PBC's) splay energy strings, axes in $\hat{z}$ direction, parallel to each other, separated by distance $2d$. $\vec{n} = \hat{x}\cos(\phi_1 - \phi_2 + \pi/2) + \hat{y}\sin(\phi 1 - \phi 2 + \pi/2)$, $\phi_1 = \tan^{-1}(y/(x - d))$, $\phi_2 = \tan^{-1}(y/(x + d))$.

- **Pair of $\pm\frac{1}{2}$ twist strings** – Two infinite (by PBC's) twist energy strings, axes in $\hat{z}$ direction, parallel to each other, separated by distance $2d$. $\vec{n} = \hat{x}\cos(\phi_1 - \phi_2 + \pi/2) + \hat{z}\sin(\phi 1 - \phi 2 + \pi/2)$, $\phi_1 = \tan^{-1}(y/(x - d))$, $\phi_2 = \tan^{-1}(y/(x + d))$.

- **Converging $\pm\frac{1}{2}$ string pair** – Two infinite (by PBC's) twist energy strings, axes in $\hat{y}$ direction, gradually coming together at a point. $\vec{n} = \hat{x}\cos(\phi_1 - \phi_2 + \pi/2) + \hat{z}\sin(\phi 1 - \phi 2 + \pi/2)$,

$\phi_1 = \tan^{-1}(y/(x - d))$, $\phi_2 = \tan^{-1}(y/(x + d(r)))$, $d(r) = \sqrt{d_0^2 - y^2}$ (for $y > d_0$, $\vec{n} = \hat{z}$), where d_0 is half the maximum string-string separation.

4.3.3 Observations

I observed many interesting defects in formation, and several decay processes. My three main tools were direct observation of cartesian planes of the director field (rod pictures), cartesian planes of the energy density, and volumetric surfaces of constant energy. The general procedure was to write the initialization code, and set up the program to run for several hours (or days, in several cases), periodically storing the entire configuration state on disk for later analysis and to allow restart in case of premature termination (like the cray system manager killing my 5 Megaword process...).

Separate analysis programs were written to allow interactive visualization of the rod orientations, and rendering of the energy density into shaded volumetric surfaces. I used NCSA XDataSlice and XImage extensively. My discussion below begins with a survey of defects produced from a random initial configuration, and continues on to observations of ± 1 and $\pm \frac{1}{2}$ strings. Finally, I describe the behavior of balanced and deformed texture in this simulation.

Defects from a random initialization

I ran several long simulations beginning with an initial configuration of random spins, generated as described in the previous subsection. The two largest runs of size $64 \times 64 \times 32$ with PBC's were performed, one on a Cray X-MP for three days, and another on a Sun Sparcstation 1 for two weeks. Analysis of the data was accomplished by processing the saved configurations with a program which calculated the local energy density $\mathcal{E}$ at each lattice site, normalized the values, and generated a 3D-SDS (Scientific Data Set) input file for use in NCSA XDataSlice.

Figure A-7 shows a picture of the final result of the cray simulation. Plotted are constant-energy surfaces, viewed from different angles. Note the existence of several closed loops. I believe that all of these defects are $\pm \frac{1}{2}$ strings, because of the ability of ± 1 strings to escape – to become very diffuse in energy. I expect ± 1 strings to be very difficult to see using my rendering technique, because the constant-energy surfaces would be very large. The $\pm \frac{1}{2}$ strings, on the other hand, are easily located by their sharp singularities in energy density. Furthermore, the size of simulated system may be too small to favor creation of ± 1 strings, as discussed in Section 3.5.

The final state of the evolution of a smaller, 32×32×16 system, is shown in Figure A-8. Here, two $\pm\frac{1}{2}$ loops remain, one which has already collapsed to the point that it looks like a blob on this visualization scale. I do not believe it to be a monopole. In fact, I have not seen any monopoles created from my random start simulations. Monopoles should appear as very, very obvious, concentrated point-singularities in the energy field, and would be attached to two ± 1 strings. I have also checked (in vain) for the existence of monopoles by studying the rod pictures directly, in search of a hedgehog like configuration. Creation of monopoles may be inhibited by the same mechanism which suppresses creation of ± 1 strings in my relatively small systems.

± 1 strings

I attempted to create an infinite $+1$ splay energy string in two ways. First, I tried a director field with no z component, just layers of 2D splay singularities: $\vec{n} = \hat{x}\cos\phi + \hat{y}\sin\phi$, for an azimuthal angle ϕ, and with the same $\vec{n}$ for all z. The evolution parameters were $\Delta t = 0.1$, $\lambda_A = \lambda_B = \gamma = a = 1$, and $k = 0.1$, and the system was 32×32×16 in size. I hoped that the periodic boundary conditions in $\hat{z}$ would create an essentially infinite length string, and that the PBC's in $\hat{x}$ and $\hat{y}$ would arrange to create an oppositely charged string, to leave a system with a total monopole charge of zero. However, this configuration quickly decayed into two $\pm\frac{1}{2}$ string loops, as shown in Figure A-9. Study of the rod pictures of these loops, Figure A-10, revealed that the two opposite segments of the rectangular loop were of opposite charge, and adjoining segments were of differing energy type (splay-bend or twist).

My second attempt to create a stable infinite $+1$ string succeeded, but with an unpredicted side effect. I used the escaped $+1$ string initial state configuration described in Section 4.3.2, and evolved the system for 24,000 steps, at which point it had equilibrated into a state with a stable infinite $+1$ string, with a companion compound -1 object formed of two infinite $-\frac{1}{2}$ strings. A rod-picture of this configuration is shown in Figure 4-8.

$\pm\frac{1}{2}$ strings

I also experimented with creating $\pm\frac{1}{2}$ strings, as pairs of infinite strings, and as loops. The $+\frac{1}{2}$ splay string loop I created (see section 4.3.2) collapsed immediately. I did not think of a way to create a stable loop in a system with PBC's. However, the $\pm\frac{1}{2}$ splay string pair configuration did stabilize,
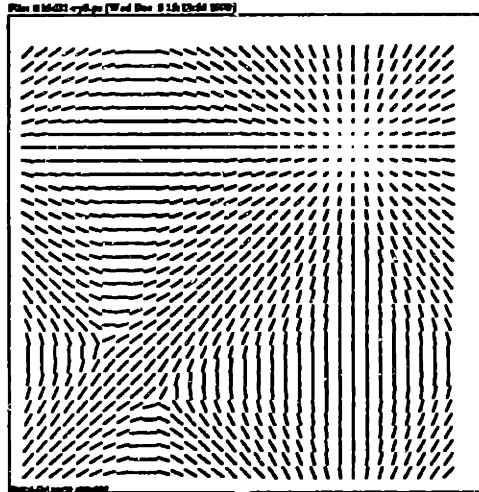
Figure 4-8: $x - y$ cross section of a $32\times32\times16$ system with a stable, escaped $+1$ string (upper right corner) and a bound state of two $-\frac{1}{2}$ strings (lower left corner).

as expected. A rod picture of the cross section is shown in Figure 4-9.

Texture

I performed several simulations to observe the decay of texture in my 3D NLC system, but did not study it systematically enough to draw any conclusions. Figure A-11 shows the cross section of an undeformed texture as it collapses. I also studied the decay behavior of a deformed texture, in a $64\times64\times64$ sized system, with scale $s = 32$, deformation $d = 0.5$, width $w = 5$, and fixed, parallel BC's on all sides. However, I placed the texture too far to one side of the box; as a result, the outer $+1$ string developed two "holes" where the rods glued themselves to the walls, and the entire defect rapidly decayed through interactions with the boundary.

Turok has developed a different numerical simulation program in which he treats the equations of motion as a diffusion equation, and calculates the new spin from an average of the old, neighboring spins. He has extended his simulation to allow for the inversion symmetry of the nematic, by calculating all the possible rod configurations and choosing the minimal energy set, similar to what was attempted in this work; however, his algorithm succeeded, because he had fewer degrees of freedom to deal with. Turok has simulated the behavior of texture in the 3D NLC extensively,
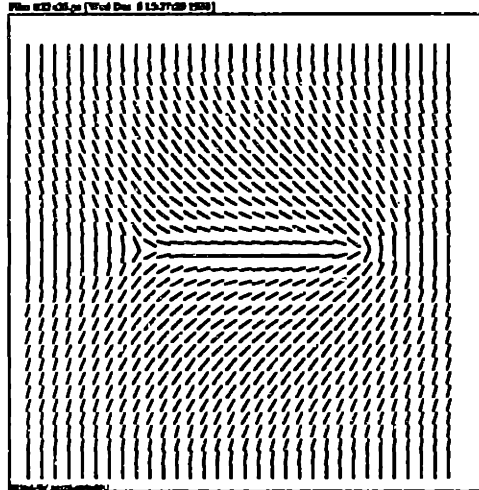
Figure 4-9: Cross section of stable configuration of two infinite $\pm \frac{1}{2}$ strings.

though mostly in the approximation in which the NLC's rod inversion symmetry is neglected [2]. His results indicate that though the undeformed texture collapses as might be expected, deformed textures decay prematurely, through a dynamical instability in which the two ± 1 strings pinch off and form two monopoles. These predictions are in good qualitative agreement with our experimental observations (in an actual thin film of NLC), as will be discussed in Section 5.4.

4.4 2D SLC Evolution Dynamics

Scaling exponents are important in characterizing the dynamics of topological defects in liquid crystals as they interact after being created in an symmetry breaking phase transition. Exponents for various processes may be calculated by measuring the rate of change of their observables in a simulation, beginning from a random initial configuration. I have measured two observables in the 2D SLC system: the structure function, and the monopole density.

---

[2] For texture simulations, inclusion of the rod inversion symmetry should not be necessary, because the only singularities in the system are ± 1 strings.

4.4.1 Scaling of the Structure Function

Theory

The two-point correlation function of the director field is given by:

$$C(\vec{r}) = \frac{1}{N^2} \sum_{\vec{r}_i} n_a(\vec{r}) n_a(\vec{r} - \vec{r}_i) , \tag{4.11}$$

where n_a are the components of the director field for the 2D SLC. Typically, because only the scaling of C with respect to the distance $r = |\vec{r}|$ is interesting, an integration over θ is done:

$$C(r) = \int r \, d\theta \, C(\vec{r}) . \tag{4.12}$$

In theories dealing with spinodal decomposition, the position of the first minima in $C(r)$ indicates the characteristic length scale of the domain walls[GMS83]. However, in the 2D SLC, whether there should be a distinct peak or not is unclear; instead, I would expect the correlation function to begin at 0.5 near $r = 0$, and decrease monotonically to some floor level.

The structure function $\tilde{C}(k)$ is defined as the Fourier transform of $C(r)$. Quantities which are often used to characterize the structure function are the ith moments k_i, defined as:

$$k_i = \frac{\sum_k k^i \tilde{C}(k)}{\sum_k \tilde{C}(k)} . \tag{4.13}$$

Analogous moments r_i for $C(r)$ may also be calculated. In the 2D SLC, it may be expected that r_1 should reflect the characteristic length scale, so that in the scaling regime, $r_1(a_{r1}(t))$, where $a_{r1}(t)$ is the scaling function, should be a constant of time. The scaling ansatz for r_1 is

$$a_{r1}(t) \propto t^a , \tag{4.14}$$

using the notation common in the literature.

Another measure which is frequently used to calculate scaling exponents for scaling laws is k_m, which is the location of the first maxima of $\tilde{C}(k)$. In the case where $\tilde{C}(k)$ (or $C(r)$) doesn't have a peak, the points r_{l_i} for which $C(r_{l_i}) = l_i$ is a constant of time could be watched instead. If the general shape of $C(r)$ doesn't change significantly with time, this measure should be valid (no proof

given), and scale as

$$a_{l_i}(t) \propto t^{a'} . \tag{4.15}$$

Note that a will not necessarily be equal to a'.
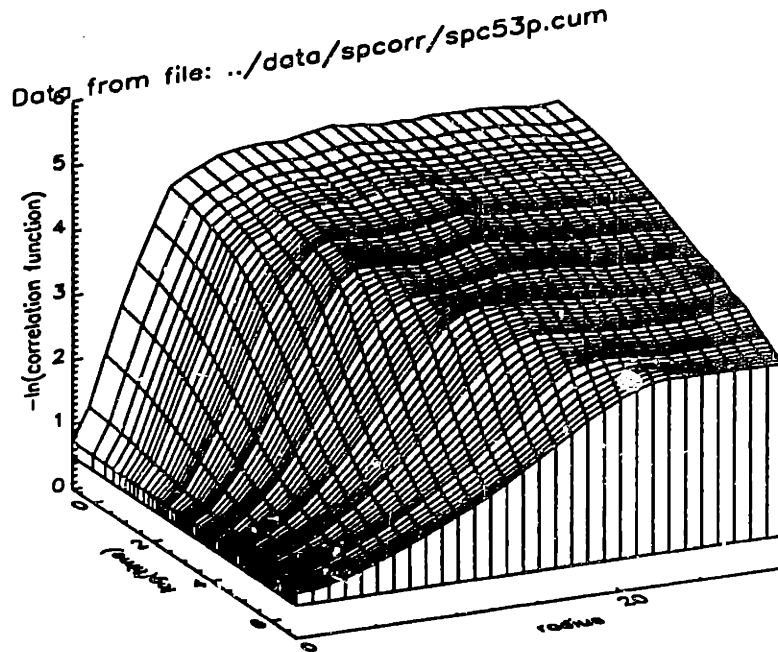
Figure 4-10: Plot of two-point correlation function vs. radius and time.

Experiment

The correlation function of Eq. (4.11) is most easily calculated using three 2D Fourier transforms:

$$C(\vec{r}) = \mathcal{F}^{-1} \left(\frac{[\mathcal{F}(n_x(\vec{r}))]^2 + [\mathcal{F}(n_y(\vec{r}))]^2}{2} \right) , \tag{4.16}$$

where $\mathcal{F}$ is the Fourier transform operator

$$\tilde{g}(k) = \mathcal{F}(g(r)) = \frac{1}{2\pi} \int g(r) e^{-i\vec{k}\cdot\vec{r}} dr , \tag{4.17}$$

and $\mathcal{F}^{-1}$ is the inverse Fourier transform operator, defined as usual. Both operations are implemented using the Danielson-Lanczos FFT algorithm[PFTV86]. The integration over θ is done by simply binning

points into groups with integer radii r_i, $0 \le r_i < r_{max}$ and averaging:

$$C(r_i) = \frac{1}{N_{r_i}} \sum_{\lfloor \vec{r} \rfloor = r_i} C(\vec{r}),$$ (4.18)

where N_{r_i} is the number of sites in the lattice at position $\lfloor \vec{r} \rfloor = r_i$. The error in $C(r_i)$ are calculated by finding the standard deviation in the distribution of the $C(\vec{r})$ which are summed:

$$\sigma_C(r_i) = \sqrt{\frac{1}{N_{r_i}} \sum_{\lfloor \vec{r} \rfloor = r_i} C^2(\vec{r}) - \left(\frac{1}{N_{r_i}} \sum_{\lfloor \vec{r} \rfloor = r_i} C(\vec{r})\right)^2}.$$ (4.19)

$C(r_i)$, and the errors $\sigma_C(r_i)$ are calculated and recorded during the evolution of a system, at exponentially increasing time intervals.

Data from file: ../data/spcorr/spc53p.xdr
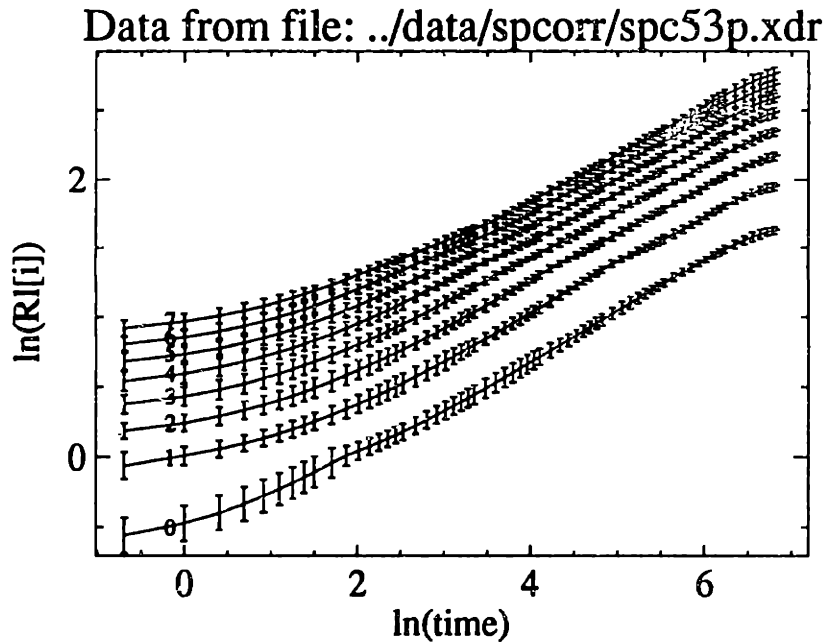
Figure 4-11: Plot of $\ln r_{l_i}$ vs $\ln t$.

The data is analyzed by first studying a contour plot of $\ln C(r, \ln t)$. If the scaling ansatz of Eq. (4.15) holds, then there should be lines of constant slope in the contour plot. The analysis is further refined by using the three points $(C(r_k), r_k)$, $k \in [1, 3]$, in the neighborhood of $C(r_{l_i}) = l_i$ to

interpolate, using a parabola, a set of r_{l_i} for various levels l_i. Errors are propagated by numerically determining $dr_{l_i}/dC(r_k)$ and propagating $\sigma_C(r_k)$. Subsequently, $\ln r_{l_i}$ vs. $\ln t$ is examined to determine the range of t where it is linear, and then best-fit to determine the slope a_{l_i}. Finally, a is determined by averaging over l_i, for a set of a_{l_i} which have been calculated from an averaged set of $C(r_i)$. Similarly, a' is found by calculating r_1 using Eq. (4.13) for $C(r_i)$, and fitting $\ln r_1$ to $\ln t$ in the scaling regime.

Data from file: ../data/spcorr/spc53p.xdr
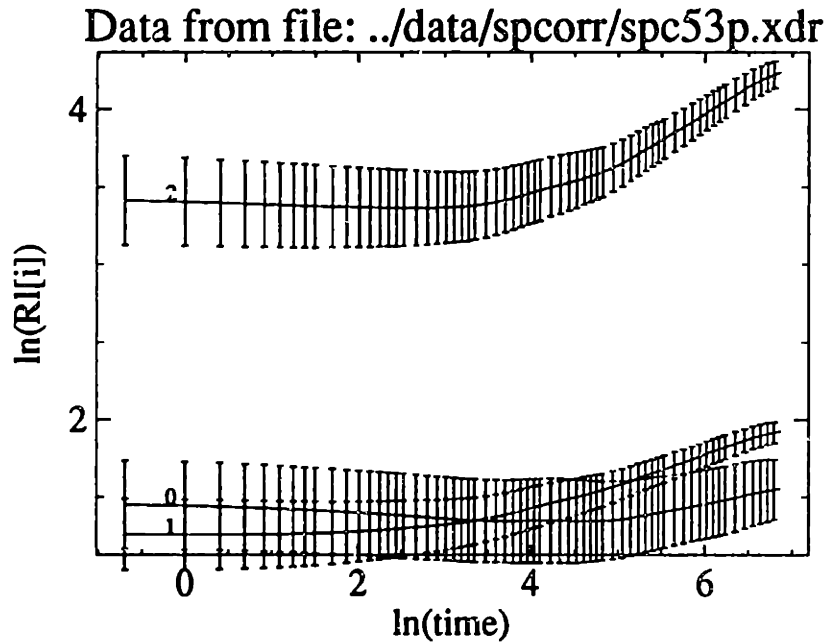
Figure 4-12: Plot of first and second moments of the two-point correlation function (see text for an explanation of the labels).

Data

Figure 4-10 shows a plot of $-\ln C(r,t)$ vs. $\ln t$ and radius r, for dataset spc56p, which is the statistical average of six datasets taken on a 128^2 lattice, beginning with a AR initial configuration. r is cut off at $r = 30$ in the plot, although it continues out to $r = 91$, because there are no interesting features in the extended range. No peaks or troughs are evident in the correlation function. I found that using progressively less averaging resulted in smaller values of $\ln C$ at early times. With no averaging, the curve increased sharply at early times, before leveling off around $\ln t \approx 3$; the AR1

and AR2 configurations resulted in longer straight-line behavior in the data. A contour plot of the $\ln C(r, t)$ surface shows sets of nearly parallel lines emanating from time $t = 0$, which are straight at first, but begin curving over around $t \approx 400$. These features are clearly indicated in Figure 4-11, which is a plot of $\ln r_{l_i}$ vs $\ln t$, for $l_i = \exp(-1 + 0.2i)$ (the numbers on the lines give i). Evidently, the scaling regime occurs approximately between $\ln t = 2$ and $\ln t = 5.5$, if the relationship in Eq. (4.15) is to be believed. Best fits to this data give $a' = 0.342 \pm 0.002$. The scaling behavior of this data is most clearly shown by actually applying the scaling relationship of Eq. (4.15) to time slices from $3 < \ln t < 6$ (the most likely selection for a "scaling regime"); the results, shown in Figure 4-13, clearly support my results for a'.
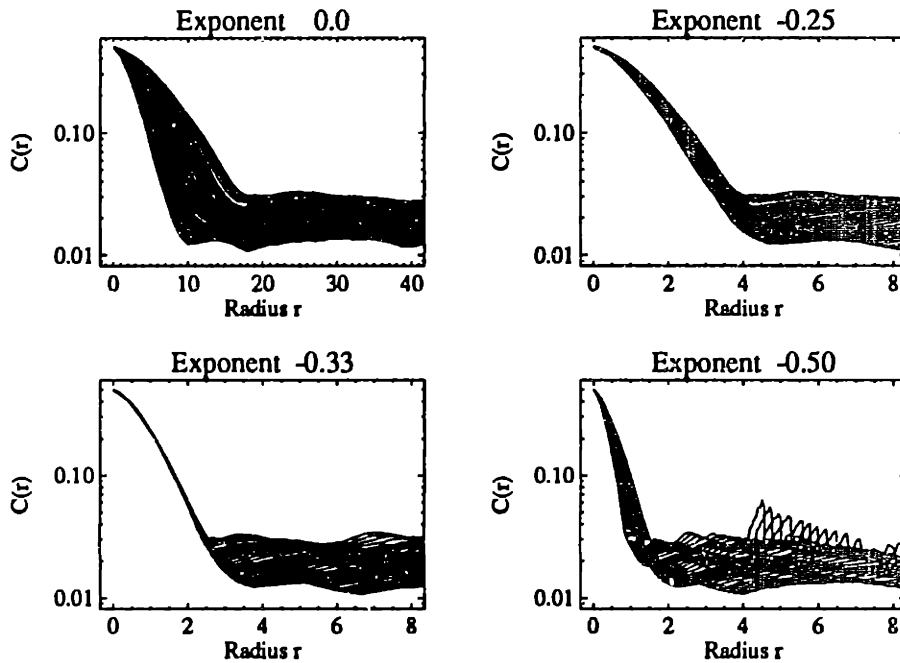
Figure 4-13: Four pictures showing the application of different exponents in renormalizing numerical measurements of the scaling function for a 2D SLC system. An exponent of $a' \approx 0.33$ appears to be correct for the $3 < \ln t < 6$ data plotted.

Unfortunately, however, the data on r_1, the first moment of $C(r)$, are not so good. The three lines in figure 4-12 correspond to $0 \to \ln \sqrt{r_2 - (r_1)^2}$, $1 \to \ln r_1$, and $2 \to \ln r_2$. They are plotted vs. $\ln t$. If $\ln t > 3$ is taken to be the linear region for r_1 and r_2, then the exponents are about 0.13 and 0.17, respectively. Not only is the scaling regime apparently different from that found for the r_{l_i}

data, but also, the exponents differ. Data gathered from 256^2 sized systems are almost identical to these 128^2 data.

Clearly, more work remains to be done to resolve these problems, and to come to a better theoretical understanding of the scaling relationships.

4.4.2 Scaling of the 2D SLC Monopole Density

Theory

Mean field studies of the coalescence of pointlike topological defects in the time-dependent Ginzburg-Landau model indicate that the density of monopoles ρ in a two-dimensional system should decrease with time as $\rho \propto t^{-2/(\beta+1)}$, where β is the exponent indicating the separation dependence of the force between defects[Toy90, Ost81]. For the 2D NLC, $\beta = 1$. A simpler dimensional argument with the same result goes as follows: the energy in a volume containing two monopoles is $\mathcal{E} \propto \ln(r)$ (see the discussion on defect energetics, Section 3.5). Thus, the rate of coalescence of a monopole pair can be calculated as:

$$\frac{dr}{dt} = -\frac{\partial \mathcal{E}}{\partial r} \propto -\frac{1}{r}.$$

(4.20)

Straightforward integration of this equation relates the separation with the time:

$$r \propto \sqrt{t_0 - t}.$$

(4.21)

If the distance r is taken to be the characteristic length scale ξ, and if it is assumed that one monopole exists per area ξ^2, and then an immediate relationship can be written down between ρ and t:

$$\rho = \frac{1}{\xi^2} \approx t^{-1}.$$

(4.22)

Experiment

The central problem in the numerical experiment is the determination of the number of monopoles in a given system. This can be done by looking for points in the lattice at which the lambda energy is above some value $E_{\lambda c}$, grouping together points which are within some distance r_{crit} of each other, then counting the final number of groups found. Such a procedure is certainly feasible; shown in Figure A-6 is a grey scale intensity image of E_λ in which monopole cores are clearly visible.

66

However, this algorithm is susceptible to undercounting when the ρ is large, because it is hard to distinguish two monopoles which are close together. Furthermore, because the algorithm also relies on selecting group members by thresholding, ρ is indeterminate until the system equilibrates to the point where distinct monopoles have formed.

Otherwise, the procedure is straightforward. A initial system with averaged random spin orientations is allowed to evolve until $\langle d\rho/dt \rangle$ is small. During the evolution, $\rho(t)$ is measured at exponentially increasing time intervals. The data is analyzed by plotting $\rho(t)$ vs. t on a log-log scale to determine the scaling exponent.
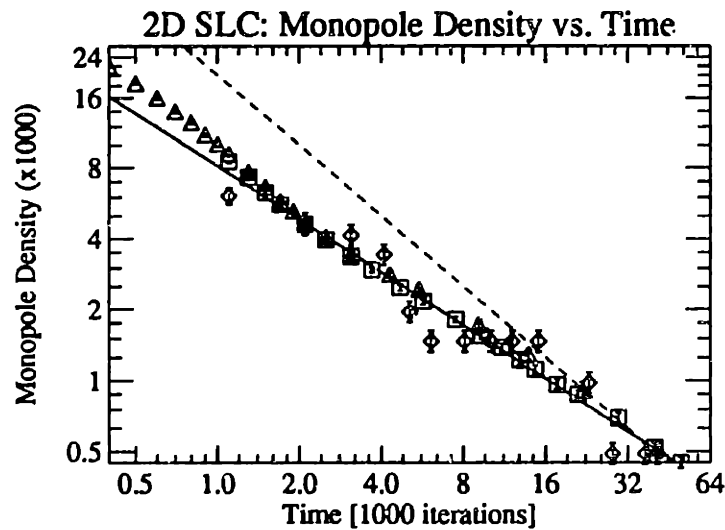
Figure 4-14: Log-log plot of three sets of data showing the scaling behavior of the monopole density in the 2D SLC simulation. Data from the 64×64 sized systems are plotted as diamonds, 128×128 as triangles, and 256×256 as boxes. The straight line through the data has slope −0.75, and the dashed line has slope −1. The expected slope, from a mean field calculation, is −1.

Data

Figure 4-14 shows a plot of the monopole density ρ vs. time. The data indicate that the best exponent is closer to 0.75 than to one. Specifically, the best-fit exponents for the 64×64, 128×128, and 256×256 sized system runs are 0.72, 0.78, and 0.74, respectively. The operational parameters are given in Table 4.1. Although my results disagree from the naive expectations, and from those of mean field calculations, the scaling exponent of 0.75 does agree with the "early-time" results of

67

Parameter	Value
Gridsize a	0.1
potential depth λ	6
timestep size Δt	0.005
diffusion constant γ	1
Langevin noise amplitude Γ_{LA}	0.01
Elasticity constants $k_1 = k_3 = k$	0.1

Table 4.1: 2D SLC operating parameters for the four 64×64, 128×128, and 256×256 sized system simulations used in gathering monopole density and monopole pair coalescence data.

[MG90] (they also found that $r \approx t^{-0.75}$), and the results of [NN89] (they studied the dynamics of line defects in a 3D system, and found that the length of defect line decreases with time as $l(t) \approx t^{-0.75 \pm 0.05}$). Unfortunately, because of time constraints, I have not had the opportunity to analyze my results further.

4.5 Summary

The numerical simulations of the 2D SLC, 2D NLC, and 3D NLC discussed in this chapter provide a bountiful testing ground for examining simple theories of defect dynamics, and defect structure. The simplicity of the 2D SLC simulation also lends itself towards calculation of observables to measure possible scaling behavior of the system. Unfortunately, interpretation of the data is unclear, in part because of the lack of computational power to analyze the behavior of larger systems, and in part because of the lack of time to pin down all the loose ends, such as finite size effects and freezing problems.

Nevertheless, the numerical simulations are very helpful in establishing some intuition about the expected behavior of an actual system, especially by allowing direct examination of the director field, an important variable which can only be observed indirectly in actual systems. This chapter closes my discussion of the exploration of NLC topological defects in numerical simulations. I turn next to the real thing, a study of the behavior of defects in 4-cyano-4'-n-pentylbiphenal.

Chapter 5

Experimental Observations

I and B. Yurke have systematically and extensively studied the dynamics of strings, monopoles, and texture defects in one particular nematic liquid crystal, using two experimental apparatuses designed to apply pressure and temperature quenches to small, thin volumes of material. Our optical microscope observations are recorded by a high speed video camera, and later played back for visual and computer analysis. We have developed sophisticated image processing techniques for automatically quantifying the defect density, and have manually counted the monopole and loop densities as a function of time after initially being created in a symmetry breaking phase transition. Our data indicate good agreement with the relative defect densities expected from the "Kibble mechanism" of cosmological defect production, and fit the predictions of the "one-scale" model for string evolution. However, our data also show unexpected behavior in the monopole and loop density evolution. In this chapter, I will describe our equipment, techniques, and experimental results.

5.1 Experimental Techniques

We have constructed equipment for studying rapid pressure and temperature induced isotropic→nematic transitions in a nematic liquid crystal (NLC), 4-cyano-4'-n-pentylbiphenyl (commercially known as "K15", or "5CB"). Our material was obtained from BDH chemicals, and used without dilution or further purification. At atmospheric pressure, this NLC has an isotropic→nematic transition temperature at 35.3°C, and a nematic→crystalline transition at 24° C. Measurements of the splay, bend, and twist elastic constants[KM77] and the viscoelastic coefficient[WC88] for this material have been

reported in the literature. At 25°C, $K_1 \approx 1.15$, $K_2 \approx 0.6$, and $K_3 \approx 1.55$ μdynes. We measured the slope $\Delta P / \Delta T$ of the isotropic-nematic phase coexistence curve to be 2.47 MPa/K, between 0.7 and 17 MPa. This slope and the 35.3°C transition temperature determine the pressure vs. temperature line which must be crossed to force an isotropic→nematic phase transition.

Our experimental apparatuses consist of a pressure cell, used to force a rapid pressure jump induced phase transition, and a free suspension loop, used to observe the effects of a temperature quench. We have also designed and tested a third apparatus which combines features from both of our workhorses. I will discuss the design and operation of three devices in this section, as well as the image processing techniques we have developed for analyzing the string density data.

5.1.1 The Pressure Cell

The pressure cell apparatus consists of a stainless steel pressure cell with observation windows, and supporting pressurization hardware. The cell contains the liquid crystal between two 1.5 mm thick sapphire windows. The thickness of the NLC layer can be adjusted by changing the level of a threaded top plug which is sealed by an O-ring. Typically, the layer is between 150 and 300 μm thick. The viewing area has a diameter of about 3 mm. Less than 1 cc of NLC fills the cell and the tube connecting it to a diaphragm, which isolates the liquid crystal from the pressurizing fluid, water. A simple hand-turned piston (pump) is used to provide between 0.7 and 34 MPa of pressure, and a valve between the pump and the diaphragm is used to apply a sudden pressure jump. Attached to the cell are a thermocouple and heating wire, to provide temperature control; the whole cell is also encased in styrofoam insulation.

The cell is mounted on the stage of a white-light transmission observation microscope, and a high speed video camera with a 5-millisecond resolution clock is used to record data onto videotape. $t = 0$ is determined by closure of a microswitch which operates when the pressure jump valve is opened. A schematic drawing of the apparatus is shown in Figure 5-1.

Boundary conditions on the cell surfaces are established by treating the sapphire windows with the homeotropic alignment material N,N-dimethyl-N-octadecyl-3-aminopropyltrimethoxysilylchloride (otherwise known as DMOAP), using standard procedures[Kah73]. For our purposes, we consider the window surfaces as imposing fixed, perpendicular boundary conditions on the NLC (the liquid crystal molecules are assumed to be "hanging" from the interfaces). The alignment effect is evident from the

70

PRESSURE JUMP
APPERATUS

ILLUMINATION

SAMPLE
CELL

DIAPHRAGM

MICROSCOPE

VALVE
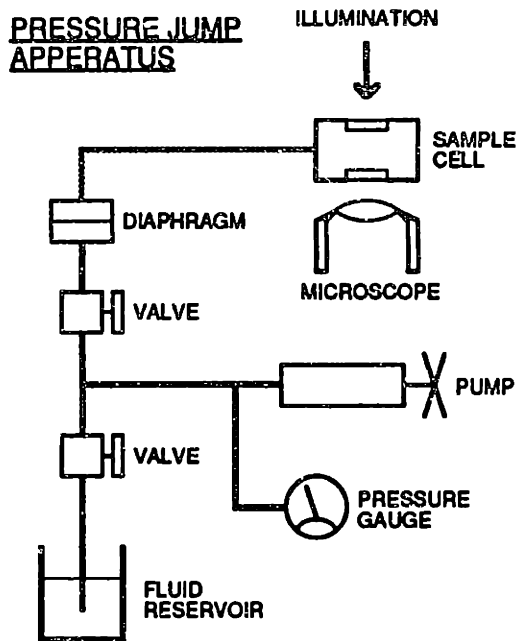
PUMP

VALVE

PRESSURE
GAUGE

FLUID
RESERVOIR

Figure 5-1: Schematic drawing of the pressure cell apparatus.

difference in appearance of the NLC between the untreated and treated cases; when the windows are untreated, the nematic takes on a "marbled" look, modulating the light with broad sweeping bands of brown even after equilibrating. When the windows have been treated, the equilibrated nematic is clear, except for the normal flickering of the director.

Typically, the cell is operated by allowing it to thermalize at a temperature around 37°C, and a pressure below that of the coexistence line. After equilibrium has been reached, the piston is brought to the desired final pressure, and the video camera is readied. Opening the pressure jump valve simultaneously starts the camera's clock and forces a phase transition in the NLC. The speed of the transition is theoretically limited by the velocity of sound in the material; we have judged that it occurs in less than 30 ms, by timing the period between when the NLC is clear (in the isotropic phase) and when string defects first become visible out of the dark mess which is seen on the camera immediately following the pressure jump. Depending on the depth of the pressure jump, and the operating temperature, the NLC coarsens to a point where few defects are visible in the camera in as little as eight seconds and as much as 60 seconds.

71

5.1.2 The Thin Freely Suspended Film

The thin, freely suspended film apparatus is substantially different in design and operation from the pressure cell. It is simply a loop of wire attached to a heating element (a 1 KΩ resistor). A droplet of NLC is carefully suspended in the loop; the precise amount is gauged to give as flat a surface as possible, to minimize lensing effects. Above the loop is mounted a dust shield with a cover glass for clear viewing, and beneath the loop are mounted two probes on xyz micrometer stages. The probes are made of single fine glass threads pulled from an approximately 1.5 mm diameter glass rod. They can be inserted into the NLC film and used to manipulate defects directly.

This entire assembly is mounted on the stage of a Zeiss microscope. The NLC film is backlit with a bright arc lamp, and is observed with 2X, 4X, and 10X objectives. In the isotropic phase, it appears as a clear, quiet fluid, while in the nematic, flickering of the rod molecules can be seen. The arc lamp lends a slight green tint to the appearance of the liquid. Defects are generated suddenly when the film is allowed to cool by convection, after heating by allowing a current to flow through the attached resistive element. About 400 mW applied for 8 seconds is sufficient to heat the NLC into the isotropic phase. Because the edges of the film cool faster than does the center (heat is conducted from the wire loop), defects usually spring forth from the sides, forming a mass of wiggling strings between the edge and an inward propagating circular domain wall dividing the nematic and isotropic phases. Often, this occurs with sufficient symmetry that a boojum (half monopole attached to the top of bottom surfaces) is created in the center of the droplet. Following the phase transition, the strings quickly intercommute with each other, coarsening into a state where most of the defects are attached to the wire loop. However, the bulk of the film will remain populated with assorted defects, including boojums, monopoles, ± 1, and $\pm\frac{1}{2}$ strings for more than half a minute before clearing. Shown in Figure A-12 is a photograph of the defect tangle produced about ten seconds after a temperature quench.

The primary utility of this apparatus is to allow manufacture of defects by direct manipulation. When a glass probe is inserted into the NLC, defects move out of its way. However, after the NLC has settled, the probe can be moved slowly and a ± 1 string will trail from it. This string will slowly escape, diffusing into a golden halo which eventually disappears, but with enough diligence and some cleverness, ± 1 strings can be led to cross each other and create monopoles. ± 1 strings can also be brought near $\pm\frac{1}{2}$ strings to observer their interactions.

72

Finally, we[1] have been able to manipulate ±1 strings to intercommute with each other in such a way as to leave behind what appeared at first to be a single, closed ±1 string. Almost immediately, a golden halo appeared around it; these golden halos are the hallmark of diffuse, very escaped ±1 strings. We observed several of these events, and believe they may be the signature of the creation of a texture defect. I will discuss this experiment in more detail in Section 5.4.

5.1.3 The Thin Film Pressure Cell

Experience with our pressure cell and thin free suspension film gave us incentive to design and construct a new apparatus which can combine the best of both. The biggest problems with the pressure cell come with window imperfections (scratches) and dust which drifts into the viewing region after repeated use. Also, the pressure cell is difficult to clean and refill, because of the volume of material it contains. However, its advantage is that pressure jumps cause much more rapid phase transitions than do thermal quenches; rapid transitions do not allow the NLC to nucleate on dust. Instead, nucleation effectively happens spontaneously, everywhere in the cell. On the other hand, the advantages of the thin film are that the top and bottom surfaces are unencumbered by tricky boundary conditions – there is only a liquid-air interface. Furthermore, thin films offer the opportunity to create very thin preparations in which essentially two-dimensional behavior may be observed.

A means to combine the best of both was proposed by Yurke. He suggested that a thin NLC film might be successfully suspended in a low vapor point liquid if a sufficiently noninteracting substance could be found. He further suggested the use of fluorinated hydrocarbons, or fluorocarbons. Such liquids are typically used as refrigerants, and have a very low vapor pressure. One such chemical is widely available commercially under the trade name "Fluorinert"[Flu]. We purchased some perfluorodecalin, and successfully trial tested this idea using a new cell. We observed a beautiful, pressure jump initiated phase transition, creating a plethora of defects. However, we have not yet been able to take data with this new cell, being too busy analyzing data from the last runs, and short of sufficient quantities of fluorocarbon to fill the pressurization system.

---

[1]Neil Turok deserves the credit for being at the micrometer controls during this sensitive operation!

5.1.4 Image Processing

A dense tangle of strings is created in a pressure jump initiated rapid isotropic→nematic phase transition. This tangle interacts with itself, by intercommuting, and forming loops which collapse. Observations of this coarsening process are recorded onto videotape, and later played back for computer analysis. The goal of this analysis, using several image processing steps, is to determine the density of strings (lines) in the picture. In this subsection, I summarize our final, best procedure, and then discuss how it was developed.

The gu..ing principle behind our application of image processing to clarify the string tangle pictures was to do as little processing as possible before estimating the string density. We used a four step analysis, including 3×3 median filtering, adaptive background subtraction, sobel gradient calculation, and a cleaning algorithm similar to morphological dilation and erosion[GW87]. Adaptive background subtraction was accomplished by dividing the 512×400 images into 128×100 sized sub-images, calculating for each region the average of each of the 32×25 sub-regions weighted by its standard deviation, fitting a 2D B-spline to the sub-image points to get 512×400 "background" images, and subtracting these from the original images. The grey levels were then rescaled such that the mean was a light grey and the standard deviation spanned the resolution of the display. This successfully normalized the light intensity across our images. Next, we calculated the Sobel gradient image. Finally, the string density was estimated from the processed images by counting the number of points above a set threshold. Examples of images generated by this procedure are shown in Fig. A-15. We chose to calibrate the string density so that it represents the number of strings per unit area crossing a plane. The calibration for each data set was obtained by counting the number of strings crossing a line drawn across the image, averaged over several lines and images, and dividing by the crossectional area, i.e., the depth of the cell times the width of the image.

We arrived at this final procedure only after considerable experimentation with various algorithms. Several problems had to be addressed. First, the images had to be normalized in light intensity and distribution. This could be accomplished several ways, such as by taking a background image, and subtracting it from the one under analysis. This did not work well, because of the wide variation in average intensity between images (dense tangle images were much darker than the final, relatively clear ones). We also tried histogram equalization, but that only brought out all the noise in the background; we desired that the background be suppressed as much as possible, and that the dark

74

lines (the strings) in the image be made sharp and highly contrasting. We also wanted the lines to be uniform in intensity and width. Because lines are large scale objects, we turned to median filtering, a procedure which takes each sub-area of an image and replaces the middle pixel by the median value in the sub-area. Median filtering is known to preserve sharp edges and blur high frequency noise. In addition to median filtering, we also devised the adaptive background subtraction method described in the previous paragraph.

The next step in the processing is to convert the image into useful information, either by locating the lines, or by directly calculating some useful quantity. From our experience with studying the structure function, we believed that a similar observable might be calculated directly from the image by taking its 2D Fourier transform, doing a radial integral, and calculating the width of the resulting distribution as a function of time after the phase transition. Unfortunately, this idea did not work, because of the noise and non-uniformity of the image, even after the first stage filtering. We found the results of the FFT to be highly dependent on the amount of filtering done the image, indicating that the noise in the image was broadband and significant.

Instead of a FFT analysis, we decided to devise a line finding algorithm. At first we devised a scheme of our own which worked fairly well. The idea was that lines could be identified locally, as humps in the intensity distribution. Humps with a certain width and depth would be validated, and others ignored. Furthermore, we could scan for humps in one dimensional strips of the image, first processing the rows then the columns. Pixels thought to be at the center of a hump would be marked, thus building up a second image which contained only those points which were elements of lines in the image. For each one-dimensional strip, we would window an eight to fifteen point segment and fit a parabola to the points to determine the height, width, and center of a hump. If these parameters fell within fixed tolerances, the central point was validated. The drawbacks of this method were that it significantly broadened the lines from their actual widths, and it sometimes failed to correctly find lines at intersections. The method also incorrectly identified isolated grey "blips" in the image as being parts of lines. Evidently, what was needed was some sort of algorithm with more than a local sense of "line."

Our next candidate for line identification was the canonical Sobel gradient operator. The Sobel operator gives two useful pieces of information: the local gradient magnitude G, and its direction θ. Typically, G and θ are used together with some thresholds to determine the existence of line

segments, and to link isolated segments together by projecting along the direction of the current segment. Additionally, before this "linking and chaining" procedure, the G and θ images can be cleaned up[CRK90] by discarding all points for which G is either less than 3σ of a threshold G_{min}, or less than 2σ of G_{min} if the point is the neighbor of an above threshold point. G_{min} and σ are calculated by dividing the Sobel image into non-overlapping 10×10 squares, calculating the standard deviation σ_i and mean $\overline{G}_i$ for each region. G_{min} and σ are chosen to be the smallest $\overline{G}_i$ and its corresponding σ_i. We use this cleaning procedure following calculation of the Sobel image G in our final procedure. We do not use a linking and chaining algorithm, because the simple implementation we wrote was time consuming and would have been prohibitively expensive in processing all forty of our final data images. One possibility for the future would be implementation of the Boie-Cox line-edge detection algorithm[BC89], which is supposed to be optimal for line recognition.

5.2   The Behavior of Strings

String defects are interesting creatures which behave very predictably, given a few simple assumptions. First, strings can be characterized as having some tension force T per unit length. Because of this internal tension, they try to unwind themselves into the straightest possible configuration, to reach a state of lowest energy. Second, strings which intersect each other while moving exchange partners; this is known as "intercommuting." Third, strings carry topological charge; like charges repel and opposite charges attract. Finally, the NLC is a dissipative system. The motion of strings in this medium competes with the damping due to viscous forces. An assembly of many strings will evolve by untangling itself, gradually becoming less and less dense. This is known as string coarsening. In this section, I will present first our observations of string intercommutation and loop collapse, then discuss our coarsening experiments. I conclude with a study of the various string intersections.

5.2.1   String Intercommutation

We frequently observe strings intercommuting with each other. Several scenarios can be imagined. Two $\pm\frac{1}{2}$ strings, bent outwards from each other, could be arranged such that they are or are not within each others arcs. If they are, then the natural straightening of the strings could pull them into each other, whereupon they would intercommute. Moreover, if they are of like charge, an intercommutation would only occur if the line tension force exceeded the repulsive force. If they

76

are not within each others arcs, then, normally, it would be expected that natural straightening would simply move them further apart; however, if they are of opposite polarity, then they will attract and thus intercommute.

The intercommutation of like-charged strings could be expected to sometimes result in the creation of a ± 1 string in-between the intercommuted $\pm \frac{1}{2}$ strings. However, such sequences are *very* rare. More often, we see sequences in which two oppositely charged $\pm \frac{1}{2}$ strings attract each other and then intercommute, as shown in Figure A-13. Furthermore, after the intercommutation, the newly formed strings appear to have no discontinuity at the junctions where the exchange took place. This is a clear indication that some mechanism is available for a $+\frac{1}{2}$ string to join continuously to a $-\frac{1}{2}$ string. I suggest that such junctions may occur through an intermediate transition from a splay-bend energy to a twist energy $\pm \frac{1}{2}$ string. In other words, for example, a $\vec{n} = \hat{x}\cos(\phi/2) + \hat{y}\sin(\phi/2)$ string in the $\hat{z}$ direction should be able to connect continuously to a $\vec{n} = \hat{x}\cos(\phi/2) - \hat{y}\sin(\phi/2)$ string by an intermediate length of $\vec{n} = \hat{x}\cos(\phi/2) \pm \hat{z}\sin(\phi/2)$ string, which is high in twist energy.

5.2.2 Loop Collapse

Loops of $\pm \frac{1}{2}$ strings often form, as a result of intercommutations leaving behind an isolated, closed length of string. These loops are unstable objects, and collapse under their own tension force. By disappearing, they have reached the lowest energy state possible. Observations of the rate of loop collapses provides a good measurement of the ratio of the string tension to the viscosity coefficient, and measurement of the evolution of the density of loops produced after a isotropic→nematic phase transition gives insight into the competing defect production mechanisms at work. I discuss these issues in this subsection, beginning with a presentation of the theory and our loop collapse data.

Theory

The dynamics of string motion are controlled by the string tension and the viscous forces. In particular, the string tension T scales as $\ln R/r_c$ where r_c is the core radius and R is the typical spacing between strings. For a string moving through the medium with a constant velocity v, it can be shown, using nematodynamic equations[dG74]:

$$\gamma \partial_t \vec{n} = -\frac{\delta \mathcal{E}}{\delta \vec{n}} , \qquad (5.1)$$

77

that the damping force Γ is also proportional to $\ln R/r_c$. $\mathcal{E}$ is the Frank free energy, given by:

$$\mathcal{E} = \frac{1}{2}\left[k_1(\vec{\nabla}\cdot\vec{n})^2 + k_2(\vec{n}\cdot\vec{\nabla}\times\vec{n})^2 + k_3\left(\vec{n}\times(\vec{\nabla}\times\vec{n})\right)^2\right].$$ (5.2)

The ratio T/Γ should thus be independent of R. We have tested this expectation by measuring the rate of collapse of $\pm\frac{1}{2}$ string loops.

The rate of collapse of loops is determined by T/Γ, the ratio of the string tension to the coefficient of viscosity. This can be understood by considering the motion of a differential arc segment ds for which the string tension T and the viscous force F_Γ are balanced. From Figure 5-2 we see that $2T\sin(d\theta)/2ds$ is the total string tension per unit length in the arc segment, and this must be balanced by $F_\Gamma = -\Gamma\dot{r}$. Approximating $\sin(d\theta)\approx d\theta$ and replacing $d\theta$ by $d\theta = s/r$, we get:

$$\frac{T}{r} = -\Gamma\frac{dr}{dt},$$ (5.3)

which when integrated, yields:

$$r = \sqrt{\frac{2T}{\Gamma}(t_0 - t)}.$$ (5.4)

Thus, we expect loop radii to shrink with time according to the following general expression:

$$r \propto (t_o - t)^\alpha,$$ (5.5)

where the theoretical prediction gives α=0.5.

Loop collapse data

Our experimental goal was to measure the exponent α in Eq. (5.5), by observing the decrease in radius r of several loops. We selected seven events from our coarsening data pressure cell runs (see Section 5.2.3) which happened to leave nearly circular isolated loops at a late stage in the evolution of the system, and measured r as a function of $t_0 - t$, t_0 being the time of disappearance of the loop.

Fig. 5-3 shows data from a typical loop collapse, for which the exponent was α=0.49±0.002. Fig. 5-4 shows the exponents calculated from seven events chosen for having eccentricities[2] less than 0.6. Averaging these results gave α=0.50±0.03, which is in agreement with the expected

---

[2]Eccentricity is defined as $e = \sqrt{a^2 - b^2}/a$, where $2a$ is the length of major axis and $2b$ is the length of the minor axis
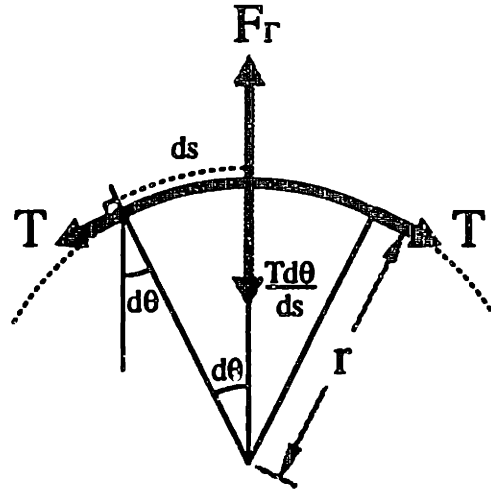
Figure 5-2: Relationships used in calculating the rate collapse of a $\pm\frac{1}{2}$ loop.

value of 0.50. The loops we observed did not leave monopoles behind, nor did they collapse around monopoles. Hence, these loops must have consisted of equal numbers of $+\frac{1}{2}$ and $-\frac{1}{2}$ string segments. Finally, from Eq. (5.4), we estimated that T/Γ varied from about about 200 to 300 μm^2/second in the 5.6 to 8.3 MPa, 37°C regime.

Loop density data

An understanding of the behavior of the density of loops ρ_l versus time after an isotropic→nematic phase transition is important because if the system has truly reached a scaling state, we expect ρ_l to have a large value at early times, and to decrease monotonically. Measurement of ρ_l is simple: we define a $\pm\frac{1}{2}$ loop in this experiment to be any isolated, closed length of $\pm\frac{1}{2}$ string. In turn, "isolated" is defined as not being connected to any other $\pm\frac{1}{2}$ string. Connections to ± 1 strings are permitted (± 1 strings have a much lower string tension than $\pm\frac{1}{2}$ strings, and therefore the behavior of $\pm\frac{1}{2}$ strings is believed to dominate the coarsening process). The procedure for this experiment is to slowly play back recorded videotapes of pressure cell runs (described in Section 5.2.3), and identify the times at which loops are created and annihilated. Timelines showning the lifetimes of loops can then be combined to calculate the number of loops in existence at any one point in time, and division by the measured cell volume converts this to a loop density, $\rho_l(t)$.

Log-log plots of these data, taken from run 8 (see 5.2.3 for the operating parameters) are shown

79
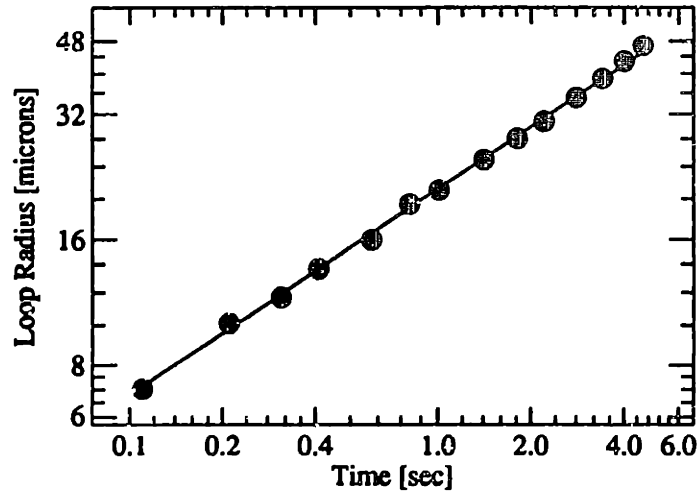
Figure 5-3: Typical data showing the loop radius as a function of $t_0 - t$, where t_0 is the time at which the loop disappears.
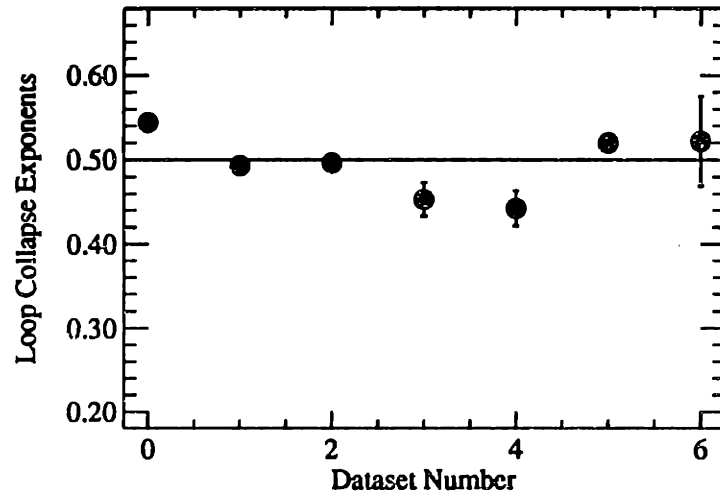
Figure 5-4: The loop collapse exponents α obtained from observing seven events. The measured α are close to the expected value of 0.5. Statistical errors are shown.

in Figures 5-5 and 5-6. Note that the late time ($t > 3$ sec.) behavior of ρ_l behaves as expected. The simple dimensional argument is that one loop should be found in each volume ξ^3, where ξ is the characteristic length scale of the system at a the time of interest. From the one-scale model, and from our coarsening data (section 5.2.3), we expect that $\xi \approx t^{-1/2}$. Thus, we expect $\rho_l \approx t^{-3/2}$, as seen.
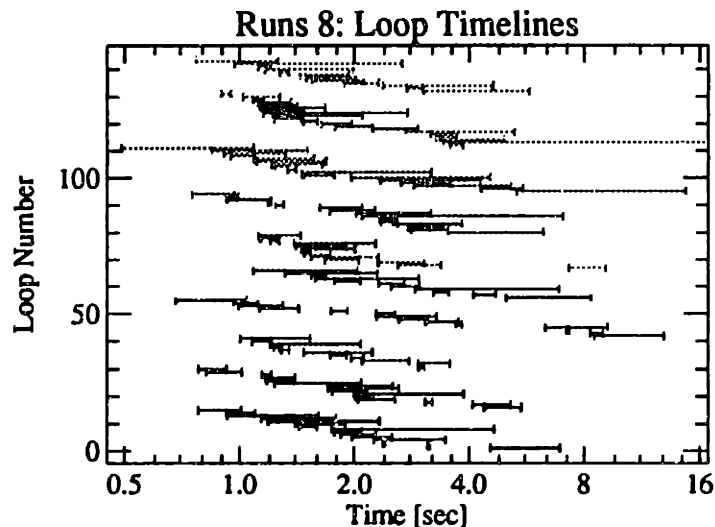
Figure 5-5: Timelines of loops found in ten pressure jump initiated phase transitions. Data collected by A. Pargellis.

However, the early and mid-time behavior of the system shows some anomalous behavior. As we mentioned earler, we expected ρ_l to decrease monotonically from an initial level reached almost immediately after the phase transition. This graph shows that many loops are created approximately one to two seconds after the phase transition, for this particular choice of operational parameters. One second is a very long time on the time scale of the speed of the phase transition, which we had estimated to take place in less than 30 ms. Although the defect density at times earlier than one second is too high to image (for the objective magnification and camera resolution we are using), we do not attribute the precipitous drop in ρ_l to experimental difficulty in identifying loops. Rather, we feel that one second is a firm lower bound on the times for which we believe we can reliably identify features in the system,

At $t = 1$ sec., $\xi \approx 90$ μm, which means that strings should be separated by about 90 μm.

81
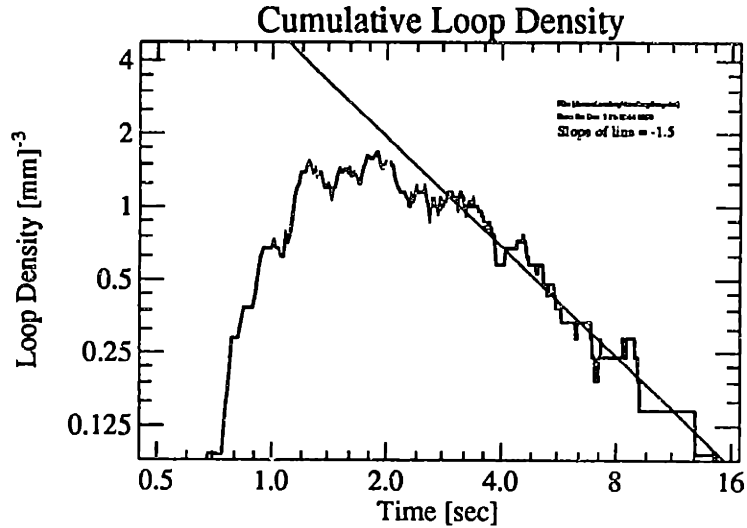
Figure 5-6: Cumulative loop density ρ_l from Run 8 data. The data is to be considered accurate for $t > 1.0$ seconds only. The straight line, with slope -3/2, shows that the late time scaling behavior of the ρ_l behaves as expected: $\rho_l \approx t^{-1.5}$. Data collected by A. Pargellis.

Allowing for the thickness of the cell, 230 μm, the observed strings should be separated by about $90^2/230=35$ μm, a distance which we find to be distinguishable in our 400 μm by 312 μm pictures. Furthermore, these measurements were taken by studying a large monitor showing the sequences, and the creation and annihilation times were individually measured, and weighed with experience gained from extensively studying the dynamics of the string interactions. Therefore, we have confidence in our data. We believe there is a definite anomaly in the $t < 3$ second behavior of $\rho_l(t)$.

A possible explanation for the initially low level of ρ_l, and its subsequent rise, is given by the defect energetics argument of Section 3.5. Another explanation comes from possible finite size effects. It is conceivable that the the boundary conditions at the window surfaces either encourage defects to move away from them, or attract defects which stick to the surfaces. We have considered these effects, and will study them further in the next subsection.

5.2.3 String Coarsening

The most interesting behavior of the tangle of defects created in the isotropic→nematic phase transition is the coarsening process. Theoretical arguments of the Lifshitz-Slyosov type[LS61] describe how late time coarsening dynamics should proceed. The premise is that the string network may be

82

characterized by a single scale ξ, defined by $\rho_s \equiv \xi^{-2}$, where ρ_s is the line length per unit volume (otherwise known as the string density). The typical radius of curvature of the strings, and the typical inter-string separation are both proportional to ξ. This model is known as the "one-scale" model for string evolution, in cosmology theories. Our examination of the string coarsening dynamics in the NLC provide a striking confirmation of this theory. In the following discussion, I sketch the theory, present our data, then consider possible secondary influences such as finite-size effects.

Theory

The characteristic velocity v of a string is found by equating the characteristic string tension force, which is proportional to T/ξ, with the characteristic friction force Γv per unit length. We find that $v \propto T/\Gamma\xi$. The rate of loss of energy from the string network is thus $\dot{W} = Tv\rho/\xi = T^2\rho^2/\Gamma$ per unit volume. The rate of decrease of ρ can be calculated by equating this energy loss with the time derivative of the string energy density $W \propto T\rho$ to get:

$$\frac{d\rho}{dt} = -c\frac{T}{\Gamma}\rho^2 , \tag{5.6}$$

where a constant of proportionality, c, has been introduced.

A second effect which contributes to the coarsening of the string network is the loss of length from the long strings into loops: this is always favored by phase space over reconnection of loops onto long string[AT89]. A long string loses length to loops at a rate given by a geometrical constant times v/ξ, which scales the same way as the viscous force damping term. Thus, the constant c may be taken to include both these effects. Integrating Eq. (5.6), we find that the general scaling solution is given by

$$\rho = (\Gamma/cT)t^{-\nu} , \tag{5.7}$$

with $\nu = 1$ expected.

Similar arguments have been given in the condensed matter literature before – applied both to domains in two dimensions[Lif82], and strings in three[TH87]. With the *assumption* of scaling, the derivation of the exponent is little more than dimensional analysis. However this basic assumption seems to have been studied and tested more comprehensively in the cosmological literature[AT89, BB89, AS90] for string networks at least.

Coarsening data

We experimentally tested the $\rho \propto t^{-1}$ string density scaling prediction by recording high speed video pictures of the evolution of the string network which forms after performing a rapid pressure jump (of ΔP) to force an isotropic→nematic phase transition. The data were analyzed by the image processing procedure described in section 5.1.4. Four pictures typical of the string tangle in evolution are shown in Figure A-14.

We estimated the depth of the visible region to be 158±8 μm for the $\Delta P \approx 2.00$ MPa run and 234±23 μm for the other three. With greater cell thicknesses, we found that identifying strings became more difficult, because of occlusions and light scattering. All the data were taken using a 10X objective, with a depth of field large enough such that all defects anywhere between both surfaces of the windows were clearly identifiable. Ten different observations of the NLC after pressure jump initiated phase transitions were recorded for each of the four data sets, known as runs 5, 7, 8, and 9. All the runs began at the same state, at approximately 37°C and 3.6 MPa, but differed in the depths of the pressure jumps. For runs 5, 7, 8, and 9, ΔP was 2.00, 2.62, 4.69, and 2.28 MPa, respectively. The pressure jump depths of the four runs are indicated on the phase diagram in Figure 5-7.

We found that for times between 1 second and 32 seconds, the string network was low enough in density for the strings to be clearly distinguished. Our scaling results are shown in Figure 5-8. The statistical errors, obtained by averaging over several runs, are smaller than the symbol sizes. Repeating the experiment at increasing ΔP, we found the same scaling with time, but decreasing string density at a fixed time, consistent with the effect expected, where if the string tension is increased, so was the scaling value of ξ.

The data do show systematic deviations from straight line behavior. We expect that at early times, line thicknesses (caused by the finite camera resolution) spuriously lower the calculated string density because of string overlap, and that at late times, image noise significantly increases the density estimation (it is not as detrimental to the early-time data, because the amount of noise is constant, and the string density is higher for smaller t). Omitting the first and last points in each data set, a least squares fit gives a scaling exponent of ν=1.02±0.04, which is close to the predicted t^{-1} power law.
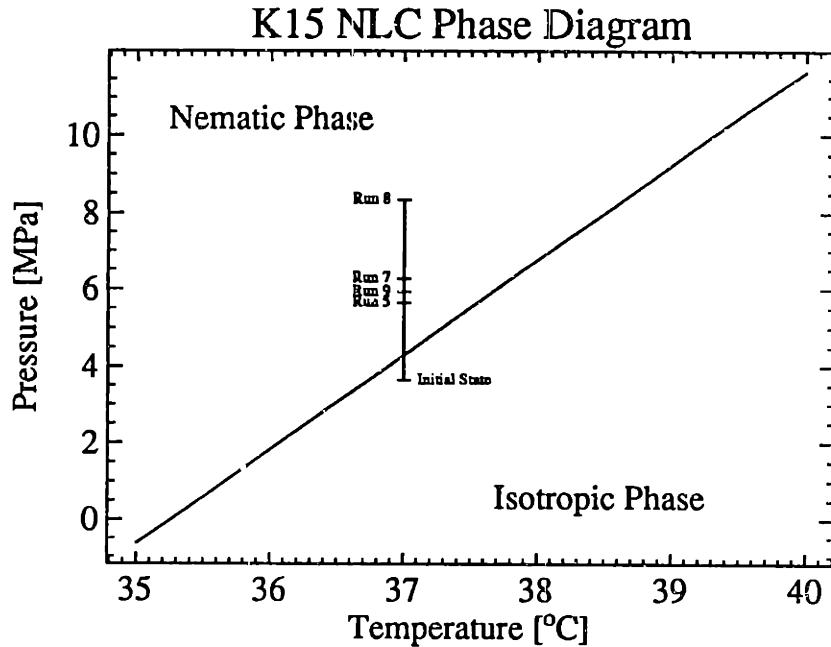
Figure 5-7: Phase diagram showing the four pressure cell coarsening data runs.

String density calibration

String density is measured in units of line length per unit volume. As I mentioned in Section 5.1.4, our simple calibration method to measure string density was to count the number of lines intersecting a line drawn across an image; the number of intersections divided by the cross sectional area determined by the line and the thickness of the cell would thus give a quantity related by a geometrical factor to the actual string density.

We later re-measured the string density by using a commercial tool available for measuring distances on a map. We selected a single set of images from the run 9 data, showing the string network at $t = 5.8$ sec., and found the average line length to be about 88.5 mm per mm^3. This value was only about 1.4 (about $\pi/2$) times larger than the $\rho_S \approx 55.6$ mm^{-2} result which we had previously arrived at. Because the new technique allowed the absolute calibration of ρ_S, we re-scaled our data to be 1.4 times larger. The data in Figure 5-8 are calibrated absolutely.
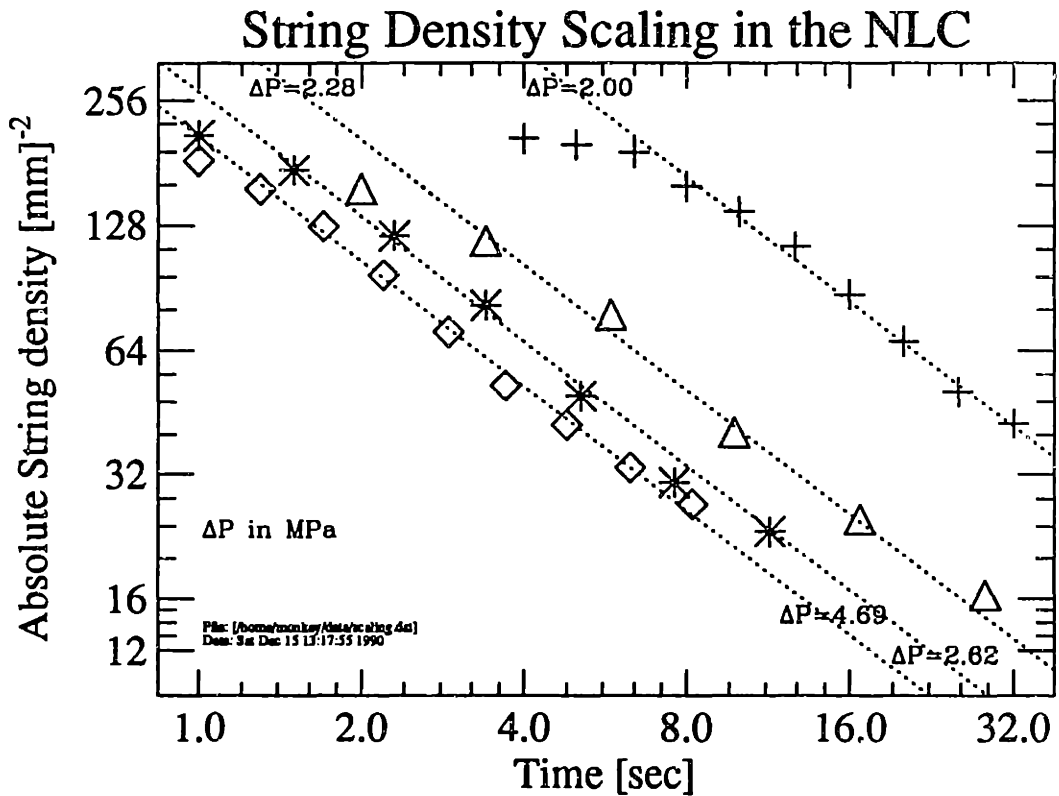
Figure 5-8: String density data, accumulated at four different ΔP. The scaling relationship was experimentally determined to be $\xi \approx t^{0.51\pm0.02}$, where $\rho \equiv 1/\xi^2$. For higher ΔP, the string tension is higher and one expects from the analysis in the text for the scaling density to be lower, as is observed. Errors are smaller than the symbol sizes. The data were calibrated absolutely (see text). Time is measured from the pressure-jump initiated phase transition.

86

Interpretation of the data is, however, complicated by possible finite size effects due to the interactions with the window surfaces. We saw no evidence of pinning of defects to the interfaces. Because of our treatment of the windows, we saw no marbled patches. Furthermore, though disclination lines were sometimes observed to terminate on the surface, they showed no evidence of pinning. Consequently, it may have been possible for the defect tangle to pull away from the windows and become concentrated in the center of the cell. To check this possibility, we studied the evolution of the number of string crossings seen in our data. As we discuss in the following section, these "X-intersections" should scale as $\rho_X \propto \rho_S^2$, where ρ_S is the string density. Because intersections are one-dimensional objects, they should be found with density $1/\xi^3$, but because our images are two-dimensional projections of a three-dimensional system, an extra factor of ξ must be added to reflect the possibility of string-string occlusions producing X-intersections in the pictures. Figure 5-9 shows our results from analyzing data from the ΔP=4.69 MPa run. The data points at late times show a consistent deviation below the t^{-2} behavior expected for a three-dimensional system whose line density is given to scale as t^{-1}. However, at early times there is good agreement.
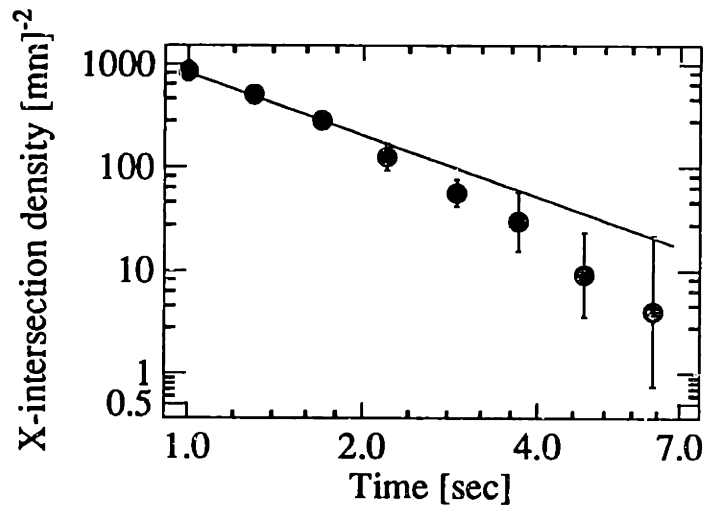
Figure 5-9: Scaling behavior of the number of $\pm\frac{1}{2}$ string crossings vs. time from the Run 8 data. The error bars indicate the statistical errors from averaging eight data sets. The solid line shows the expected t^{-2} scaling for the bulk.

A model for the deviation observed in the behavior of ρ_X vs. t can be constructed by assuming that the cause is a shrinking of the effective thickness d of the defect layer in the pressure cell. Thus, by extracting d from the data in Figure 5-9, a correction for the proper string density ρ can be estimated. Using this procedure, and fitting to the linear regime in the corrected $\ln \rho$ vs. $\ln t$ data, a corrected scaling exponent of $\nu_c=0.93\pm0.06$ is obtained. This number can be understood as a bound on possible deviations in bulk behavior for the coarsening exponent ν, and is reasonably incorporated as an additional contribution to the error bars originally given for ν. Our conclusion is that the bulk scaling exponent for our K15 system is $\nu=1.02\pm0.09$.

5.2.4 String Intersections

Two $+\frac{1}{2}$ strings may intersect at a three-string vertex with a $+1$ also string coming off of the junction (this is also true for strings of the opposite sign). We denote such intersections as "T-intersections," because of the way they often appear in our pictures; a schematic drawing of a T-intersection is shown in Figure 5-10. Simpler yet, when viewed as a two-dimensional projection (we observe our three-dimensional slab of NLC from the top and see everything through to the bottom), strings cross each other, we call these crossings "X-intersections." The scaling of T and X-intersections is expected to be similar to the behavior of ξ vs. time.
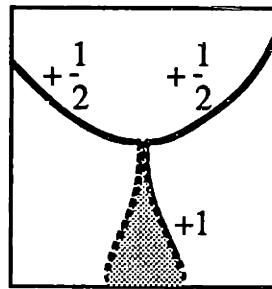
Figure 5-10: Intersection between two $+\frac{1}{2}$ strings and one $+1$ string. This is known as a "T-intersection."

Because string intersections are one-dimensional objects, we expect to find one intersection per volume ξ^3, such that the density of intersections should be $\rho = 1/\xi^3$. However, X-intersections are generated by the occlusion of one string by another (occlusions producing apparent T-intersections do not happen, because the flux of ± 1 strings is pinched at T-intersections, and otherwise diffuse).

String Observable	Expected Scaling Behavior
String density	$\rho_S \approx t^{-1}$
T-intersection density	$\rho_T \approx t^{-1.5}$
X-intersection density	$\rho_X \approx t^{-2}$

Table 5.1: Scaling behavior of the string, T-intersection, and X-intersection densities as a function of time, assuming that the characteristic length scales as $\xi \approx t^{1/2}$.

Thus, we expect that while the density of T-intersections should scale as $\rho_T = 1/\xi^3$, the density of X-intersections should scale with an extra factor of ξ: $\rho_X = 1/\xi^4$. Rewritten using the relationship $\xi \approx t^{1/2}$, and including the string density for comparison, we arrive at the scaling results given in Table 5.1.

Data measuring the behavior of ρ_S and ρ_X were already acquired for the analyses of the previous subsection; we added to our collection by manually counting the number of T-intersections from run 7 data. Our results, shown in Figure 5-11, agree well with the predictions, at early times. The systematic deviation for late time datapoints can be understood in terms of the finite size effects discussed in Section 5.2.3.

5.3 Monopole Statistics

The second class of defects observable in the NLC are monopoles (corresponding to nontrivial $\pi_2(\mathcal{M}_0)$). Monopoles appear as dark dots sitting on ± 1 strings, where the flux appears to converge to a single point. We see relatively few of them in the pressure jump initiated phase transition data, but they are created in abundance following temperature quenches. We do not know exactly why this is the case, but believe that it may have something to do with the speed of the phase transition. In trying to understand monopole behavior, and creation and destruction mechanisms, we have systematically studied the evolution of monopole density in our pressure cell data, in a manner similar to our study of loop densities.

5.3.1 Creation and Annihilation Mechanisms

We observed that the most common mechanism for creation of a monopole is the collapse of a $\pm\frac{1}{2}$ loop carrying ± 1 monopole charge and having two ± 1 strings attached to it. This process is
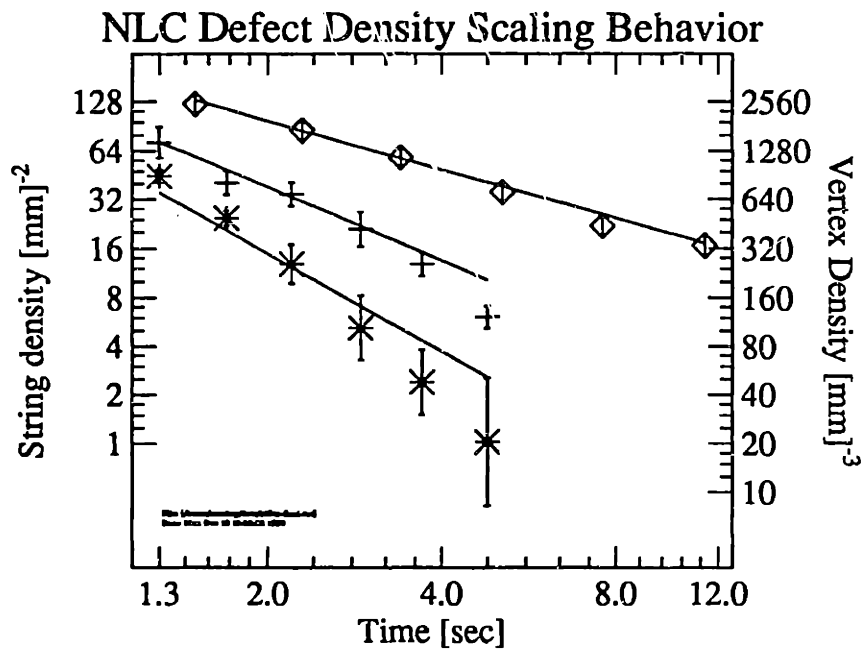
Figure 5-11: Experimental data showing the scaling behavior of the string density ρ_S (diamonds), the T-intersection density ρ_T (plus-symbols), and the X-intersection density ρ_X (stars). The string density scale should be multiplied by 1.4 to give the actual, calibrated string length per unit volume (this has no effect on the slope, which is the major point of this graph). The slopes of the lines indicate the scaling behavior of the three observables: $\rho_S \approx t^{-1}$, $\rho_T \approx t^{-1.5}$, and $\rho_X \approx t^{-2}$.

diagrammed in Figure 5-12. Another mechanism we believe we have have observed is the production of a monopole by two ± 1 strings which are attached to a $\pm\frac{1}{2}$ string drawing together and pulling off, as shown in Figure 5-13. We have not observed any other mechanisms for creating monopoles in data from the pressure cell experiment. Two events, showing the creation of a monopole by the collapse of a $\pm\frac{1}{2}$ loop, are shown in Figures A-17 and A-18.
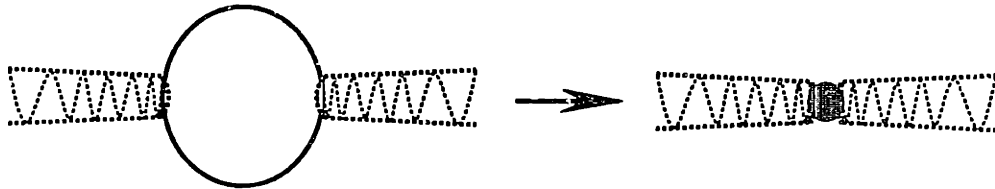
Figure 5-12: Collapse of a $\pm\frac{1}{2}$ loop into a monopole.
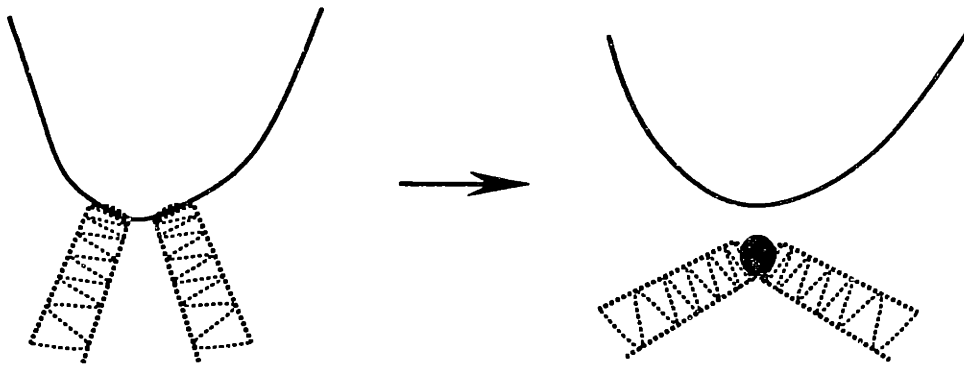
Figure 5-13: Creation of a monopole by two ± 1 strings pinching off of a $\pm\frac{1}{2}$ string.

5.3.2 Monopole Density

Monopoles seem to be created only infrequently. We have gathered statistics on the density of monopoles as a function of time $\rho_m(t)$ from the data of runs 7, 8, and 9. Our results are shown in Figure 5-14. The top plot gives ρ_m for the three data sets; the middle plot shows how they look when t is multiplicatively scaled for the data of runs 7 and 9, to bring the means of the three distributions together. The cumulative monopole density in the bottom plot is simply the sum of the three rescaled distributions. The two straight lines show the approximate asymptotic slopes of each side; they both

have slope −3. We do not have a theory explaining why these slopes should be −3.

5.4 Texture Decay

Texture is the third class of defects in the NLC I consider here. It can be a difficult topological defect to observe experimentally, especially because it is entirely nonsingular except at it moment of collapse. Ideally, we would imagine being able to create an isolated texture defect which can be observed as it delays. We set about doing this using our thin film apparatus and mechanical manipulators, but discovered that though we came close to producing the textures described in Section 3.4, the objects we saw decayed unexpectedly. This occurred several times. One such sequence is shown in the left hand column of Figure A-16. Our observations were that although we could create two nearly concentric ±1 strings, they would always be unbalanced enough that instead of shrinking uniformly, the rings would pinch off at one point, and form a monopole-antimonopole pair.

Turok analyzed this decay behavior by performing a simple relaxation simulation of a liquid crystal in the one constant approximation. He discretized space as a cubic (40^3) lattice, and performed multiple sweeps through the lattice, minimizing the energy at each site as a function of the director at that site while keeping the director at neighboring sites fixed. The initial shape and size of the texture was fixed by $\chi(r) = \pi(1 + \tanh((r - S)/W))$, where S determined the size of the ring, and W its width. A perfectly circular texture of this form collapsed with the inner ring first shrinking to a point and forming a monopole, then the outer ring subsequently collapsing to annihilate the monopole. However, when the texture was slightly perturbed (replacing the argument of the hyperbolic tangent by $(r - S(1 + \frac{1}{2}\cos\phi))/W$, with ϕ the azimuthal angle), Turok observed a very different evolution. Similar to our observations in the thin film NLC, the ±1 ring pinched off at one point, forming a monopole-antimonopole pair which was clearly identifiable in plots of the director field. The monopoles would then travel around opposite halves of the ring and annihilate on the far side. The simulation results are shown alongside our experimental observations in Figure A-16.

A detailed examination of the two monopoles and the texture equation indicates that the two ±1 strings emanating from the monopole are apparently escaped in the same direction on either side of the monopole. This possibility is contrary to the expectation that the flux on either side of a monopole should be escaped in opposite directions (to see this, consider a hedgehog monopole, with all the $\vec{n}$ pointing radially inwards toward the origin, and note that in each half space, all of the rods

92
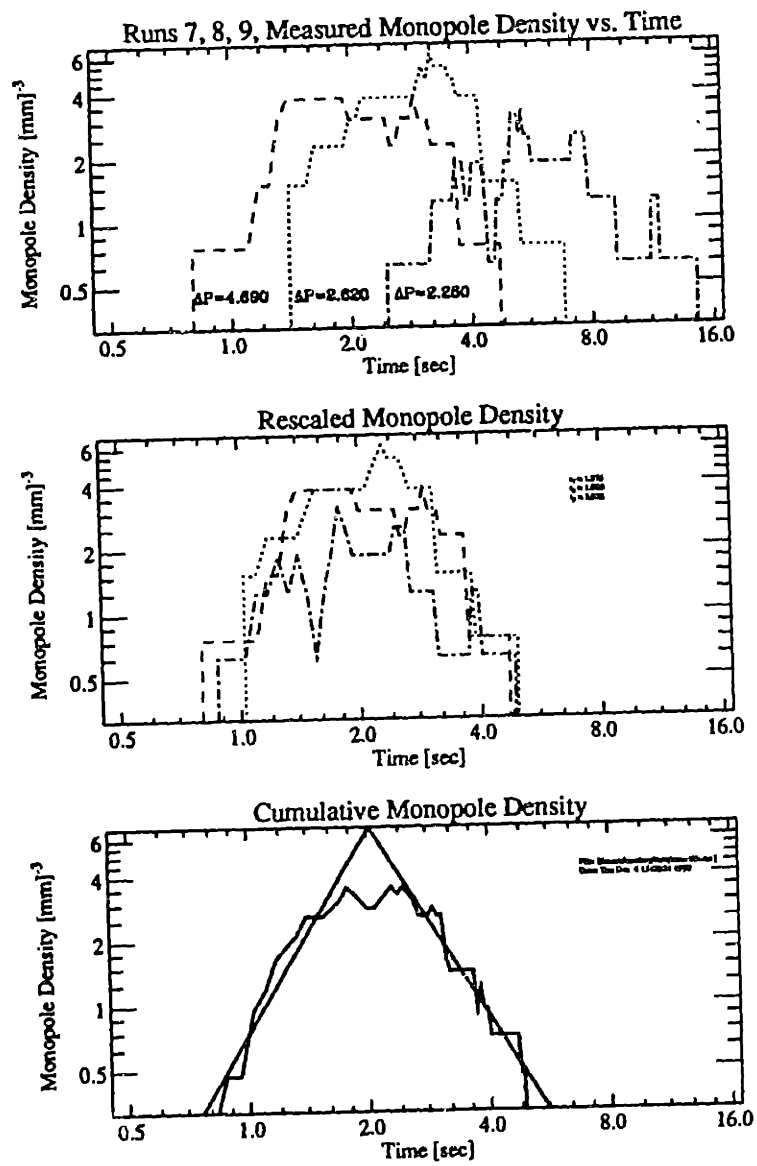
Figure 5-14: Three plots showning our monopole density data, $\rho_m(t)$.

are pointing towards the other side). We believe that there is a simple explanation for this seeming contradiction, and anticipate being able to resolve it through a direct examination of the director field of the simulation results.

Our conclusion is that texture has a decay channel into monopole-antimonopole pairs. Viewed in terms of Hopf links, the monopole and antimonopole evidently act as sources from which all lines emerge. Apparently, the linked lines all cross at once, forming the pair, and then break apart as the monopole-antimonopole pair move apart.

5.5 Defect Interactions

Thus far, in our discussion of the dynamical behavior of defects in the NLC, I have primarily concentrated on analyzing the properties of macroscopic observables such as defect densities. In this section, I turn to a microscopic characterization of defect dynamics, by considering "pair" and higher-order interactions. I consider the following questions: How do defects interact? What can interactions result in? How often do they occur?

5.5.1 Event Classifications

We have already seen examples of several defect interactions, namely, string intercommutations (Figure A-13) and loop collapses. In the following discussion. I will refer to these interactions not as continuous processes, but rather, as specific events which occur within immeasurably small time windows. I will characterize events by their reactants and products; for example, $\pm\frac{1}{2}$ string intercommutations take place between two $\pm\frac{1}{2}$ strings, and result in two $\pm\frac{1}{2}$ strings with different orientations than the original two strings. Loop collapses are events which take place when a $\pm\frac{1}{2}$ string loop disappears into nothingness. Another event, shown in Figure A-19, is the decay of a ± 1 string connecting two parts of the same $\pm\frac{1}{2}$ string. Interactions leading to monopole annihilations and creations are also events worth noting.

I and B. Yurke have developed the following event classification scheme, based on our experimental observations of defect interactions in our pressure cell data. We have identified sixteen basic events, identified by a event code number and pictograph, as described in Table 5.2. The basic components are $\pm\frac{1}{2}$ strings, ± 1 strings, and monopoles. We have left out texture, because we have not identified any texture defects which have been created spontaneously; none appear in the pressure

94

cell data. $\pm\frac{1}{2}$ strings are singular defects, and appear as sharp black lines; thus, we represent them in our pictographs as single black lines. ± 1 strings are nonsingular, and appear as diffuse "flux tubes." Thus, we represent ± 1 strings by pairs of dotted lines. Monopoles are singular; they are represented as black dots which sit on ± 1 strings at points where the flux lines (the dotted lines) converge.

5.5.2 Quantum Numbers?

The construction of an event classification scheme leads to the question of the existence of natural groupings for the various events. We have studied five groupings, based on quantities which are changed incrementally in certain events. These quantities are the number of T-intersections, monopoles, links, isolated $\pm\frac{1}{2}$ strings, and isolated ± 1 strings (Table 5.3). We symbolize their change as Δn_T, Δn_M, Δn_L, Δn_{1s}, and $\Delta n_{\frac{1}{2}s}$, respectively, and itemize their behavior for the various events in Table 5.4.

Note that $\Delta n_T = 1$ refers to the creation of *one* T-intersection. Most of the events in Table 5.4 either create or destroy two T-intersections; never have we observed the creation or destruction of a single T-intersection. One further note about Δn_{1s} and $\Delta n_{\frac{1}{2}s}$: we define an "isolated" segment of string as one which is not attached to any other defect participating in the event.

We gathered statistics comparing the probable occurrences of each of our selected events. We recorded the time and location of 435 events observed in our Run 8 pressure cell data. The resulting probabilities, also given in Table 5.4, are shown in a histogram in Figure 5-15. Figure 5-16 shows the number of occurrences of events #1 and #8 as a function of time; these data are typical of our statistics. We found that to the resolution of our data, the relative probabilities of different events remained approximately constant as a function of time after two seconds.

5.5.3 Branching Ratios

The occurrence probabilities of Table 5.4 can be reduced by categories of observables to give "branching ratios," i.e., probabilities of different mechanisms which result in the change of a certain quantum number. I tabulate our results in Tables B.1 through B.9.

One of our results can be explained by a simple counting argument. Monopoles can be created when a $\pm\frac{1}{2}$ loop collapses and brings two ± 1 strings together, as indicated in #15. However, not all loop collapses bringing together ± 1 strings result in the creation of a monopole. If we postulate

95
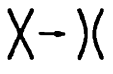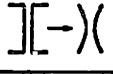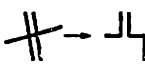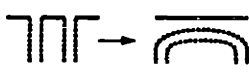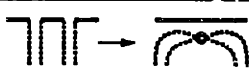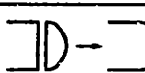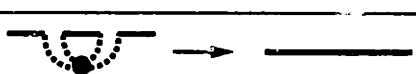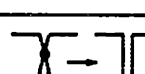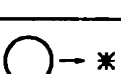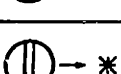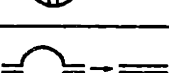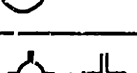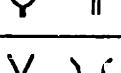
Code	Event pictograph	Description
1	$X\!\to\!)($	Intercommutation of two $\pm\frac{1}{2}$ strings (The two initial strings are separated in space)
2	$][\!\to\!)($	Decay of a ±1 across two $\pm\frac{1}{2}$'s into two $\pm\frac{1}{2}$'s
3	$][[\!\to\!)($	Decay of two ±1's across two $\pm\frac{1}{2}$'s into two $\pm\frac{1}{2}$'s
4		Intercommutation of a $\pm\frac{1}{2}$ and a ±1 resulting in a $\pm\frac{1}{2}$ with two T-intersections
6		Unlinking of two ±1's from a $\pm\frac{1}{2}$
7		Unlinking of two ±1's from a $\pm\frac{1}{2}$ resulting in a single $\pm\frac{1}{2}$ and a monopole carrying ±1
8	$]D\!\to\!D$	Decay of a ±1 connecting two parts of the same $\pm\frac{1}{2}$ into a single $\pm\frac{1}{2}$
9		Decay of a ±1 connected at both ends to a straight segment of $\pm\frac{1}{2}$
10		Decay of a monopole carrying ±1 connected at both ends to a straight segment of $\pm\frac{1}{2}$
11	$Y\!\to\!T$	Decay of a monopole sitting on a ±1 by absorption into a $\pm\frac{1}{2}$
12	$\bigcirc\!\to\!*$	Collapse of a $\pm\frac{1}{2}$ loop (no end products)
13	$\textcircled{$\parallel$}\!\to\!*$	Collapse of a $\pm\frac{1}{2}$ loop with a ±1 across it
14		Collapse of a $\pm\frac{1}{2}$ loop with two ±1's coming out at either end, resulting in a single ±1
15		Collapse of a $\pm\frac{1}{2}$ loop with two attached ±1's, resulting in a monopole carrying ±1
16		Collapse of a $\pm\frac{1}{2}$ loop with four attached ±1's, resulting in a four-±1 vertex which escapes
17	$X\!\to\!\bowtie$	Intercommutation of two $\pm\frac{1}{2}$'s resulting in two $\pm\frac{1}{2}$'s connected by a ±1

Table 5.2: Defect event classifications.

Observable	Description
Δn_T	T-intersection creation
Δn_M	Monopole creation
Δn_{1s}	Creation of isolated ± 1 string segments
$\Delta n_{\frac{1}{2}s}$	Creation of isolated $\pm\frac{1}{2}$ string segments

Table 5.3: Description of our five postulated "quantum numbers."

Defect Interaction Event Probabilities
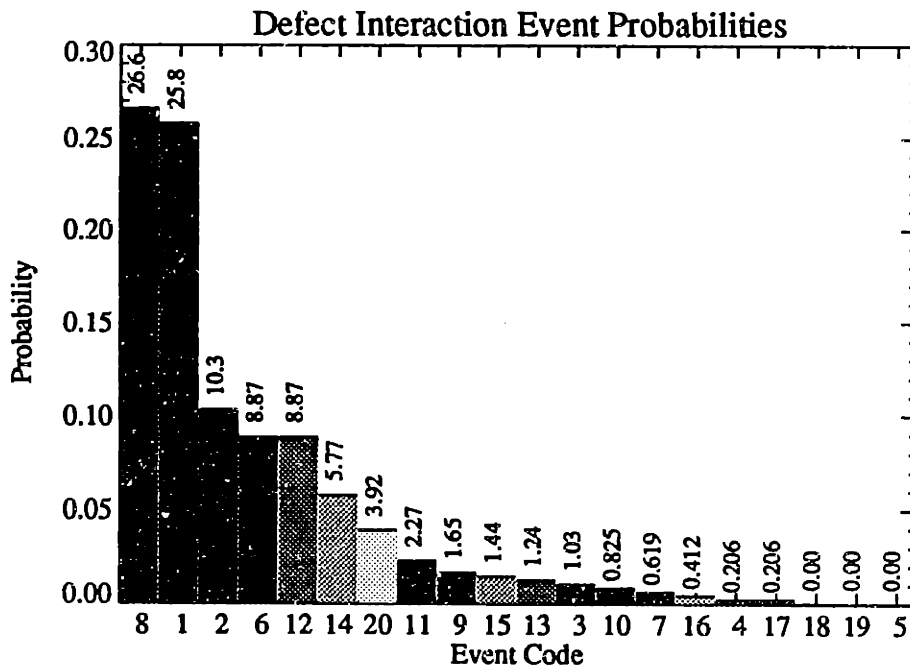
Figure 5-15: Histogram showing the relative probabilities of occurrence for the 16 events we classified. Code 20 refers to unclassifiable events, which were recorded to provide an estimate of the error in our measurements. Codes 18, 19, and 5 can be ignored.

Code	Event	% Prob.	Δn_T	Δn_M	Δn_L	Δn_{1s}	$\Delta n_{\frac{1}{2}s}$
1	X→)(	26.6					
2	][→)(	10.3	-2		−1	−1	
3	]][→)(	1.0	-4		−1	−2	
4	╫→⅃⌐	0.2	+2		+1		
6	⫟⫟→⌒	8.9	-2		−1		
7	⫟⫟→⌒•	0.6	-2	+1	−1		
8	])→)	25.8	-2			−1	
9	⌣→—	1.7	-2			−1	
10	⌣•→—	0.8	-2	−1		−1	
11	X→⫟⫟	2.3		−1			
12	○→*	8.9					−1
13	⊕→*	1.2	-2			−1	−1
14	○→=	5.8	-2				−1
15	○→><	1.4	-2	+1			−1
16	◇→╫	0.4	-4				−1
17	X→⊁	0.2	+2		+1	+1	

Table 5.4: Defect events, their probabilities, and associated observables. Probabilities were measured from the observation of about 485 events from Run 8 data. Code 20 (not listed above) refers to unclassifiable events, which were found with probability 3.9%.

Occurances of Event #1 vs. Time

Occurances of Event #8 vs. Time
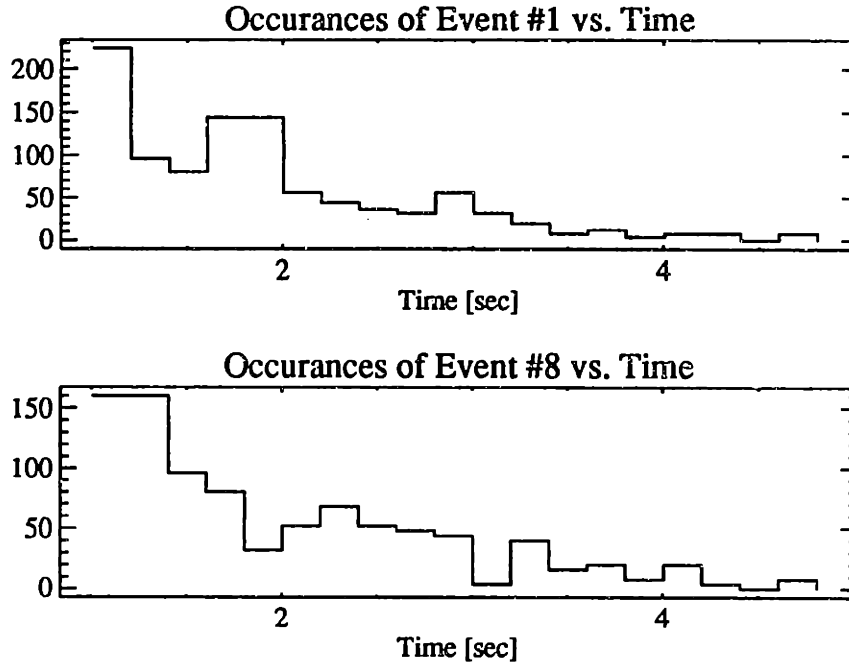
Figure 5-16: Number of occurrences of events #1 and #8 as a function of time. The bin size is $\Delta t = 0.2$ sec. Not all events were recorded for $t < 2.0$ sec.

q	Λ	Monopole produced?
+1	+1	No
+1	−1	Yes
−1	+1	No
−1	−1	No

Table 5.5: Monopole production possibilities. q and Λ are the relative charges and escape directions of two ±1 strings which are brought together by a loop collapse. Contrary to the expectations tabulated above, Turok's texture collapse simulations indicate that a $q = -1$, $\Lambda = +1$ configuration (with the two ±1 strings of opposite charge but escaped in the same direction) might also produce a monopole.

that monopoles may only be created when two ± 1 strings of the same charge and opposite escape directions are brought together, then the probability of the creation of a monopole by a the collapse of a loop with two attached ± 1 strings is found to be 25% as follows: first, assign each of the two strings a charge, $q_{1,2} = \pm 1$, and an escape direction $\Lambda_{1,2} = \pm 1$. The relative charges and escape directions can be represented by the products of the individual quantities: $q = q_1 q_2$ and $\Lambda = \Lambda_1 \Lambda_2$. The four possibilities are enumerated in Table 5.5. By our postulate, only one of the four combinations of charge and escape direction result in the production of a monopole. Reading from Table 5.4, we find that of the combination of events #14 and #15, event #15, which results in the production of a monopole, occurs 20% of the time. This is in reasonable agreement with our prediction of 25%.

5.5.4 Summary

My discussion of defect interactions ends the presentation of our experimental observations. I have not yet had an opportunity to further analyze the statistics gathered, but can imagine several interesting experiments. First, I expect to be able to greatly improve the time resolution of our statistics by gathering more data; we hope to be able to quantitatively identify the different epochs in the evolution of the NLC system which are dominated by proliferous production of certain defects. We also intend to perform space-time correlation measurements on our data; we know from our observations that some events are highly interdependent - for example, the collapse of a loop is necessarily predicated by several $\pm \frac{1}{2}$ string intercommutations. These observations may be quantified using the classification scheme we have developed.

In concluding this section, I present a typical sequence of observations showing the combined action of various events, in Figure A-20. We see the creation of a loop through several $\pm \frac{1}{2}$ string intercommutations, and the decay of several ± 1 strings. The loop subsequently collapses. I find it wonderful to observe the way events take place while preserving the scaling behavior of the system which we have observed.

5.6 Summary

The primary findings of this chapter are summarized in Figures 5-3, 5-6, 5-8, 5-11, and 5-14, and Table 5.4. I have shown that the dynamical behavior of strings observed in the NLC are consistent with expectations from the "one-scale" model of cosmology, and do not contradict expectations from

the workings of the Kibble mechanism. However, our observations of loop and monopole densities vs. time do not agree with expectations from a simple scaling model. Though such deviations may perhaps be explained by the relative energetics model of Chapter 3, I really do not fully understand all our observations.

Thus, I turned to a characterization of the microscopic behavior of defect interactions, by devising an event categorization strategy in which the probabilities of creating T-intersections, monopoles, new links, and isolated string segments can be quantified directly. Though I do not view our categorization as comprehensive, it certainly encompasses all of the interactions we have observed in our data on defect behavior in pressure jump initiated NLC phase transitions. I challenge the interested reader to attempt to come to a more complete theoretical understanding which predicts the branching ratios of the events we have described.

This chapter concludes the discussion of my work. I next summarize briefly my principle findings, and present my suggestions for future work.

Chapter 6

Conclusion

The research presented in this thesis represents significant progress in understanding the dynamical behavior of topological defects in a simple condensed matter system. Through my numerical and experimental study of the nematic liquid crystal (NLC), I have developed valuable tools for investigating defect behavior. I have also gathered data both supporting and contradicting various cosmological scenarios for defect formation and evolution. The principle accomplishments of my work are summarized in Figure 6-1.

6.1 Future Work

A multitude of future projects can be spawned from the work I have accomplished in this thesis. Numerical simulations of dynamical systems such as the NLC will continue as a matter of course, but the insight gained in this work will likely influence the particular numerical experiments which will be performed. I also hope that the tensor field methods I presented will be useful. However, truth be said, the bulk of the most interesting research will be continuations of the experimental initiatives I have established. The pressure jump initiated phase transition data I carefully gathered has been the main source of our experimental data, and was worth all the tedium and painstaking attention to detail, but our experiences suggest new and even better techniques to develop and experiments to perform. Certainly, more challenges lie ahead. In this section, I summarize some of what I believe to be the most important projects currently facing us.

- Experimental confirmation of the applicability of the "one-scale" model of string network evolution for describing the coarsening behavior of a tangle of string defects in the nematic liquid crystal, by systematic measurement of string density as a function of time.

- Formulation of a defect interaction event categorization strategy, and associated "quantum numbers" which identify fundamental processes such as T-intersection, monopole, and link creation and annihilation.

- Accumulation of statistics describing the evolution of monopole, loop, T-intersection and X-intersection densities as a function of time; measurement of event "branching ratios."

- Experimental observation of a dynamical mechanism for texture decay, string intercommutation, and loop collapse.

- Development of NLC equations of motion utilizing a SO(3) tensor field.

- Qualitative prediction of relative defect abundances based on a comparison of the total energy of each defect within a volume ξ^3.

- Design and implementation of two experimental apparatuses for observation of defect dynamics in a thin film and bulk volume of liquid crystal.

Figure 6-1: Principle accomplishments of this thesis.

104

6.1.1 Numerical Simulations

Possible future numerical simulation work includes further analysis of monopole production mechanisms and study of the means by which oppositely charged segments of $\pm\frac{1}{2}$ string seem to be able to link together continuously. I also believe that with little additional effort, the 2D SLC structure function and monopole density scaling results can be made self-consistent and rigorous; our study of defect energetics indicate that the monopole density should in fact *not* scale at times for which the characteristic length scale is small enough (compared to the monopole core size) that logarithmic corrections in the attractive force become important.

6.1.2 Experimental Research

There are many potentially interesting topics of research in the experimental arena. First and foremost, the classification of defect interaction events of Section 5.5 represents only the tip of an iceberg. A great deal of work remains to be done, for example, in formulating a model which explains theoretically what the different branching ratios which we measured *should* be. Furthermore, I expect that though our classification scheme will be extremely useful in future research, refinements are not unlikely.

Second, I believe that a more comprehensive test of the Kibble mechanism itself can be designed. At best, our experiments test the Kibble mechanism only inferentially; a detailed examination of the relative defect densities immediately after the phase transition would be a natural step. Also, Turok has suggested that it should be possible to predict the relative proportions of defects produced by a moving domain wall; such predictions could be tested by arranging to have a film of NLC undergo a slow phase transition while under observation by a high speed camera.

One final, obvious possibility is the study of defects in other liquid crystals, such as biaxial nematics, cholesterics, and lytropics. Liquid crystals composed of very large assemblies of molecules exist, and may be amicable for use in studying the details of defect core structure. We suggest an interferometric experiment in which the core of a line defect is imaged by coherent light; the size, and also any internal structure (such as an isotropic core region), should be quantifiable. Also, as I have noted, Bouligand has observed texture in cholesteric liquid crystals[Bou73]; if textures can be created in abundance in cholesterics, statistics can be gathered to quantify how they interact with other defects, and how they affect the evolution of a defect tangle.

6.2 Kirei Desu Ne!

In conclusion, I must say that liquid crystals are most fascinating systems to study. Not only are the pictures generated by the ensemble of molecules in a liquid crystal very beautiful, but also, the laws obeyed by these molecules are determined by aesthetically appealing symmetries in the fundamental physics of the systems. Furthermore, liquid crystals are amazingly easy for the experimentalist to work with, and because of the universality of symmetry breaking phenomena, analogies can be drawn to relate studies of defect dynamics in liquid crystals to theoretical studies in cosmology and particle physics. This study indicates that certain cosmological theories can indeed be tested successfully through laboratory observations of some physics in liquid crystals. I hope that more research in the same vein will be soon to follow. Liquid crystal research, in the context of cosmology and particle physics theories, promises to provide experimental insights which have never been within reach before.

Bibliography

[AC90]   B. Allen and R. R. Caldwell. Generation of Structure on a Cosmic-String Network. *Phys. Rev. Lett.*, 65:1705, 1990.

[AS90]   B. Allen and E. P. S. Shellard. *Phys. Rev. Lett.*, 64:119, 1990.

[ASM88]   J. G. Amar, F. E. Sullivan, and R. D. Mountain. Monte carlo study of growth in the two-dimensional spin-exchange kinetic Ising model. *Phys. Rev. B*, 37:196, January 1988.

[AT85]   A. Albrecht and N. Turok. Evolution of Cosmic Strings. *Phys. Rev. Lett.*, 54:1868, 1985.

[AT89]   A. Albrecht and N. Turok. Evolution of Cosmic String Networks. *Phys. Rev. D.*, 40:973, 1989.

[BB89]   D. P. Bennett and S. R. Bouchet. *Phys. Rev. Lett.*, 63:2776, 1989.

[BB90]   D. P. Bennet and F. R. Bouchet. High-resolution simulations of cosmic-string evolution I. Network Evolution. *Phys. Rev. D*, 41:2408, 1990.

[BC89]   R. A. Boie and I. J. Cox. A Theory of Edge Recognition. *BTL Technical Memorandum 11228-89712-09TM*, 1989.

[Bou73]   Y. Bouligand. Recherches sur les textures des etats mesomorphes 4. La texture a plans et la Morphogenese des Principales Textures Dans Les Cholesteriques. *Journal de Physique*, 34:1011, 1973.

[Bou74]   Y. Bouligand. Recherches sur les textures des etats Mesomorphes 6 – Dislications Coins Et Signification Des Cloisons de Grandjean-Cano Dans Les Cholesteriques. *Journal de Physique*, 35:959, 1974.

[Bou81]   Y. Bouligand. In R. Balian et al., editor, *Les Houches Session XXXV, Physics of Defects*. North Holland, Dortrecht, 1981.

[Bra89]   A.J. Bray. Exact Renormalisation-Group results for Domain-Growth Scaling in Spinodal Decomposition. *Phys. Rev. Lett.*, 62:2841, June 1989.

[CDTY90]   I. L. Chuang, R. Durrer, N. Turok, and B. Yurke. Cosmology in the Laboratory: Defect Dynamics in Liquid Crystals. October 1990. Submitted to *Sci.*

[CF90]   J. A. Cuesta and D. Frenkel. Monte Carlo simulations of two-dimensional hard ellipses. *Phys. Rev. A*, 42:2126, 1990.

[CK72]   P. E. Cladis and M. Kléman. Non-singular Disclinations of Strength S=+1 in Nematics. *Le Journal De Physique*, 33:591, may-jun 1972.

[CPT90]   D. Spergel C. Park and N. Turok. Large Scale Structure in a Texture Seeded CDM Cosmogony. *Princeton preprint, in preparation*, 1990.

[CRK90]   A. C. F. Colchester, R. T. Ritchings, and N. D. Kodikara. Image segmentation using maximum gradient profiles orthogonal to edges. *Image and Vision Computing*, 8, August 1990.

[CS79]   S. Chandrasekhar and R. Sashidhar. High-pressure studies of Liquid Crystals. *Advances in Liquid Crystals*, 4:83, 1979.

[CvSFK87] P. E. Cladis, W. van Saarloos, P. L. Finn, and A. R. Kortan. Dynamics of Line Defects in Nematic Liquid Crystals. *Phys. Rev. Lett.*, 58(3):222, January 1987.

[CW90]   A. Cumming and P. Wiltzius. Nucleation and Growth of Monodispersive Droplets in a Binary-Fluid System. *Phys. Rev. Lett.*, 65:863, 1990.

[Dcr64]   G. H. Derrick. Comments on Nonlinear Wave Equations as Models of Elementary Particles. *J. Math. Phys.*, 5:1252, 1964.

[dG74]   P. G. de Gennes. *The Physics of Liquid Crystals*. Claredon Press, 1974.

[dPT86]   F. de Pasquale and P. Tartaglia. Theory of Phase-transition Kinetics in Systems with Continuous Symmetry. *Phys. Rev. B*, 33:2081, 1986.

[DR78]   Dietrich Demus and Lothar Richter. *Textures of Liquid Crystals*. Verlag Chemie, 1978.

[Flu]   Minnesota Mining and Manufacturing Company, 3M Industrial Chemical Products Division. 3M Center, St. Paul, Minnesota 55144 (612-733-1710).

[Fur85]   H. Furukawa. A Dynamical Scaling Assumption for phase separation. *Advances in Physics*, 34:703, October 1985.

[GGS73]   C. J. Gerritsma, J. A. Geurst, and A. M. J. Spruijt. Magnetic-Field-Induced Motion of Disclinations in a Twisted Nematic Layer. *Physics Letters*, 43A(4):356, 1973.

[GMS83]   J. D. Gunton, M. San Miguel, and Paramdeep S. Sahni. The Dynamics of First-order Phase Transitions. In C. Domb and J. L. Lebowitz, editors, *Phase Transitions and Critical Phenomena*, page 267. Academic Press, 1983.

[Gol89]   A. S. Goldhaber. Collapse of a 'Global Monopole'. *Phys. Rev. Lett.*, 63:2158, 1989.

[GSG75]   J. A. Geurst, A. M. J. Spruijt, and C. J. Gerritsma. Dynamics of S=$\frac{1}{2}$ Disclinations in Twisted Nematics. *Le Journal de Physique*, 36:653, 1975.

[GSM87]   B. D. Gaulin, S. Spooner, and Y. Morii. Kinetics of Phase Separation in $Mn_{0.67}Cu_{0.33}$. *Phys. Rev. Lett.*, 59:668, August 1987.

[GST90]   A. Gooding, D. Spergel, and N. Turok. The Formation of Galaxies and Quasars in a Texture Seeded CDM Cosmogony. *Princeton preprint POP-367*, 1990.

[GW87]   Rafael C. Gonzalez and Paul Wintz. *Digital Image Processing*. Addison-Wesley, 1987.

[HH77]   P. C. Hohenberg and B. I. Halperin. Theory of dynamic critical phenomena. *Rev. Mod. Phys.*, 49:435, 1977.

[Hus86]   D. A. Huse. Corrections to late-stage behavior in spinodal decomposition: Lifshitz-Slyozov scaling and Monte Carlo Simulations. *Phys. Rev. B*, 34:7845, 1986.

[Kah73]   Frederic J. Kahn. Orientation of liquid crystals by surface coupling agents. *Appl. Phys. Lett.*, 22:386, 1973.

[Kaw85]   K. Kawasaki. Defect-phase-dynamics approach to statistical domain-growth ploblem of clock models. *Phys. Rev. A*, 31:3880, June 1985.

[Kib76]   T.W.B. Kibble. Topology of cosmic domains and strings. *J. Phys. A*, 9:1387, 1976.

[Kib80]   T. W. B. Kibble. Some Implications of a Cosmological Phase Transition. *Phys. Reports*, 67:183, 1980.

[KL88]   M. V. Kurik and O.D. Lavrentovich. Defects in Liquid Crystals: Homotopy Theory and Experimental Studies. *Sov. Phys. Usp.*, 31:196, 1988.

[Kle83]   M. Kleman. *Points, Lines, and Walls, in liquid crystals, magnetic systems, and various ordered media*. John Wiley and Sons Ltd., 1983.

[Kle90]   W. Klein. Fractal and Multifractals in Early-Stage Spinodal Decomposition and Continuous Ordering. *Phys. Rev. Lett.*, 65:1462, 1990.

[KM77]   P. P. Karat and N. V. Madhusudana. Elasticity and Orientational Order in Some 4'-n-Alkyl-4-Cyanobiphenyls: Part II. *Mol. Cryst. Liq. Cryst.*, 40:239–245, 1977.

[KMT77]   M. Kléman, L. Michel, and G. Toulouse. Classification of Topologically Stable Defects in Ordered Media. *Le Journal de Physique*, 38:L–195, May 1977.

[KRS85]   V. Kuzmin, V. Rubakov, and M. Shaposhnikov. *Phys. Lett. B*, 155:36, 1985.

[Lif82]   I. M. Lifshitz. Kinetics of Ordering During Second-Order Phase Transitions. *Soviet Physics JETP*, 15:939, November 1982.

[LR88]   O. D. Lavrentovich and S. S. Rozhkov. Strings with boojums at their ends: topological defects of a new type in nematic liquid crystals. *JETP Lett.*, 47:255, 1988.

[LS61]   I. M. Lifshitz and V. V. Slyosov. *J. Phys. Chem. Solids*, 19:35, 1961.

[Mer79]   N. D. Mermin. The topological theory of defects in ordered media. *Rev. of Mod. Physics*, 51(3):591, July 1979.

[MG90]   M. Mondello and N. Goldenfeld. Scaling and vortex dynamics after the quench of a system with continuous symmetry. *University of Illinois at Urbana Champagne Preprint*, 1990.

[Mic80]   Louis Michel. Symmetry defects and broken symmetry. Configurations Hidden Symmetry. *Rev. of Mod. Physics*, 52(3):617, July 1980.

[MMR90]   K. J. M. Moriarty, E. Meyers, and C. Rebbi. The Dynamical Interactions of Cosmic Strings. *J. Computational Physics*, 88:467, 1990.

[MV87]   G. F. Mazenko and O. T. Valls. Spinodal decomposition for Langevin Equations. *Phys. Rev. Lett.*, 59:680, 1987.

[MYT+77]   A. Miyaji, M. Yamaguchi, A. Toda, H. Mada, and S. Kobayashi. Control and Elimination of Disclinations in Twisted Nematic Liquid-Crystal Displays. *IEEE Trans. on Electron Devices*, 24(7):811, July 1977.

[MZ85]   G. F. Mazenko and M. Zannetti. Instability, spinodal decomposition, and nucleation in a system with continuous symmety. *Phys. Rev. B*, 32:4565, 1985.

[NN89]   H. Nishimori and T. Nukii. A Computational Study of Defect Dynamics of a 3-Dimensional Quenched Complex Field. *J. Phys. Soc. of Japan*, 58(2):563, February 1989.

[NOI87]   T. Nagaya, H. Orihara, and Y. Ishibashi. Collective Motion of an Assembly of Disclinations in the Non-Orthogonally Twisted Nematics Quenched below the Clearing Point. *J. Phys. Soc. Japan*, 56(9):3086, September 1987.

[NS71]   J. Nehring and A. Saupe. On the elastic theory of Uniaxial Liquid Crystals. *J. Chem. Phys.*, 54:337, 1971.

[OI86]   H. Orihara and Y. Ishibashi. Dynamics of Disclinations in Twisted Nematics Quenched below the Clearing Point. *J. Phys. Soc. Japan*, 55(7):2151, July 1986.

[Ost81]   S. Ostlund. Interactions between topological point singularities. *Phys. Rev. B*, 24:485, 1981.

[PFTV86]   Press, Flannery, Teukolsky, and Vetterling. *Numerical Recipes, the Art of Scientific Computing*. Cambridge University Press, 1986.

[RED88]   T. M. Rogers, K.R. Elder, and R. C. Desai. Numerical study of the late stages of spinodal decomposition. *Phys. Rev. B*, 37:9638, 1988.

[Rey90]   A. D. Rey. Defect controlled dynamics of nematic liquids. *Liquid Crystals*, 1:315, 1990.

[Sha77]   R. Shanker. Applications of topology to the study of ordered systems. *J. Phys. (Paris)*, 38:1405, 1977.

[Sha87]   M. Shaposhnikov. Baryon asymmetry of the universe in standard electroweak theory. *Nuc. Phys. B*, 287:757, 1987.

[Sha88]   M. Shaposhnikov. *Nuc. Phys. B*, 299:797, 1988.

[Ste51]   N. E. Steenrod. *The Topology of Fibre Bundles*. Princeton University Press, 1951.

[TCG88]   R. Toral, A. Chakraburti, and J. Gunton. Numerical Study of the Cahn-Hilliard Equation in Three Dimensions. *Phys. Rev. Lett.*, 60:2311, 1988.

[TH87]   H. Toyoki and K. Honda. Ordering Dynamics of a Deeply Quenched Complex Field. *Progress of Theoretical Physics*, 78:237, August 1987.

[Toy90]   H. Toyoki. Pair annihilation of pointlike topological defects in the ordering process of quenched systems. *Phys. Rev. A*, 42:911, 1990.

[TS90]   N. Turok and D. Spergel. Global Texture and the Microwave Background. *Phys. Rev. Lett.*, 64:2736, 1990.

[Tur89]   N. Turok. Global Texture as the Origin of Cosmic Structure. *Phys. Rev. Lett.*, 63(24):2625, December 1989.

[TZ90]   N. Turok and J. Zadrozny. *Phys. Rev. Lett.*, 1990. to appear.

[VdJ88]   G. Vertogen and W.H. de Jeu. *Thermotropic Liquid Crystals*. Springer-Verlag, 1988.

[Vil81]   A. Vilenkin. Cosmic Strings. *Phys. Rev. D*, 24:2082, 1981.

[Vil85]   A. Vilenkin. Cosmic Strings and Domain Walls. *Phys. Rep.*, 121:263, 1985.

[Voo85]   P. W. Voorhees. The theory of Ostwald Ripening. *J. Stat. Phys*, 38:231, 1985.

[WC88]   Shin-Tson Wu and R. J. Cox. Optical and electro-optic properties of cyanotoluanes and syanostilbenes: Potential infrared crystals. *J. App. Phys.*, 64:821, 1988.

[WCK73]   C. E. Williams, P. E. Cladis, and M. Kleman. Screw Disclinations in Nematic Simples with Cylindrical Symmetry. *Mol. Cryst. Liquid Cryst.*, 21:355, 1973.

[WPC72a]   C. Williams, P. Pierański, and P. E. Cladis. Nonsingular S+1 Screw Disclination Lines in Nematics. *Phys. Rev. Lett.*, 29:90, 1972.

[WPC72b]   C. Williams, P. Pierański, and P. E. Cladis. Nonsingular S=+1 Screw Disclination Lines in Nematics. *Phys. Rev. Lett.*, 29(2):90, July 1972.

[WZ89]   Y-S. Wu and A. Zee. *Nuc. Phys. B*, 324:623, 1989.

[Zur85]   W. H. Zurek. Cosmological experiments in superfluid helium? *Nature*, 317:505, October 1985.

Index

114

Appendix A

Images and Photographs

This Appendix contains a collection of images and photographs of the various systems we studied.

A.1   The 2D SLC: Simulated Schlieren Images
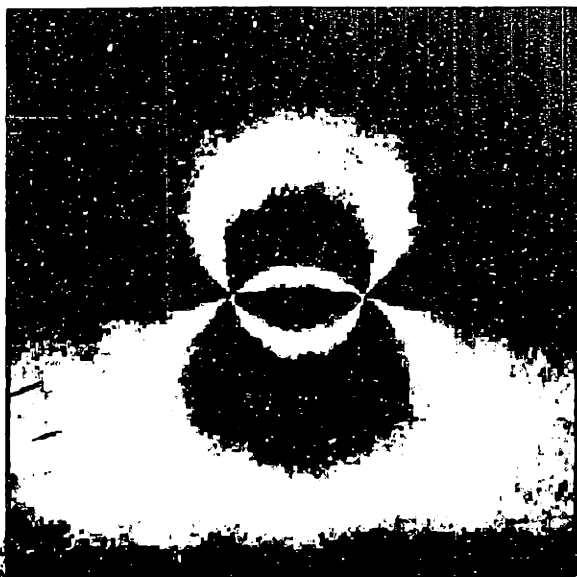
t=4000 iterations   t=8000 iterations
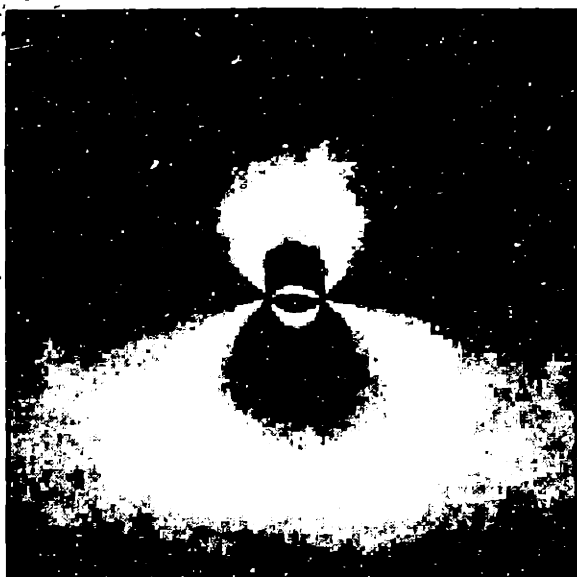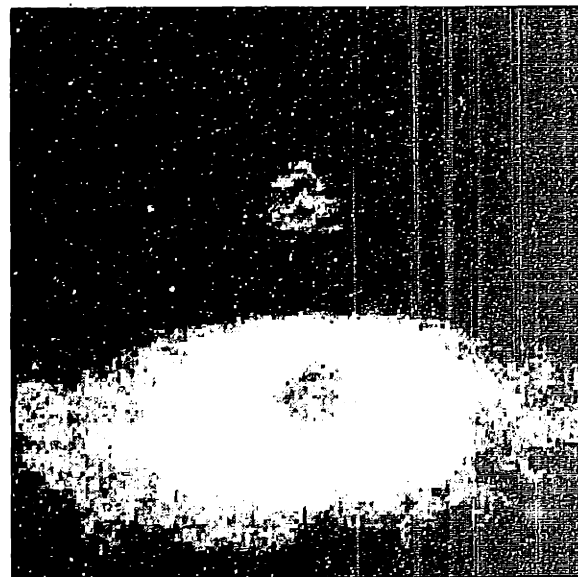
t=10000 iterations   t=12000 iterations

lsim 2D-SLC simulation. File: semectic/monopole/monop.ps, generated from monop1.cmd simulation (128x128) [Wed Jul 11 17:14:12 1990]

Figure A-1: A sequence of four simulated schlieren images of a SLC thin film, showing monopole coalesence. The images are of a 128×128 sized system.
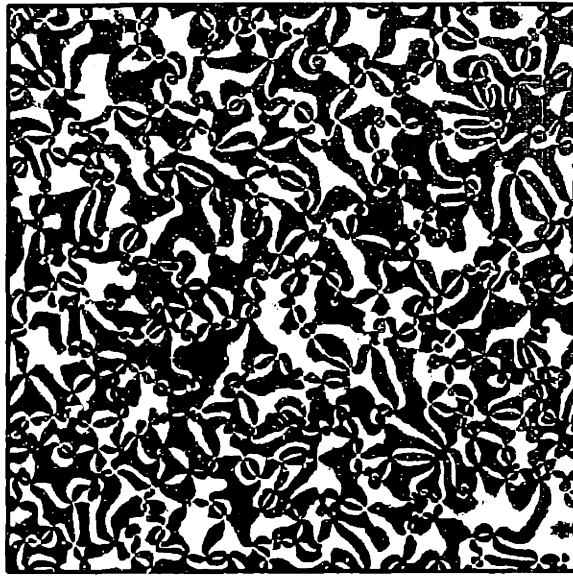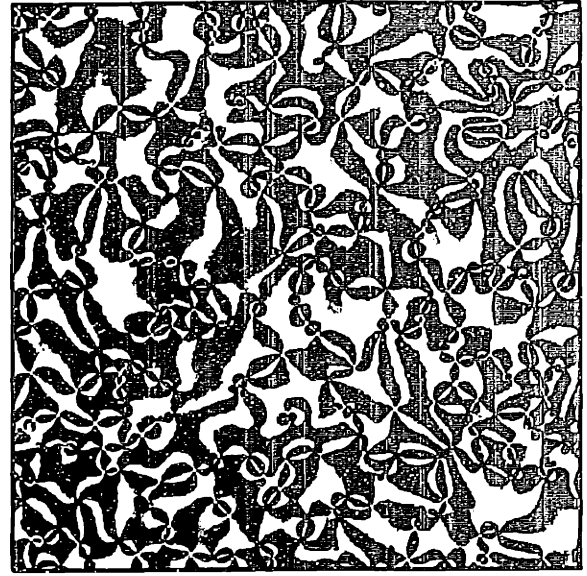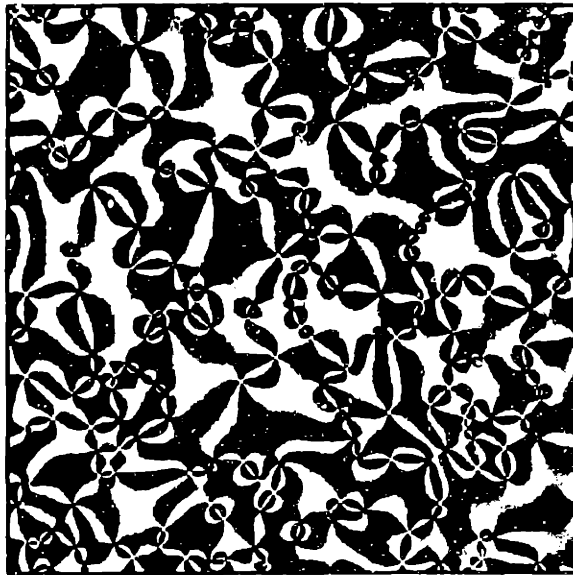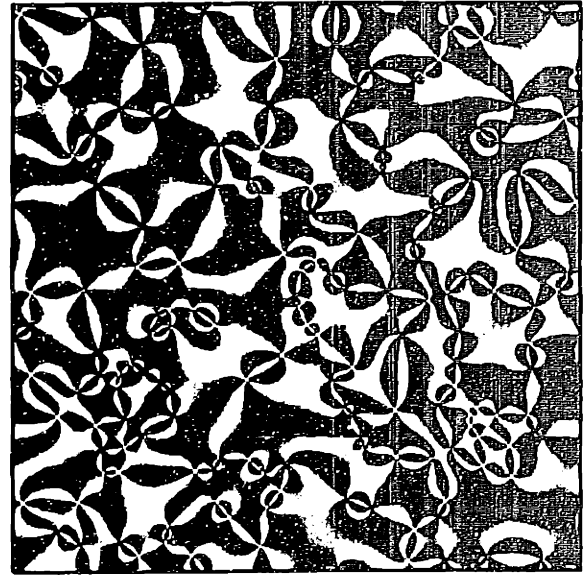
A2

t=248

t=504

t=1016

t=2040

Figure A-2: Numerical simulation of a quench-induced isotropic→smectic phase transition in a 256×256 sized 2D SLC system. Times are given in number of iterations. The evolution parameters are as follows: Langevin noise amplitude $\Gamma_{LA} = 0.001$, viscous coefficient $\gamma = 1$, potential depth $\lambda = 4$, elastic constants $k_1 = k_3 = 0.1$, time stepsize $\Delta t = 0.05$, and gridsize $a = 1$.

A.2 The 2D NLC: Director Fields and Schliren Images
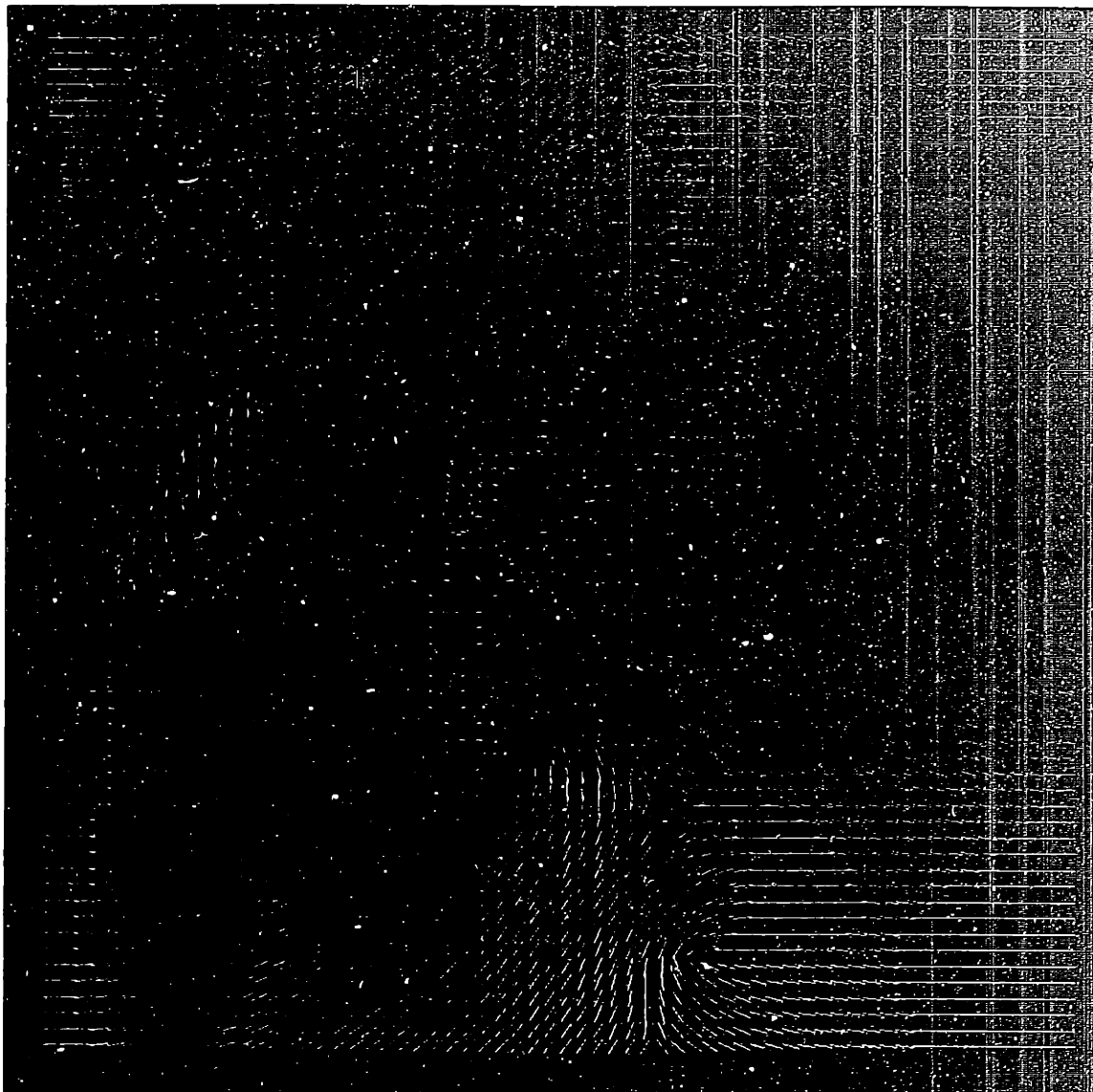
Figure A-3: Picture of the director field of a 64×64 2D NLC system showing three pairs of $\pm\frac{1}{2}$ monopoles in the process of annihilating with each other.
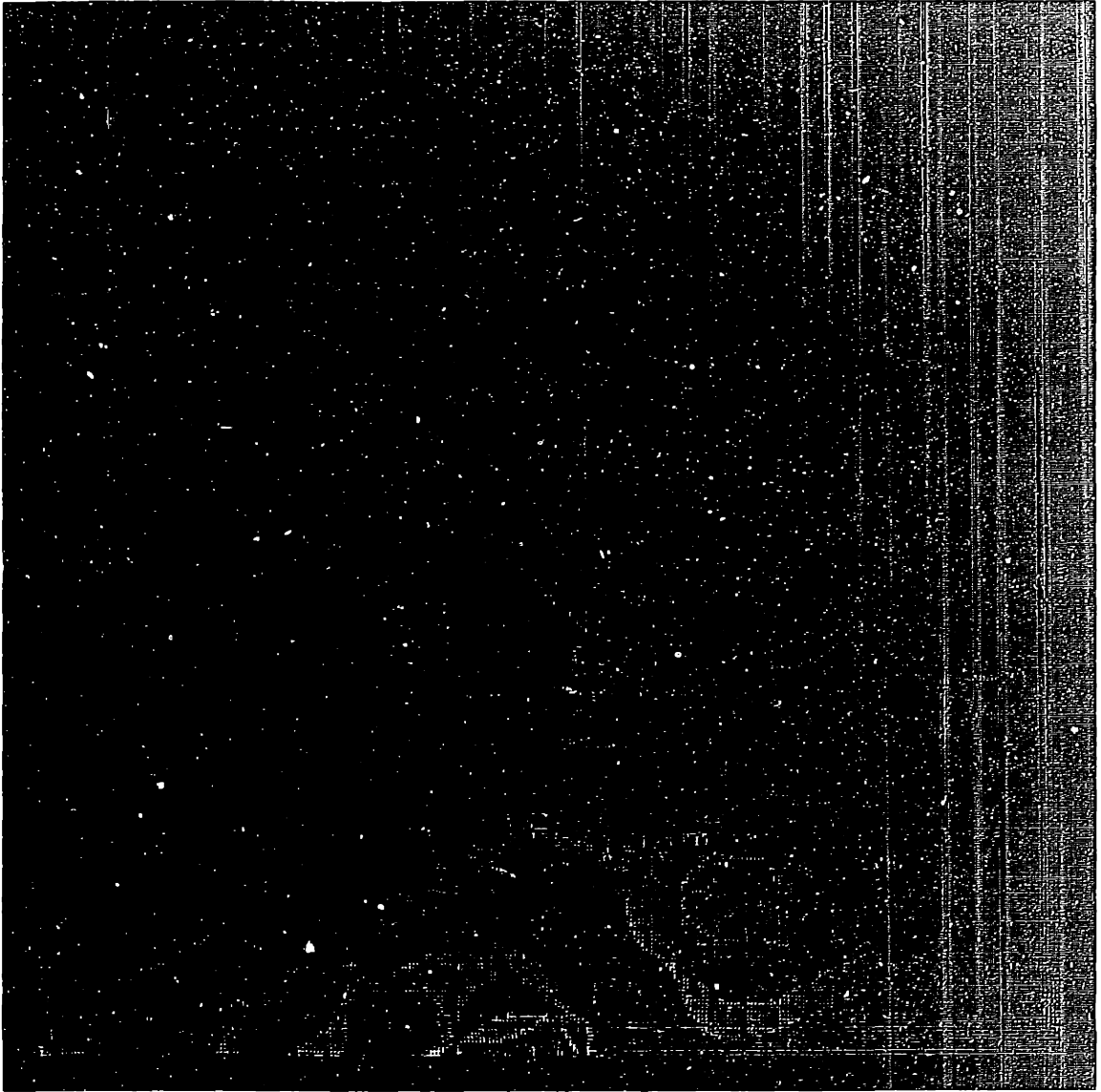
Figure A-4: Director field of a 2D NLC evolved from a random initial configuration. Note the absence of ±1 monopoles.
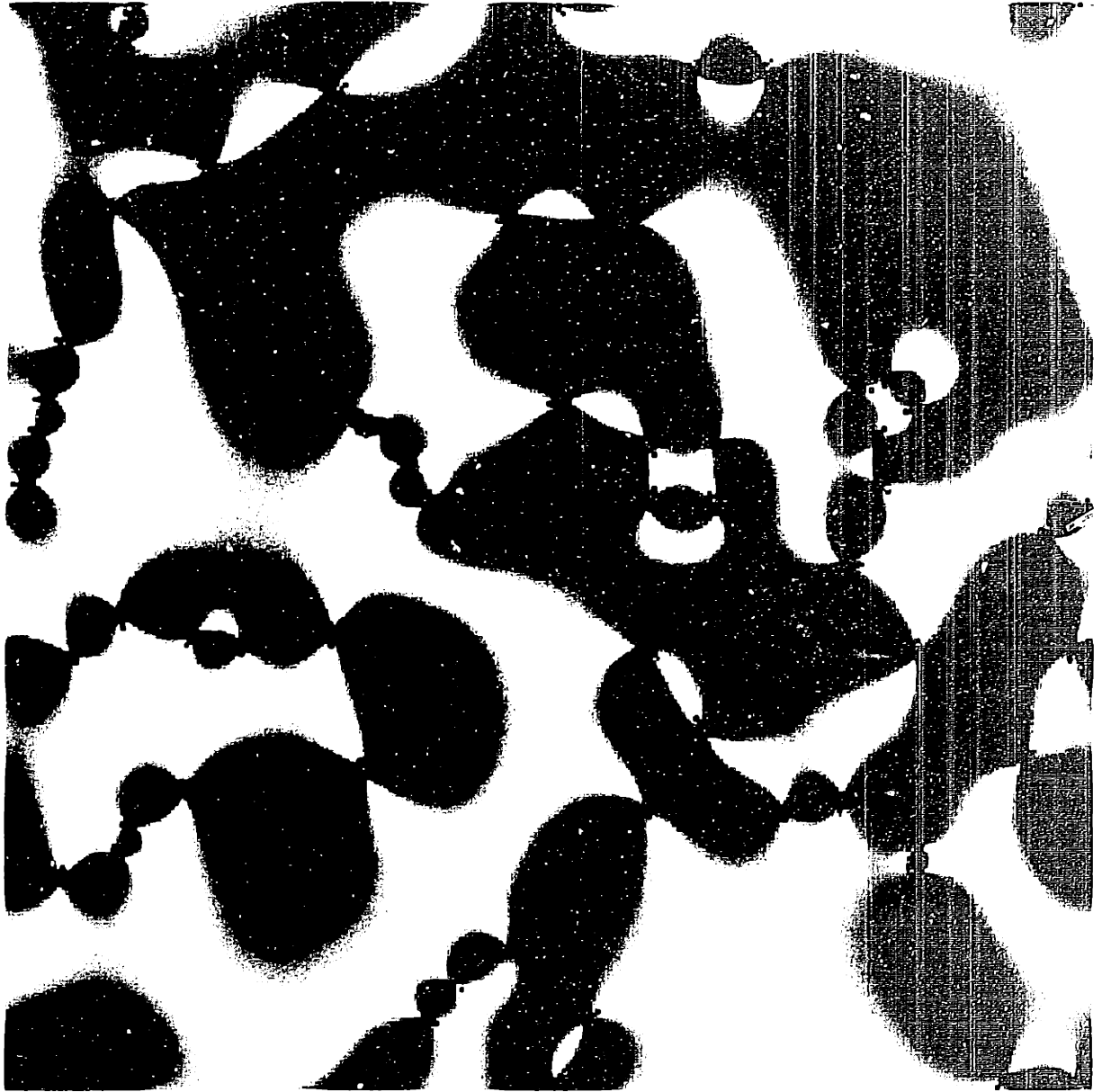
Figure A-5: Crossed polarizer image of the director field of Figure A-4.
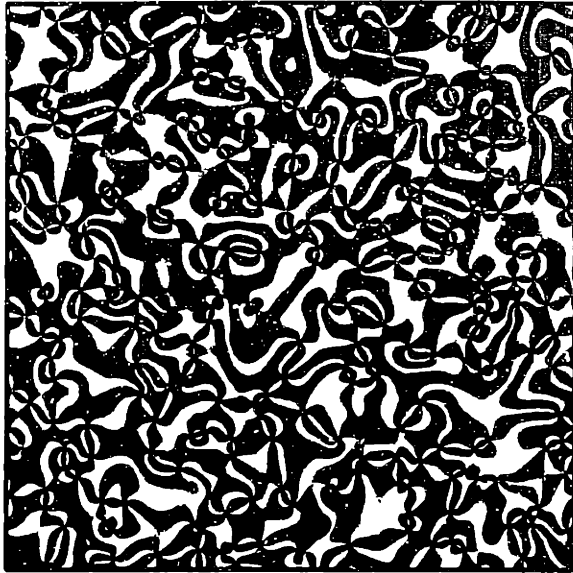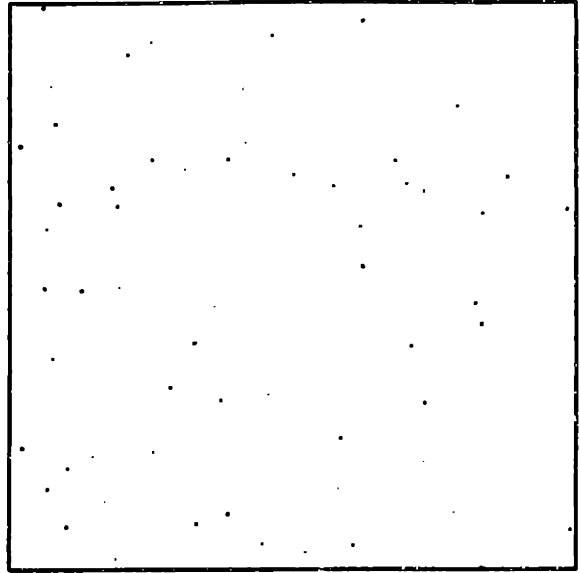
Crossed polarizer image   **Splay energy image**
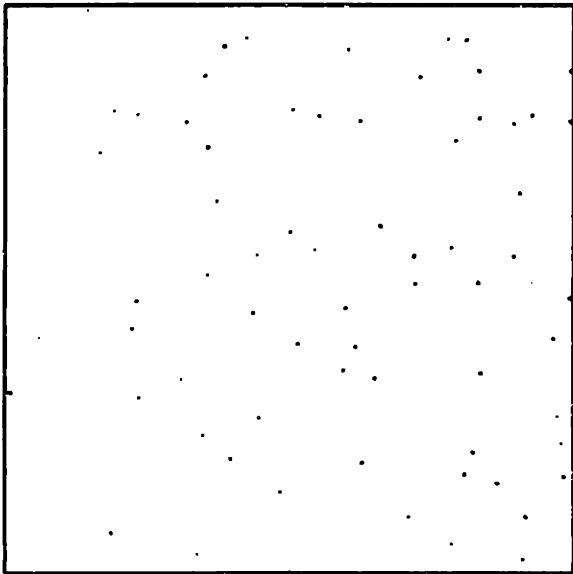
Bend energy image   **Lambda potential energy image**
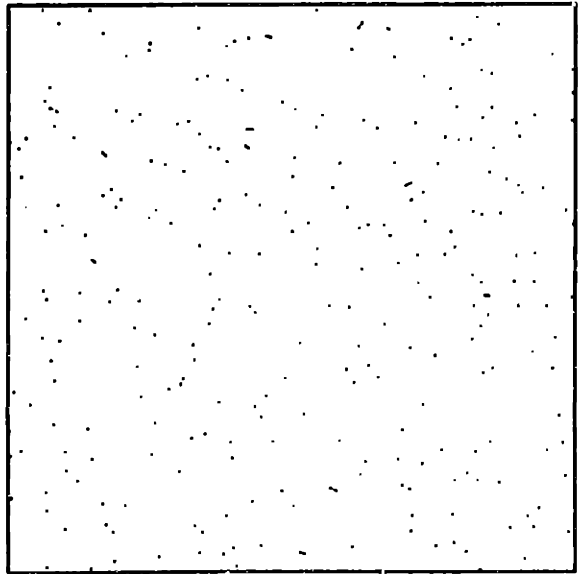
Figure A-6: Four images showing various features of a densely populated 2D-SLC system. The Schlieren image is a simple function of the director field itself, while the bend, splay, and lambda energy pictures indicate the points in the system which are high in the respective energy components. Note their correspondence with the various monopole locations.

A7

A.3 The 3D NLC: Director fields and Isometric Energy Surfaces
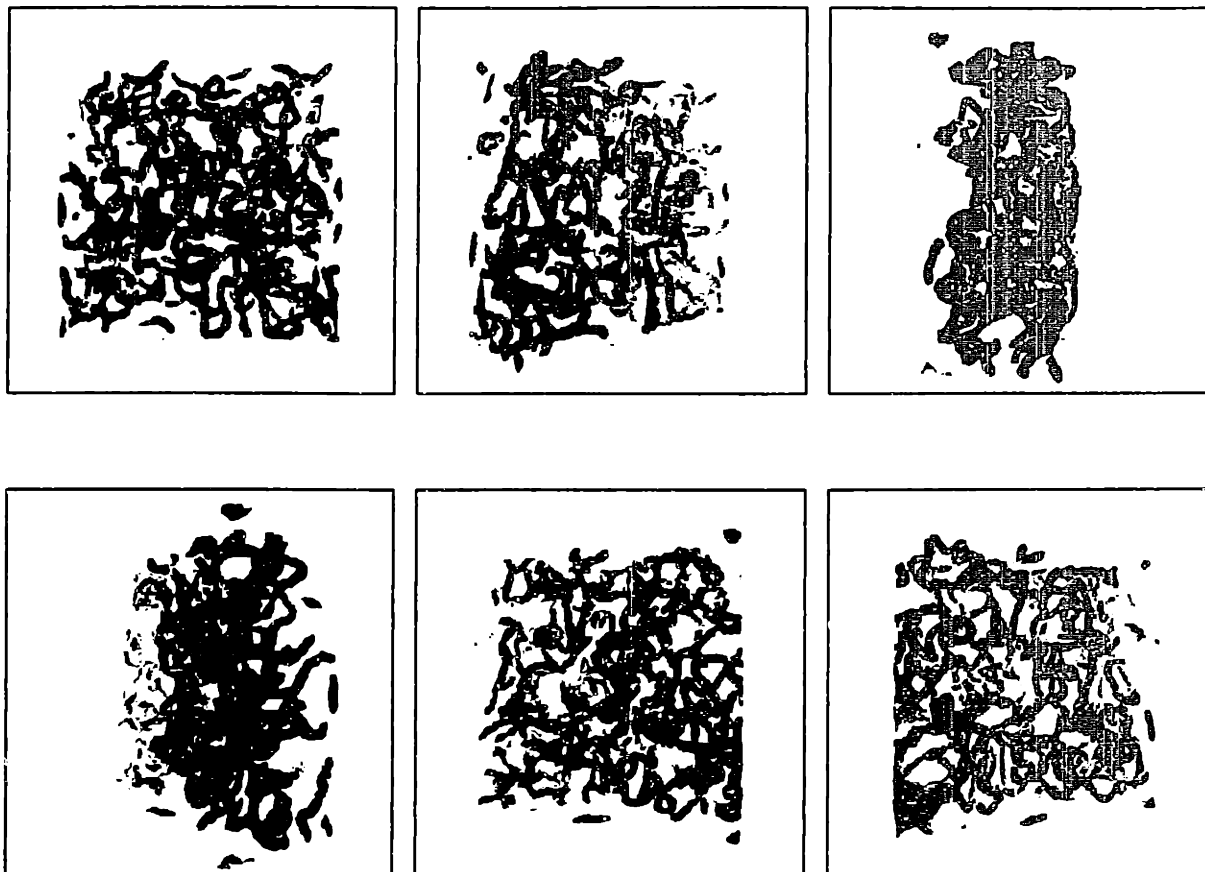
Figure A-7: Simulation results showing the tangle of strings generated by quench of a 3D NLC into the nematic phase. The six frames show the same defect tangle from different perspectives. Surfaces of constant energy density were volume-rendered using NCSA X-DataSlice, with data generated from our SO(3) tensor model 3D NLC simulaton running on a Cray X-MP. See Figure A-22 for a full-scale rendition of the tangle.
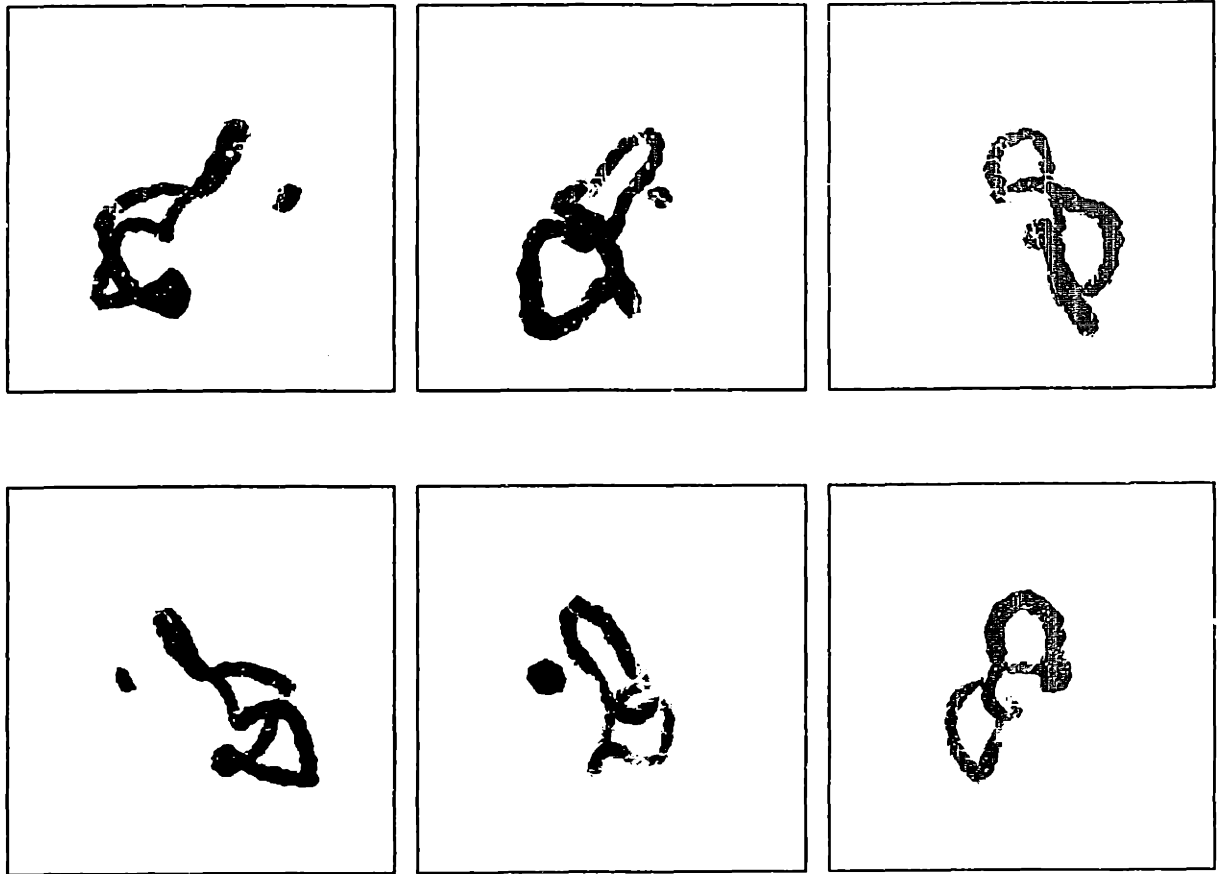
A8

Figure A-8: Simulation results showing two $\pm \frac{1}{2}$ loops, one collapsed to near extintion, generated by quench of a 3D NLC into the nematic phase.
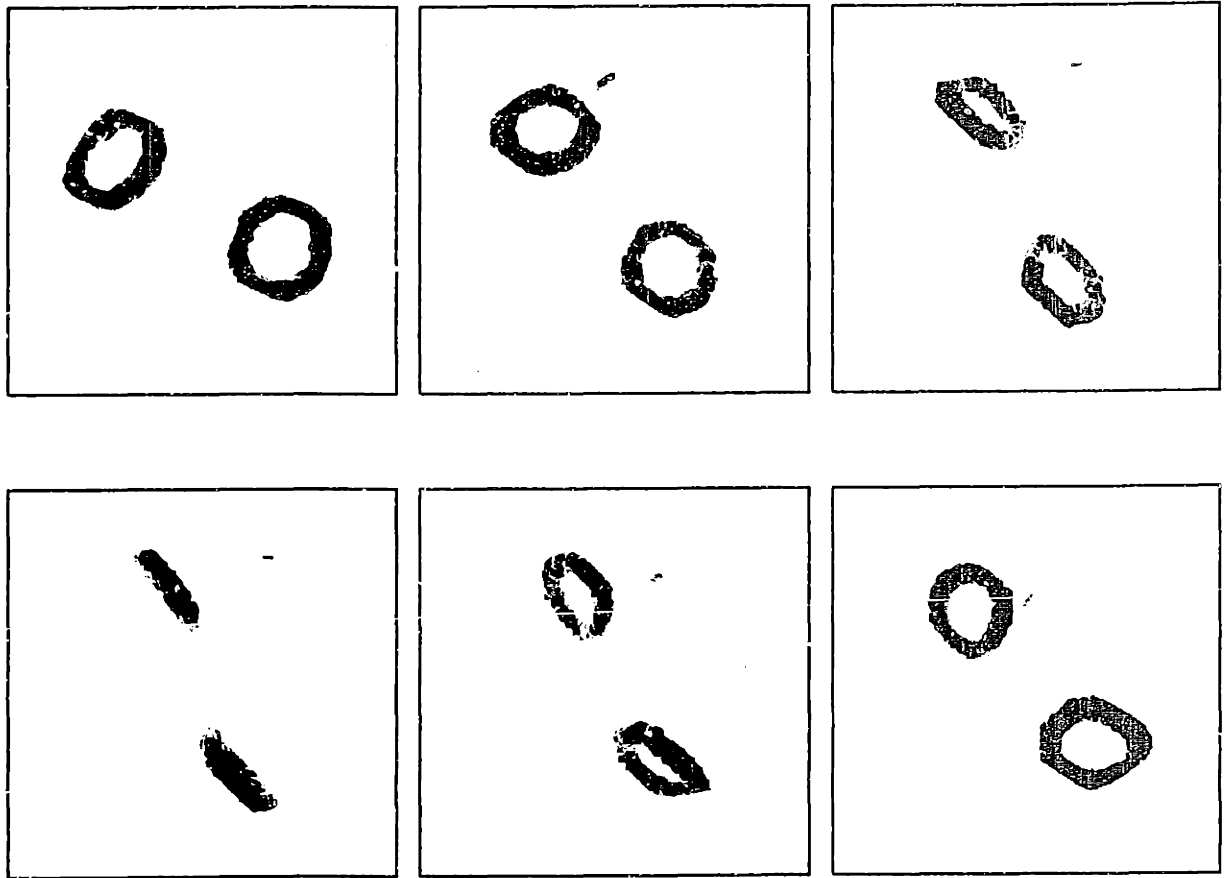
Figure A-9: Two $\pm\frac{1}{2}$ loops, created by the decomposition of an unescaped $+1$ string.

A10
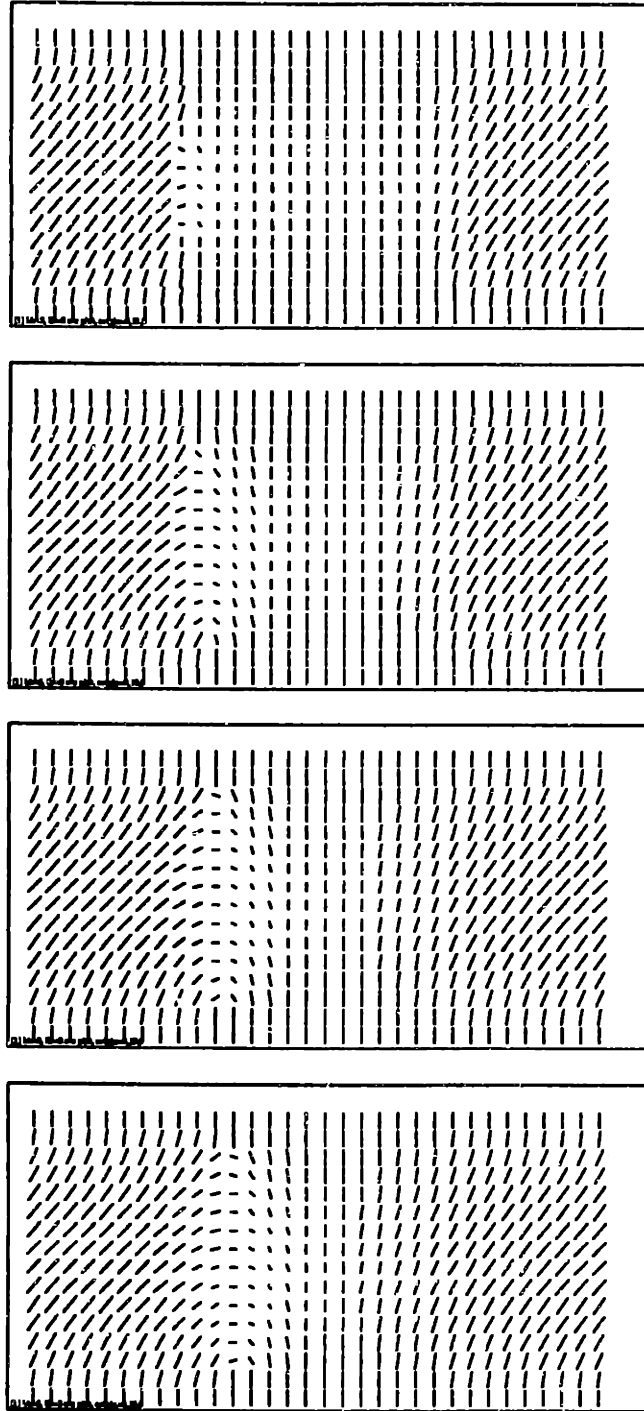
Figure A-10: Cartesian crossection rod pictures of Figure A-9 The x-z plane of the $32\times32\times16$ sized system is shown at four levels (top, y=28; middle, y=29, y=30; bottom, y=31). The length and orientation of the rods are given by their n_x and n_z components. Half of one loop can be seen.

A11
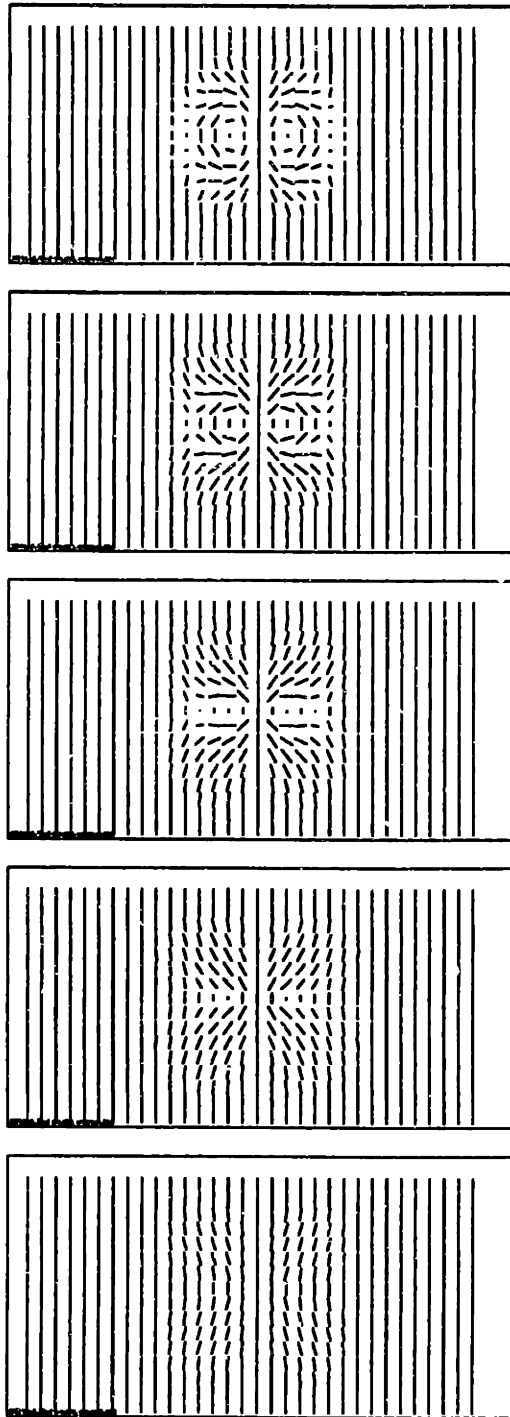
Figure A-11: $x - z$ plane crossection of a texture with its axis along $\hat{z}$. The sequence shows the texture as it collapses, at approximately 1000 iteration intervals.

A.4   The Thin Film NLC
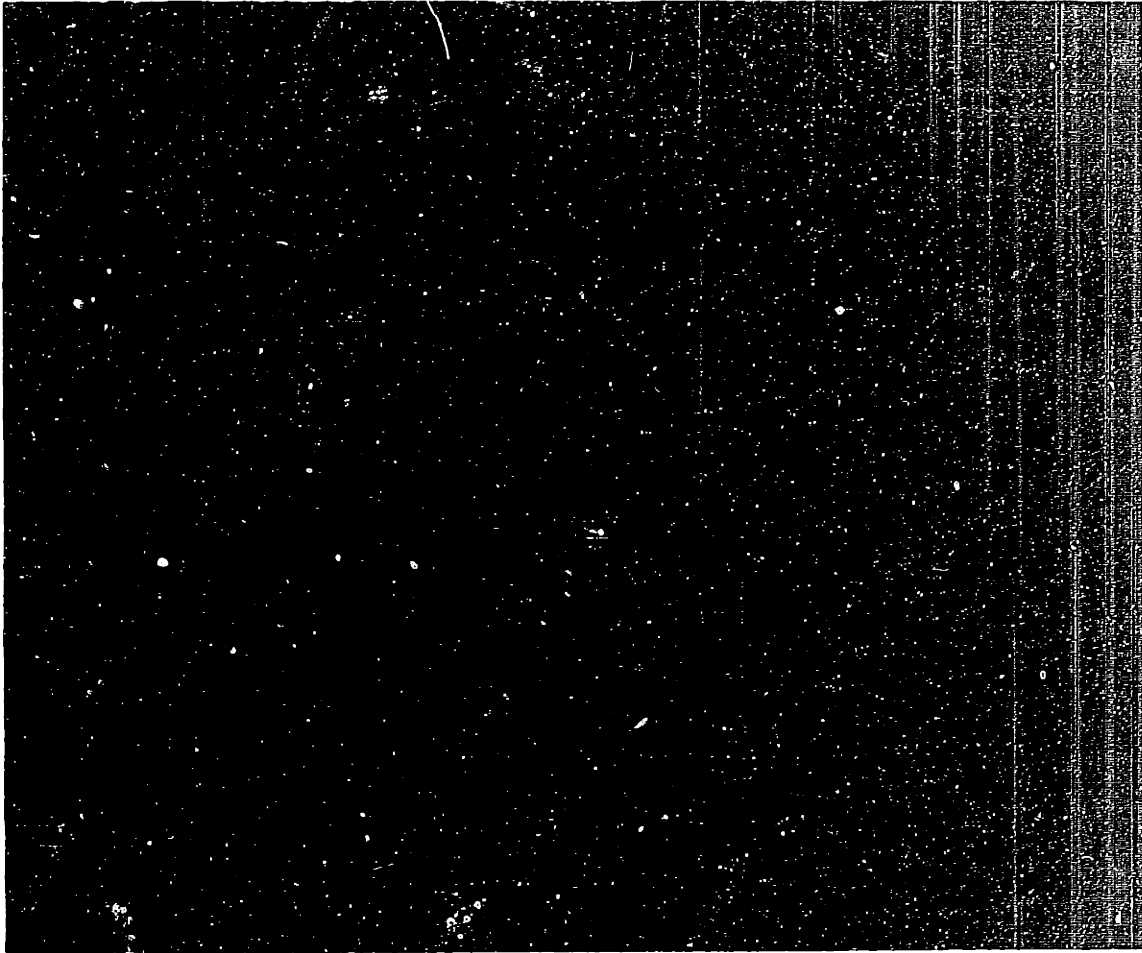
Figure A-12: Photograph of the defect tangle in a thin film of freely suspended nematic liquid crystal after a temperature quench. The dark, sharp lines in the picture are type-$\frac{1}{2}$ strings. In the top-center of the picture, is a diffuse but visible type-1 string with three monopoles, which appear as black spots on the string. Below that is a type-$\frac{1}{2}$ string attached in two places to a type-1 string which is also supporting a monopole. Various other features in the photograph include boojums, which are defects which are attached to the surface of the film and appear as lines which terminate in dark blobs, and many instances of type-1 strings cutting across horseshoe shaped type $\frac{1}{2}$ strings. The picture is about 790 μm wide.

A.5 Pressure Cell Data Images
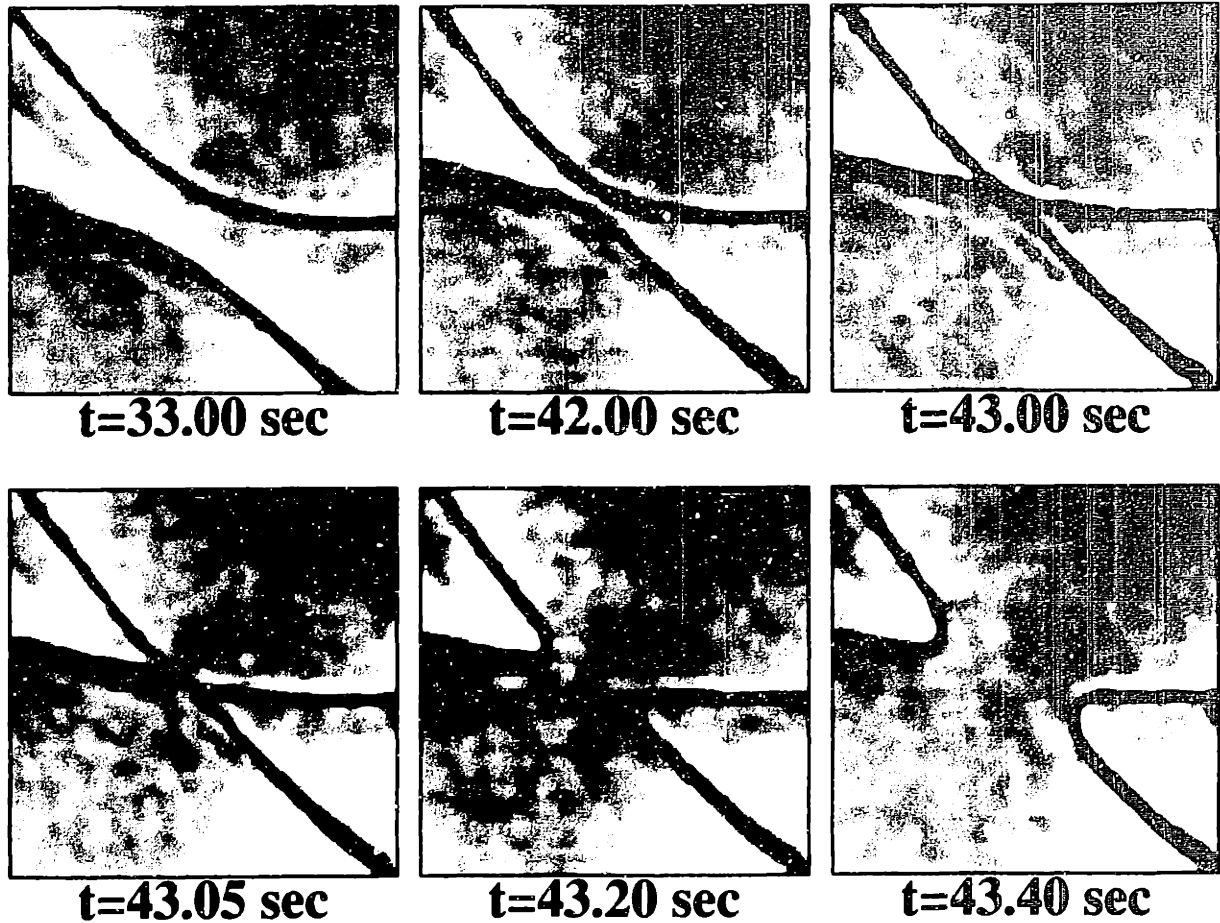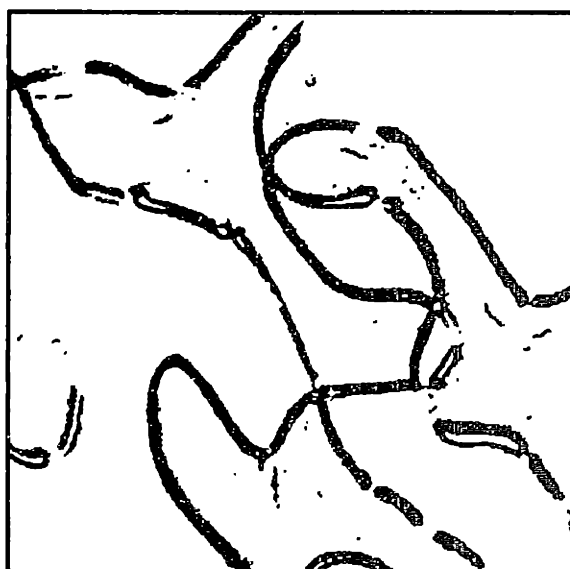

t=33.00 sec t=42.00 sec t=43.00 sec

t=43.05 sec t=43.20 sec t=43.40 sec

K15 Liquid Crystal.   File: ic/ic1-m34.ps, generated from input ic/ic1-m34.raw (192x156) [Sat Oct 13 21:07:02 1990]

Figure A-13: String intercommutation sequence, showing two type $\frac{1}{2}$ strings crossing each other and reconnecting the other way. Each picture is about 140 μm wide. Note that the two strings lie almost in the same plane - the intercommutation occurs after the strings move toward each other under their mutual attraction.
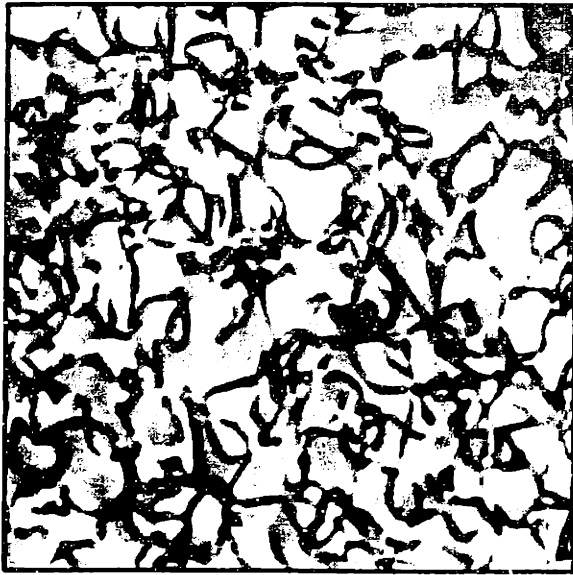
t=1.0 sec

t=1.7 sec

t=2.9 sec

t=4.8 sec

K15 Liquid Crystal.   File: ic/ic1-m34.ps. generated from input ic/ic1-m34.raw (192x156) [Sat Oct 13 21:07:02 1990]

Figure A-14: A coarsening sequence showing the strings visible in our 230 μm thick pressure cell containing K15 nematic liquid crystal, at t=1.0, 1.7, 2.9, and 4.8 seconds after a pressure jump of ΔP = 4.7 MPa from an initially isotropic state in equilibrium at approximately 37 °C and 3.6 MPa. The evolution of the string network shows self-similar or "scaling" behavior. Each picture is about 360 μm wide.
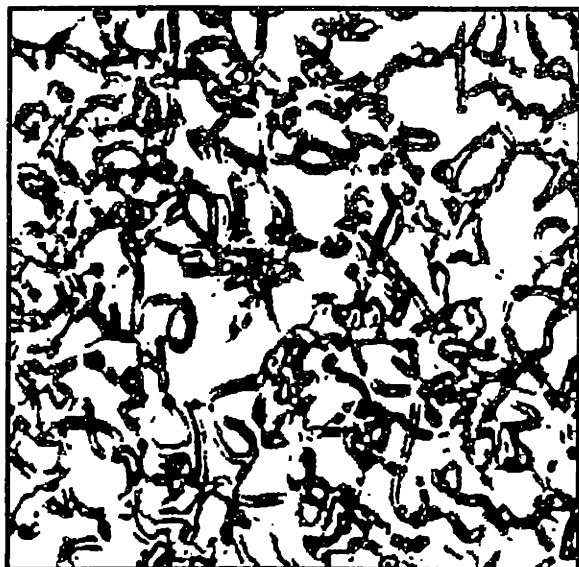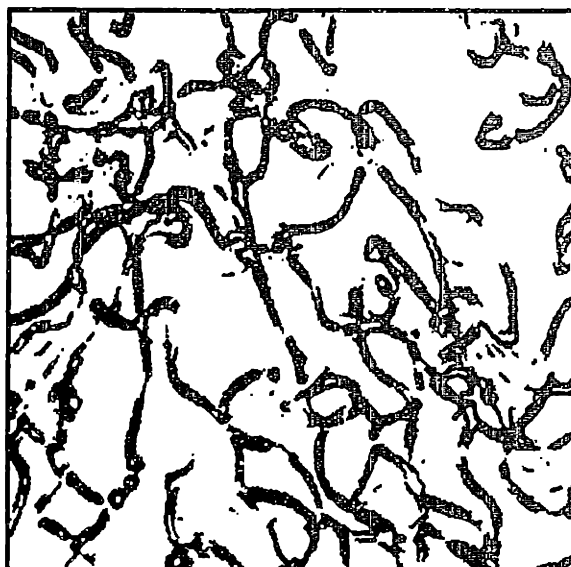
A15

t=1.0 sec

t=1.7 sec

t=2.9 sec

t=4.8 sec

K15 Liquid Crystal, File: ic/icl-m34.ps, generated from input ic/icl-m34.raw (192x156) [Sat Oct 13 21:07:02 1990]

Figure A-15: Processed versions of the data in Figure A-14. The images were cleaned using 3×3 median filtering, adaptive background subtraction, sobel gradient calculation, and morphological dilation/erosion.
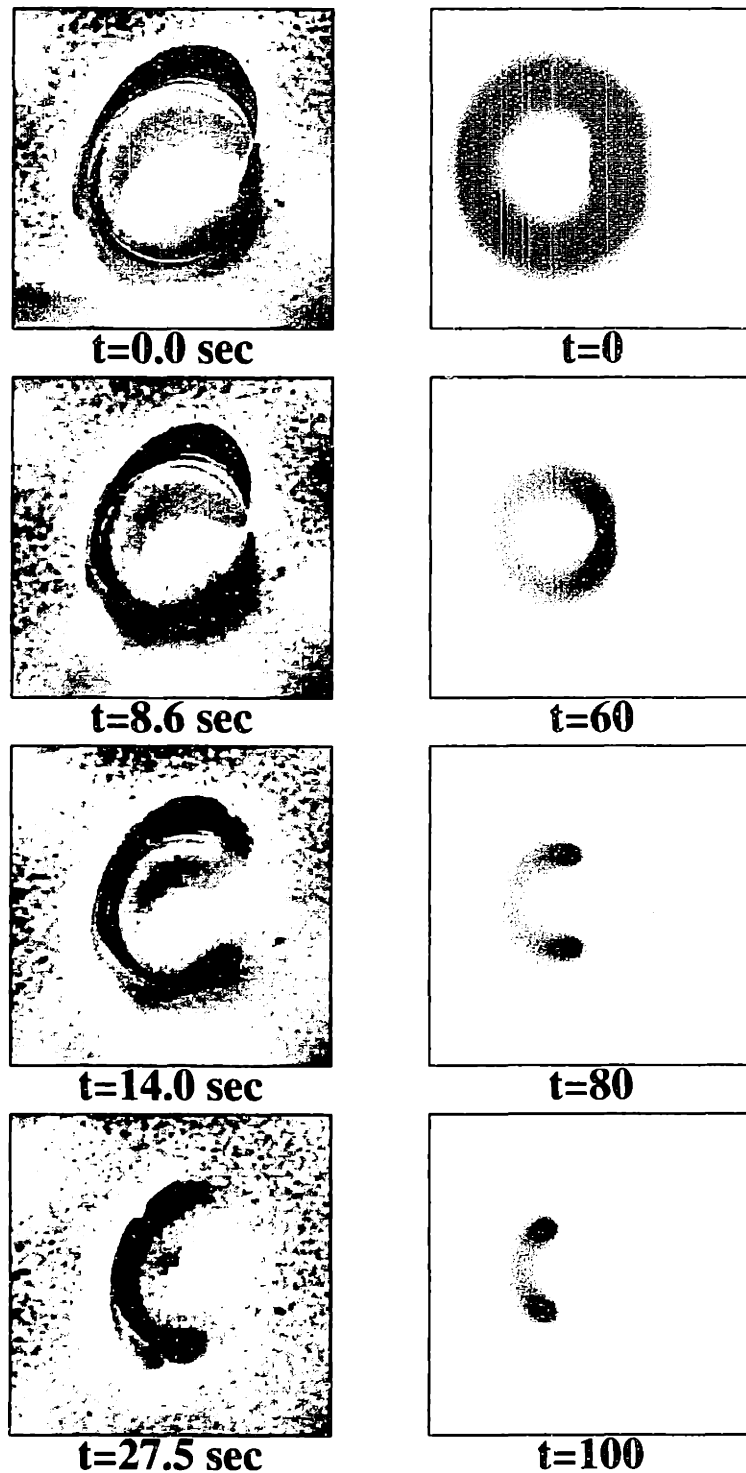
Figure A-16: A time sequence showing the evolution of a π_3 "texture" in a freely suspended thin film of nematic liquid crystal (left column), and as simulated numerically (right column). The texture breaks at one point to form a monopole-antimonopole pair which then move around the ring to annihilate on the far side. Each frame is about 260 μm wide.

t=5.9 sec   t=6.8 sec   t=7.1 sec

t=8.3 sec   t=9.1 sec   t=10.6 sec
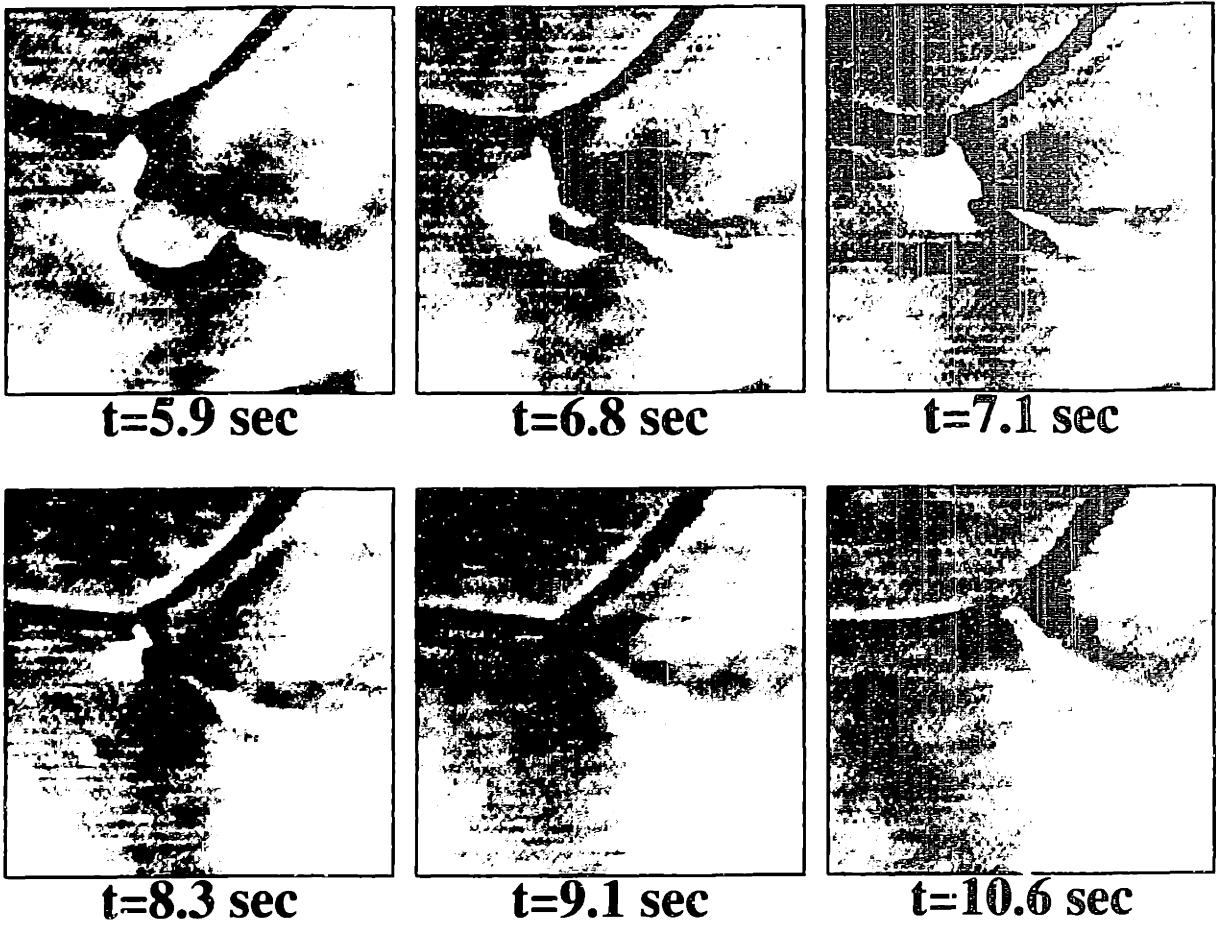
K15 Liquid Crystal.   File: mlc98-six.ps. generated from input mlc98.raw (138x132) [Fri Nov 16 17:06:58 1990]

Figure A-17: Creation of a monopole from the collapse of a $\pm\frac{1}{2}$ loop. The figure shows actual pictures recorded from one pressure jump of the set of ten in Run 9.
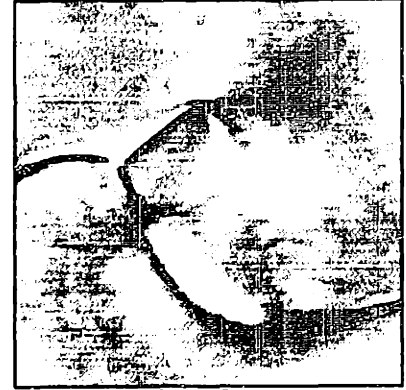
t=9.5 sec t=10.5 sec t=11.2 sec
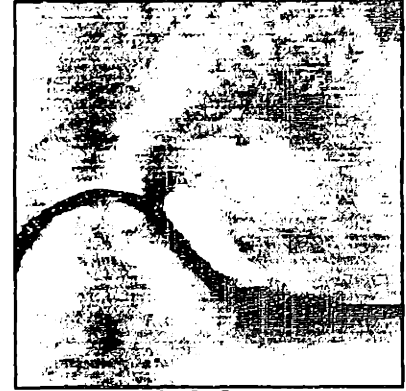
t=12.0 sec t=14.5 sec t=16.0 sec

K15 Liquid Crystal.   File: mhist-six.ps. generated from input monop/mhist.ps (256x256) [Thu Nov 15 19:42:29 1990]

Figure A-18: Another monopole creation event, from the collapse of a $\pm\frac{1}{2}$ loop.

A19

t=3.75 sec

t=3.90 sec

t=4.13 sec
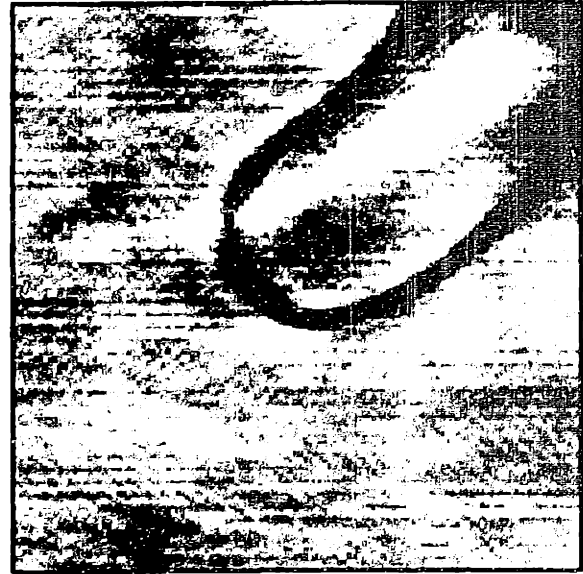
t=4.40 sec

Figure A-19: Decay of a ± 1 string connecting two parts of the same $\pm \frac{1}{2}$ string. This is a very common event. We denote it as event code 8 in our classification (Table 5.2).

t=1.2 sec   t=1.7 sec   t=2.3 sec

t=3.0 sec   t=4.0 sec   t=4.6 sec
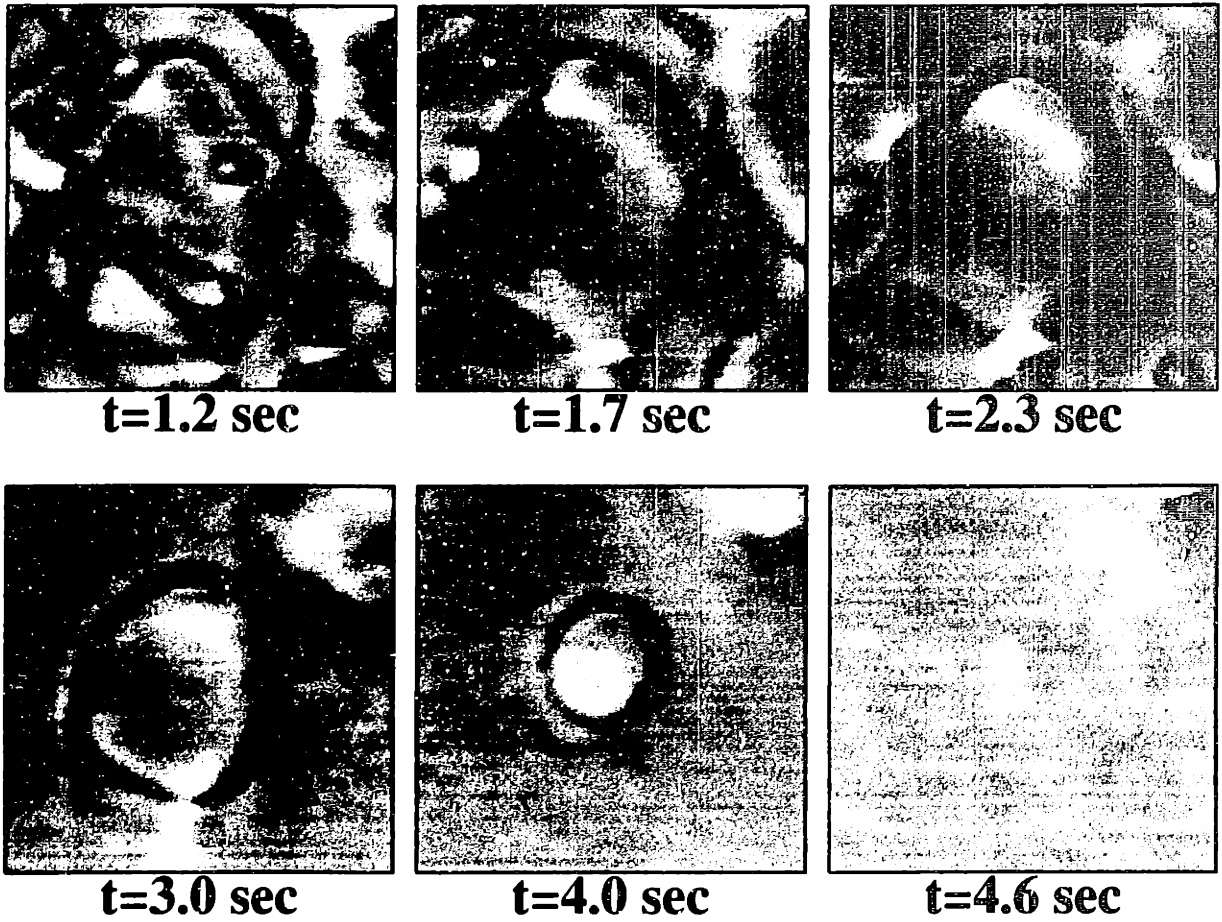
K15 Liquid Crystal.   File: loop-history/loop-six.ps. generated from input loop.raw (128x128) [Fri Nov 16 16:20:51 1990]

Figure A-20: Observation of the creation of a loop from various defect events. The loop subsequently collapses.

A.6 Additional Images
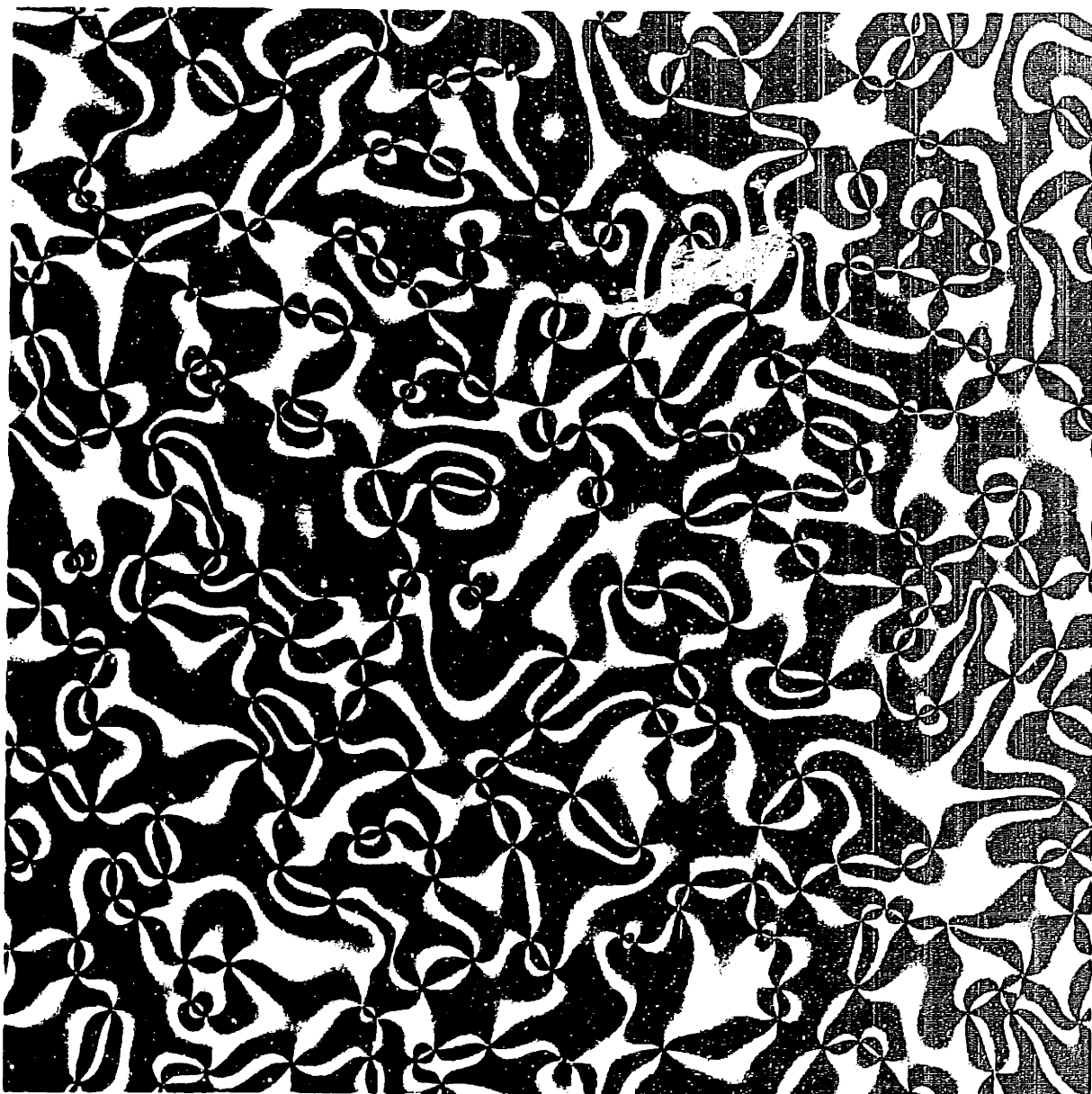
Figure A-21: The Schliren image of a 512×512 sized 2D SLC system, showing numerous monopoles.

Figure A-22: The defect tangle created by a 3D NLC simulation starting from a random configuration (see Figure A-7).

Appendix B

Defect Interaction Event Branching Ratios

This Appendix contains data tabulating our observations of the branching ratios of various defect interaction events. Refer to section 5.5 for a discussion of the data and the nomenclature used in the tables.
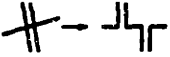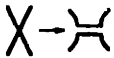
Code	Event	Probability (%)
4		50
17		50

Table B.1: Branching ratios of T-intersection creation ($\Delta n_T = +1$) events. A total of 4 T-intersection creation events were observed.
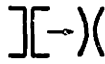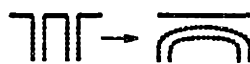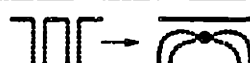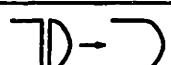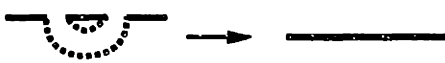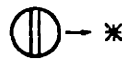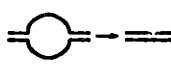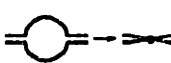
Code	Event	Probability (%)
2	$]\!\complement\!\rightarrow\!)\!($	18.9
3	$]\!]\!\complement\!\rightarrow\!)\!($	3.3
6	$\pi\!\pi\!\Gamma\!\rightarrow\!\widehat{\frown}$	13.7
7	$\pi\!\pi\!\Gamma\!\rightarrow\!\widehat{\frown}$	1.1
8	$]\!D\!\rightarrow\!\supset$	44.4
9	$\smile\!\rightarrow\!\longrightarrow\!\_\_\_$	2.2
10	$\smile\!\bullet\!\rightarrow\!\longrightarrow\!\_\_$	1.6
13	$(\!|\!D\!\rightarrow\!*$	1.6
14	$=\!\bigcirc\!=\!\rightarrow\!=\!=$	9.6
15	$=\!\bigcirc\!=\!\rightarrow\!\bowtie$	2.5
16	$\diamondsuit\!\rightarrow\!\#$	1.1

Table B.2: Branching ratios of T-intersection annihilation ($\Delta n_T = -1$) events. A total of 730 T-intersection events were observed.

Code	Event	Probability (%)
7	$\pi\!\pi\!\Gamma\!\rightarrow\!\widehat{\frown}$	69.2
15	$=\!\bigcirc\!=\!\rightarrow\!\bowtie$	30.8

Table B.3: Branching ratios of monopole creation ($\Delta n_M = +1$) events. A total of 13 events were observed.
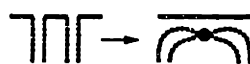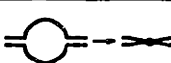
Code	Event	Probability (%)
10		31.6
11		68.4

Table B.4: Branching ratios of monopole annihilation ($\Delta n_M = -1$) events. A total 19 events were observed.
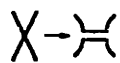
Code	Event	Probability (%)
4		50
17		50

Table B.5: Branching ratios of link creation ($\Delta n_L = +1$) events. A total of two events were observed.

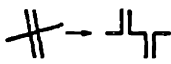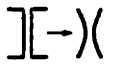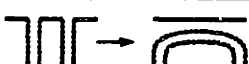| Code	Event	Probability (%)
2		53.5
3		4.7
6		38.8
7		3.1

Table B.6: Branching ratios of link annihilation ($\Delta n_L = -1$) events. A total of 295 events were observed.
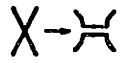
Code	Event	Probability (%)
17	$\mathsf{X \rightarrow \overline{)(}}$	100

Table B.7: Branching ratios of ± 1 string creation ($\Delta n_{1s} = +1$) events. A total of one event was observed.
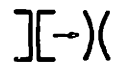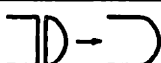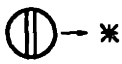
Code	Event	Probability (%)
2	$\mathsf{][\rightarrow)(}$	26.8
3	$\mathsf{]][\rightarrow)(}$	2.3
8	$\mathsf{]D \rightarrow \_)}$	63.0
9	$\longrightarrow$ ───	3.1
10	$\longrightarrow$ ───	2.3
13	$\mathsf{(|D \rightarrow *}$	2.3

Table B.8: Branching ratios of ± 1 string annihilation ($\Delta n_{1s} = -1$) events. A total of 257 events were observed.

B4
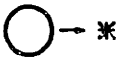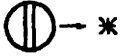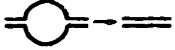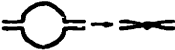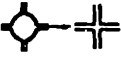
Code	Event	Probability (%)
12	$\bigcirc \to \ast$	50.5
13	$\oplus \to \ast$	5.7
14	$\bigcirc \to =$	17.9
15	$\bigcirc \to \bowtie$	8.6
16	$\diamondsuit \to$	1.9

Table B.9: Branching ratios of $\pm\frac{1}{2}$ string annihilation ($\Delta n_{\frac{1}{2}s} = -1$) events. A total of 105 events were observed.

Appendix C: The Physics of Haggling Defects

Isaac Chuang

January 31, 1991

1 Introduction

This brief summary is meant for those who absolutely insist on understanding the physics underlying my EE'91 thesis. My goal is to address the question "What are the dynamics of defects in a liquid crystal?" aside from all considerations about what a topological defect is, and with as little group theory as possible. As opposed to just presenting results, I will attempt to explain what is happening in the most general and applicable form.

2 The Scenario

First, allow me to review the scenario under consideration. A liquid crystal can be considered to be an assembly of rod-like molecules. Experimentally, a drop of liquid crystal can be studied under a microscope as the temperature is lowered suddenly. When it is hot, the individual molecules orient and position themselves randomly. However, as the system is cooled down, it undergoes a transition into the "nematic" state wherein the individual molecules orient themselves along some preferred direction (in three dimensional space).

Because each individual molecule chooses some random orientation direction, immediately after the phase transition the system is characterized as having many patches of molecules oriented in different directions. These patches will haggle with each other until all the molecules agree, and find one common preferred orientation. During this process, because the system energetically prefers that the orientation of adjacent molecules be as continuous as possible, disagreements in molecule orientation will be localized as much as possible.

These "disagreements" are known as "topological defects," and will be referred to simply as "defects" in our discussion. The interaction of these defects, the haggling by which they come to terms (sometimes through mutual annihilation), can be a beautiful dance which is over in less than a minute. The rules of this dance are the subject of our review.

3 The First Order: A String Network

In the nematic liquid crystal system we are studying, the predominant defect is the $\pm \frac{1}{2}$ string. To a good first approximation, the defect dynamics in a nematic liquid crystal can be approximated as those

1

How to Create Topological Defects

- Gather together an ensemble of many objects

- Give the objects some local interaction

- Create a configuration space with a degeneracy in energy

- Suddenly, and globally, abolish the degeneracy

- Allow the system to relax

Figure 1: Cookbook' recipe for topological defects

Characteristics of the Nematic Liquid Crystal

- Dissipative system (highly viscous medium)

- $\pm\frac{1}{2}$ strings dominated defect dynamics

- Other defects: monopoles and ± 1 strings

- Free energy proportional to $|\vec{\nabla} \cdot \vec{n}|$

Figure 2: Important properties of the nematic liquid crystal

of a $\pm\frac{1}{2}$ string network. "Strings" are one-dimensional defects. They are infinitely long except when they form loops. Strings move under a balance of forces between their own internal "string tension" and the viscous force due to moving through the liquid medium. Their goal is to straighten themselves out. While doing so, they sometimes intersect each other and trade ends. This process have some probability of creating a loop, which will shrink and disappear. See [Vil85] for a comprehensive review article on the subject of strings and their properties.

The dynamics of this "string coarsening" behavior is described extremely well by the so-called "one-scale" model, which originated in the astrophysics community [TH87,Lif82,AT89,BB89,AS90]. We will discuss that model here, and its consequences for our system.

3.1 The one-scale model

The string tension T arises from a string's desire to straighten itself out as much as possible, and thus decrease the derivatives in the orientations of its compositional elements, the rod-like molecules. (As mentioned before, the free energy in the liquid crystal system is proportional to the magnitude of $\vec{\nabla} \cdot \vec{n}$, where $\vec{n}$ is a vector field which gives the orientations of the molecules.) T can be considered to be constant to a good approximation.

The viscous force per unit length, Γ/ξ, which a moving string encounters is proportional to the velocity at which it is moving. The force balance on a moving string is thus written as:

$$f_{\text{viscous}} = f_{\text{string tension}} \tag{1}$$
$$\frac{\Gamma}{\xi} = \frac{T}{\xi}.$$

Next, consider an ensemble of strings, all tangled up together. Knowing the above force balance equation, can we calculate the evolutionary behavior of the string density ρ_S (the line length per unit volume)? Keep in mind that we know that ρ_S must decrease as the strings straighten themselves out.

A relationship between ρ_S and time t can be calculated by examining the rate of loss of energy from the string network. We assume that essentially all the strings at time t can be characterized as having a radius of curvature ξ, and that the string density is approximately $\rho_S \approx \xi^{-2}$. Recalling that energy loss is force $\times$ velocity, we can write the rate of loss of energy as:

$$\frac{dW}{dt} = \frac{Tv}{\xi^3}, \tag{2}$$

per unit volume ξ^3. However, we also know that the string energy density directly:

$$W = T\rho_S. \tag{3}$$

Thus, we can arrive at a differential equation for ρ_S by equating the time-derivative of Eq. (3) with Eq. (2):

$$\frac{d\rho_S}{dt} = -c\frac{T}{\Gamma}\rho_S^2, \tag{4}$$

where a constant of proportionality, c, has been introduced. The general solution for the evolution of the string density with time is given by:

$$\rho_S = \frac{\Gamma}{cT}t^{-\nu}, \tag{5}$$

with $\nu = 1$ as the expected scaling exponent. Note that this solution also implies that the characteristic length scale of a string network ξ is related to time as:

$$\xi \propto \sqrt{t}. \tag{6}$$

I will simply note here that a similar consideration of the balance of forces upon an arc segment of a loop of string results in the same relationship $r \propto \sqrt{t}$. Specifically, Eq.(5.4) shows that

$$r = \sqrt{\frac{2T}{\Gamma}(t_0 - t)}. \tag{7}$$

Experimental data measuring the rate of loop collapse has been used to estimate that T/Γ lies between 200 and 300 μm^2/second in the specific material studied; of course, its precise value depends on the ambient pressure and temperature. A further discussion of the specific values of the elastic constants for the nematic liquid crystal may be found in [KM77] and [WC88].

3.2 In perspective...

One great significance of my work was in showing that the string density actually did evolve as expected in a laboratory bench system. I experimentally found that $\rho_S \approx t^{-1.02\pm0.09}$ for strings produced in a certain nematic liquid crystal. As far as I know, this is the first such confirmation of the one-scale model.

3.3 A one-scale molecular dynamics system

A consequence of the validity of the one-scale model in faithfully describing the coarsening behavior of a string network is that it may be possible to study other systems which are characterizable by a single scale to gain insight into the dynamics of string coarsening. Of course, the motivation would be to find a simpler system (string dynamics are notoriously difficult to simulate). As an example, consider the following, well-known[Toy90] molecular dynamics construction, wherein an ensemble of particles and anti-particles interact together via a Lagrangian

$$\mathcal{L} = KE - \Phi, \tag{8}$$

where Φ is the interaction potential. We approximate the medium in which the particles interact to be so viscous that a particle under no force will immediately come to rest. That is, the equations of motion for the particle position variables $\vec{r}_i$ are given by

$$-\frac{\partial \Phi}{\partial \vec{r}_i} = \gamma \frac{d\vec{r}_i}{dt}, \tag{9}$$

where γ is a damping constant. Setting Φ to be a logarithmic potential (this will give us the correct scaling behavior later):

$$\Phi = \sum_{\langle i,j \rangle} q_i q_j \ln |\vec{r}_i - \vec{r}_j|, \tag{10}$$

we find that the instantaneous velocity of a particle is given by

$$\vec{v}_i = -q_i \sum_j q_j \frac{\vec{r}_j - \vec{r}_i}{|\vec{r}_j - \vec{r}_i|^2}. \tag{11}$$

Given this equation of motion, how does the density of particles behave? In an infinite system with randomly and homogeneously distributed particles and anti-particles, the particle density ρ obeys a simple rate equation:

$$\frac{d\rho}{dt} = -\alpha\rho, \tag{12}$$

where α is the inverse of the characteristic lifetime of a particle. Dimensionally, α can be constructed from the characteristic velocity and length scales such that $\alpha \approx v/\xi$. Using Eq. (11), we find $v \approx 1/\xi$,

and thus $\alpha \approx \xi^{-2}$. Substituting into Eq. (12) along with the definition $\rho \equiv \xi^{-2}$, we have the differential equation

$$\frac{d\xi}{dt} \propto \xi\alpha \approx \frac{1}{\xi}, \tag{13}$$

which has the solution $\xi \approx \sqrt{t}$, as desired.

Thus, we have seen that a the evolution of a two-dimensional ensemble of charged particles does indeed evidence one-scale behavior, at lease in equilibrium. A simple physical picture for understanding why such a model exists can be drawn by considering a two-dimensional cross section of an ensemble of strings. Disregarding strings which lie in the plane, we see that all strings pass through the plane at a point. Some of these points will be "positive" or "negative" (strings have charge also – their topological charge is given by a line integral around a closed contour around the strings axes). As the strings stretch out and intercommute with each other, these points in our plane will move about, and opposites will attract and like will repel. The motion of the points is entirely analogous to the motion of the points in the model we have created. Likewise, the scaling behavior of the characteristic distance between particles in the molecular dynamics system is exactly like the scaling behavior of the string density.

In this section, we have discussed how the physics of the "one-scale" model completely describe the dynamics observed in the string network, the first order approximation to the defect tangle of the nematic liquid crystal. We have also seen how a simpler, two-dimensional molecular dynamics model replicates all of the essential physics, because of the simplicity of the "one-scale" concept. We will consider next interactions of higher order, which lead to non-scaling behavior and require the introduction of new models to explain experimentally observed behavior.

4 The Second Order: Monopoles and ±1 Strings

Second order interactions involve two other defects present in the nematic liquid crystal: monopoles and ±1 strings. Monopoles are zero dimensional (point) defects, and appear as blobs sitting on flux tubes. ±1 strings are flux tubes. They are non-singular strings, and can readily achieve a lower energy state by diffusing out (and just disappearing into nowhere). An imaginative (but not very accurate) analogy might associate a wooden stick with a $\pm\frac{1}{2}$ string and a thin cardboard tube with a ±1 string; a $\pm\frac{1}{2}$ string has a definitive core which cannot go away by itself, while a ±1 string really has no core.

The density of monopoles ρ_M is very small compared to $\rho_S^{1.5}$. The line length per unit volume of visible ±1 string ρ_O also appears to be small compared to ρ_S. Furthermore, neither seem to have any significant effect on the scaling behavior of ρ_S. Experimental data indicate that ±1 strings do interact with $\pm\frac{1}{2}$ strings, but independent measurement of ρ_O is not feasible because of the difficulty in identifying what constitutes a ±1 string. However, ρ_M can be quantified accurately, since monopoles are straightforward (if tedious) to identify and locate.

4.1 Monopole density non-scaling behavior?

The evolution of ρ_M is interesting because experiment has shown that apparently it does not have a scaling behavior until relatively late times. That is to say, while ρ_S seemed to be proportional to t^{-1}

after $t_1 \approx 1.3$ seconds (i.e, $\log \rho_S$ points plotted vs. $\log t$ fell on a straight line of slope -1 after t_1), it was clear that ρ_M rose sharply from a very small value and was still rising at time $t = t_1$, and leveled off at about $t_2 \approx 1.6$ sec. (times quoted from run 8 data, see my thesis for more details).

I will digress from the original aims of this article for two paragraphs for the purposes of elucidating a recent and possibly important insight into explaining the apparent non-scaling behavior of ρ_M.

Two models have been advanced to explain this observation. The first involves a hypothetical limiting mechanism due to the presence of a second length scale in the system, the core radius r_c. Defect energetics arguments, which compare the amount of energy contained inside a ξ^3 volume box enclosing either of three defects ($\pm\frac{1}{2}$ string, ± 1 string, or monopole), indicate the existence of three "epochs" in which the costs of creating one defect over another shift relative to each other. According to this argument, at first the creation of $\pm\frac{1}{2}$ strings are energetically favored, while monopoles are the least favored. Next, the ± 1 strings become favored over $\pm\frac{1}{2}$ strings, and finally, monopole production becomes favored over $\pm\frac{1}{2}$ strings (see Figure 3-4). The key point is that the crossover times are exponential functions of r_c. Unfortunately, however, it is not clear whether or not this comparison is physically meaningful, because it compares isolated defects.

A second model is based on describing the production of monopoles through a simple rate equation, balancing the number of loop collapses (the basic mechanism for monopole creation) with the absorption of monopoles into a $\pm\frac{1}{2}$ string (the basic annihilation mechanism). The initial form of this equation, as proposed by Turok, included a logarithmic function of the core radius as a means for shutting off the monopole creation term, schematically as follows:

$$\frac{d\rho_M}{dt} \approx \alpha\rho_{\text{loop}}\ln(\gamma r_c) - \beta\rho_M . \tag{14}$$

It was felt that the logarithm was needed because of the obvious non-equilibrium behavior of ρ_M as compared to ρ_S at the same times. However, I later realized that the same effect could be achieved by discarding the logarithmic term:

$$\frac{d\rho_M}{dt} \approx \alpha\rho_{\text{loop}} - \beta\rho_M , \tag{15}$$

and replacing it with a specification of an initial condition which would place the system out of equilibrium. For example, requiring that $\rho_M \approx 0$ at $t = 0$ is sufficient, because it necessitates an initial increase in ρ_M in order to reach equilibrium, after which point ρ_M could then decrease as expected, and consistent with experimental observations. The presumption of the existence of such an initial condition is not untenable. Turok has calculated that in the Kibble mechanism essentially zero monopoles are created. This is fundamentally because the probability of randomly coming up with molecule orientations completely wrapping the two-sphere is very small.

Unfortunately, the direct exploration of the non-scaling behavior of ρ_M in a simulation of string dynamics is prohibitive, because of the difficulties associated with simulating an ensemble of strings in three dimensions. However, these difficulties can be circumvented by developing a simple model applicable to the molecular dynamics system described at the end of the last section.

4.2 A simple monopole behavior model

Monopole creation and annihilation dynamics can be explored through a simple extension of the molecular dynamics model previously discussed. In this subsection, we shall develop the rationale behind this

extension, and along the way, highlight some of the main considerations in dealing with simplifying from the actual defect dynamics system.

As presented, only two species of particles exist in the molecular dynamics model, positive and negative charges. By adding a new species to represent monopoles, and by giving it the appropriate creation and annihilation mechanisms, we can hope to compare ρ_M and ρ_S at specific times.

The mutual annihilation of a pair of oppositely charged particles roughly corresponds to the intercommutation of two strings or the collapse of a loop, because of the rapid, local loss of string length during those two processes. Monopoles are created in approximately one quarter of all loop collapse events, and perhaps ten percent of all string intercommutations result in a loop creation. Thus, monopole production should indeed a relatively rare process. One way of implementing a monopole creation mechanism is to create a monopole at the site of a pair annihilation, with some fixed probability, and immediately after the annihilation event. Monopole annihilation can be implemented directly analogously to the observed physics; we see that monopoles disappear by first being attracted towards a $\pm \frac{1}{2}$ string then being absorbed by it. Thus, we may create an attractive potential $\Phi_M \approx \log r$ between monopoles and both positive and negative particles (no difference due to charge).

A typical scenario for this model goes as follows: an initial distribution of totally randomly located charged particles in an infinite system, with no monopoles, is allowed to evolve. At first, the monopole density should increase, until the rate of monopole creation is in equilibrium with the rate of annihilation. This will happen when the cumulative excess number of monopoles created arrives at a total sufficient to sustain an annihilation rate commensurate with the creation rate, which continually decreases from the start because the charged particle density decreases. The crucial questions are whether or not the particle density reaches a scaling solution sooner than does the monopole density, and if the monopole density also attains a scaling solution at late times.

A numerical simulation of the model just described was implemented, and experiments with 400 to 3200 particles and various stepsizes and lattice sizes were run in a box with periodic boundary conditions. Specific results will not be presented here, but preliminary data (see Figure 3) indicate that given the initial condition $\rho_M = 0$, the monopole density ρ_M reaches a scaling solution distinctly after the string density ρ_S does. This observation is consistent with laboratory experiment data, and adds confidence to the model expressed in Eq. (15).

5   Conclusion

Much more remains to be said about this topic. To wit, I could continue by reiterating the discussion about my motivation for and results from my numerical simulations of Chapter 4. I could also rehash my central conclusions and recommendations for future work. However, allow me to simply refer the reader back to the thesis for more details on those subjects, and end by reflecting on what we have reviewed in this article.

We have seen that in the first approximation, the essential physics of a defect ensemble are given by the "one-scale" model, which describes the evolutionary behavior of a string network. This model can also be used to describe the behavior of an ensemble of charged particles interacting through a logarithmic potential, in what we denoted as the molecular dynamics model. Such an approach, much like viewing a crossection of an ensemble of strings, is valuable for its simplicity. In the final section,
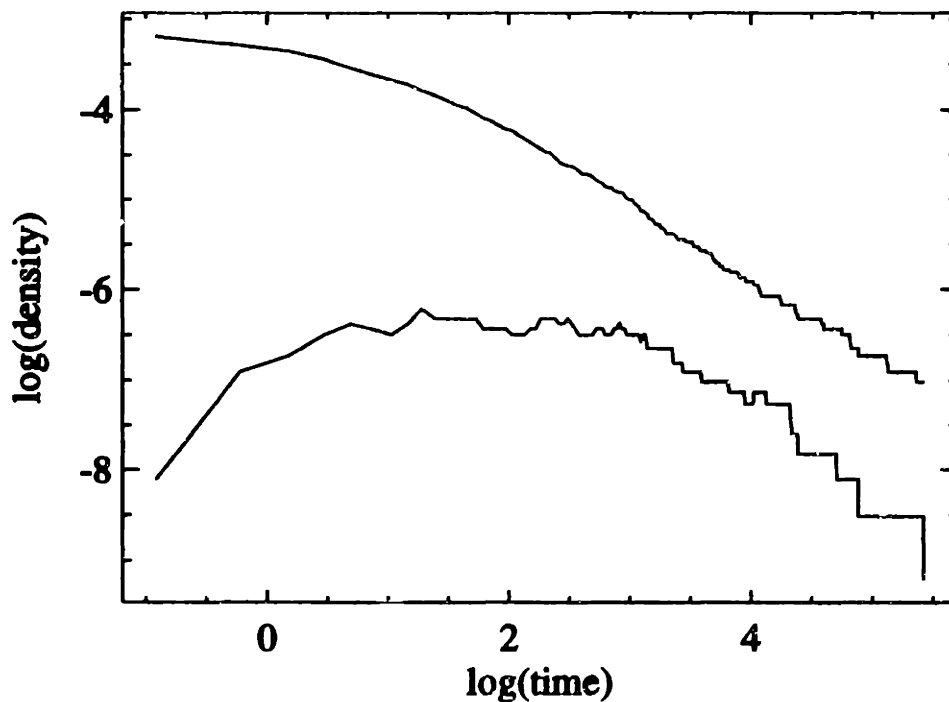
7

Figure ?: Data from molecular dynamics simulation modified to include the effect of monopole creation and annihilation. The upper curve indicates the density of particles in the system as a function of time, and the lower curve shows the monopole density vs. time. The final slope of the particle density line is ≈0.9; theoretically, it should be exactly 1.0. Operational parameters for this run were as follows: dt=0.1, probability of monopole creation for each pair annihilation 10%, size of system 128×128, margin box size 20×20, initial number of particles = 800.

we discussed a specific application of the molecular dynamics model towards the exploration of a second order effect, the non-scaling behavior of the monopole density. Preliminary results from the numerical simulations are promising, but are certainly wanting for future, more rigorous work.